APPLICATIONS OF PIEZOTRONICS AND PIEZO-PHOTOTRONICS

A Dissertation
Presented to
The Academic Faculty

by

Haiyang Zou

In Partial Fulfillment
of the Requirements for the Degree
Doctor of Philosophy in the
School of Materials Science and Engineering

Georgia Institute of Technology
August 2019

APPLICATIONS OF PIEZOTRONICS AND PIEZO-PHOTOTRONICS

Approved by:

Dr. Zhong Lin Wang, Advisor
School of Materials Science and Engineering
Georgia Institute of Technology

Dr. Naresh Thadhani
School of Materials Science and Engineering
Georgia Institute of Technology

Dr. Meilin Liu
School of Materials Science and Engineering
Georgia Institute of Technology

Dr. Zhiqun Lin
School of Materials Science and Engineering
Georgia Institute of Technology

Dr. Mostafa El-Sayed
School of Chemistry and Biochemistry
Georgia Institute of Technology

Date Approved: May 20, 2019

To my dearest family

ACKNOWLEDGEMENTS

I'd like to gratefully acknowledge my advisor-Professor Wang for his guidance and advice. Without his help during the research, I could not have the achievements. From him, I deeply understand that happiness lies not in the mere possession of money, it lies in the joy of achievement, in the thrill of creative efforts. The joy and moral stimulation of work no longer must be forgotten in the mad chase of evanescent profits.

I owe my great gratitude to my family, especially my parents, wife, daughters, and parents in law, they give me love and encouragement, tried their best to support me in all my pursuits. Without their support, I would not be here.

My sincere thanks to my dissertation committee members, Prof. Naresh Thadhani, Prof. Meilin Liu, Prof. Zhiqun Lin, and Prof. Mostafa El-Sayed for the precious time, patience and invaluable advice which they generously offer. It is my pleasure to pay tribute to all the faculty and staff. They shared their valuable knowledge, experience, and advice with me in classes. They have been a great help in my academic performance. I thank all of those who supported me in any respect during the completion of my Ph.D. work. I would like to express my gratitude to my colleagues and friends I met here. I am so happy to have a pleasant and comfortable life here with all my friends. I express my apology to anyone who I did not mention personally. The life in Georgia Tech has been a wonderful journey in my whole life. With the great joy and pride, sheer determination and perseverance, I have courage and conviction in pursuing my goals and ideals.

TABLE OF CONTENTS

ACKNOWLEDGEMENTS **iv**

LIST OF TABLES **vi**

LIST OF FIGURES **vii**

SUMMARY **xiv**

CHAPTER 1. INTRODUCTION **1**
1.1 Motivation **1**
1.2 Piezoelectric **3**
1.3 Piezotronic and Piezo-phototronic **6**

CHAPTER 2. SYNTHESIS OF PIEZOELECTRIC NANOMATERIALS **14**
2.1 ZnO Nanowire Arrays **14**
2.2 A-axis GaN Nanowires **16**
2.3 CdS_xSe_{1-x} Nanowire **19**

CHAPTER 3. PIEZO-PHOTOTRONIC EFFECT ON PHOTOVOLTAICS PROCESSES 21
3.1 Broadband Photodetector Based on p-Si/n-ZnO Nanowire Arrays **21**
3.1.1 Sensitivity and Responsivity from Near-UV to Near-IR 21
3.1.2 Selective Electrons or Holes Transport 34
3.1.3 Response Time 38
3.2 Broadband Photodetector Based on p-Si/AlOx/n-ZnO Nanowire Arrays **46**
3.2.1 Enhanced Photon Sensing Based on p-insulator-n 47
3.2.2 Fowler-Nordheim Tunneling Distance 56
3.3 Photodetector Based on Ternary CdS_xSe_{1-x} Nanowires **64**
3.3.1 Sensitivity and Responsivity 66
3.3.2 The Composition Effect of Materials on Piezo-phototronic Effect 76

CHAPTER 4. PIEZO-PHOTOTRONIC EFFECT ON LIGHT EMISSION PROCESSES 84
4.1.1 Emitted Light Intensity 86
4.1.2 Suppression of Efficiency Droop 90
4.1.3 Physical Mechanisms and Theoretical Simulation 93

CHAPTER 5. Conclusion **102**
5.1 Summary of Work **102**
5.2 Future work **104**

REFERENCES **107**

LIST OF TABLES

Table 1 A comparison of photosensing properties for various nanostructure photodiodes. 29
Table 2 Materials' parameters used in the simulation 94

LIST OF FIGURES

Figure 1 Illustration of the superior material properties of wide bandgap semiconductors over silicon. 3

Figure 2 The piezoelectric effect is a property of certain crystals in which mechanical strain generates an electrical current. Specifically, pressing or deforming the crystal will create a voltage across its two sides. If the material is connected to a circuit, it will generate current. The materials also have a reverse effect: apply electricity to the crystal and it will deform or vibrate. 4

Figure 3 Piezopotential in wurtzite crystal. (a) Atomic model of the wurtzite-structured ZnO. (b) Aligned ZnO nanowire arrays by solution based approach. Numerical calculated distribution of piezoelectric potential along a ZnO NW under axial strain. The growth direction of the NW is c-axis. 7

Figure 4 (a-c) Energy band diagram for illustrating the effects of piezoelectric polarization charges on a Schottky contacted metal-semiconductor interface without and with the presence of non-mobile, ionic charges at the metal-semiconductor interface. The piezoelectric charges are indicated at the interface. (d-f) Energy band diagram for illustrating the effect of piezoelectricity on a p-n junction that is made of two materials of similar bandgaps. The distorted band with the presence of piezoelectric charges is indicated by red lines. 9

Figure 5 Schematic of (a) a general n-type piezoelectric nanowire LED fabricated using p-n heterojunction structure. Schematic of a piezo-phototronic devices: piezo-LED under (b) compressive strain and (c) tensile, where the sign and magnitude of the piezopotential tunes/controls the photon emission, carrier generation and transport characteristics. The color represents the distribution of the piezopotential at the n-type nanowire. 11

Figure 6 Schematic diagram showing the three-way coupling among piezoelectricity, photoexcitation and semiconductor. The core of these coupling relies on the piezopotential created by the piezoelectric materials. 12

Figure 7 (a-b) Top view of ZnO nanowire arrays at low magnification and high magnification. (c) Cross-section view of ZnO nanowire arrays. 16

Figure 8 (a) Schematic illustration of the patterned silicon substrate. (b) SEM images of the nanowires in the plane of the Si substrate; scale bar is 3 μm. (c) SEM images of the nanowire array; scale bar is 2 μm. 18

Figure 9 (a) Cross-sectional SEM images of the patterned Si substrate; scale bar is 4 μm; (b) Cross-sectional SEM images of the as grown nanowire on the patterned silicon; scale bar is 4 μm. 19

Figure 10 Schematic illustration of processing steps for fabricating the p-Si/n-ZnO nanowires array broadband photodiode. 23

Figure 11 Device fabrication and characterization. SEM images of n-ZnO nanowires from (a) top view before PMMA spin coating, (b) XRD diffraction pattern obtained from the ZnO/p-Si heterostructure, (c) side view and (d) 30° tilt view of p-Si/n-ZnO heterojunction after PMMA spin coating and oxygen etched, (e) ITO coating as top electrode. (f) 30° tilt view of ITO coating at the edge of the device after applying strains repeatedly. 25

Figure 12 Optical properties of the device. (a) Absorption spectra of p-Si, n-ZnO, p-Si/n-ZnO nanowire arrays without top electrode, and the sample with mushroom-like ceiling top electrode. (b) Transmission spectra of ITO, ZnO NWs array on the glass before annealed and after annealed. (c) I-V characteristics of the device in dark, under the illumination 442 nm and 1060 nm wavelength with the power densities of 26.45 mW/cm^2, 17.42 mW/cm^2 respectively. (d) The sensitivity of the device under different illumination power densities. 27

Figure 13 Repeatability and time response of the device under (a) 442 nm light with a power density of 0.62 mW/cm^2 and (b) 1060 nm light with a power density of 3.32 mW/cm^2. The chopper on/off ratio is about 20 Hz. The devices were all measured at -2 V bias voltage. 28

Figure 14 Experiment set-up and measurement system. External strains are applied onto the p-Si/n-ZnO PD by pressing the surface of the device through a piece of sapphire. 30

Figure 15 Piezo-phototronic effect on photo response. I-V characteristics of the device under illumination of (a) 442 nm and (d) 1060 nm wavelength with the power densities of 26.5 mW/cm^2, 18.9 mW/cm^2 respectively. The insets are the output current under different strains at -2 V bias voltage at the above illumination condition. Photocurrent of the device under (b) 442 nm, (e) 1060 nm under different strains and illumination conditions, biased at -2 V. 31

Figure 16 The enlarge figure of photocurrent under different compressive strains at (a) 442 nm light with relative high power densities of 26.45 mW/cm^2 (red dots and dash line) and 0.62 mW/cm^2 (blue dots and dash line) and (b) 1060 nm light with a relatively high power density of 18.9 mW/cm^2 (red dots and dash line) and a low power density of 1.32 mW/cm^2 (blue dots and dash line). 32

Figure 17 Piezo-phototronic effect on responsivity. Photo responsivity (a-b) and relative changes (c-d) of photoresponsivity of the device under different strains and illumination conditions, biased at -2 V. (a, c) are under the illumination of 442 nm wavelength, and (b,d) are under the illumination of 1060 nm wavelength. 33

Figure 18 Working mechanism. Photoexcitation and energy-band diagram of the broadband photodiode. 34

Figure 19 Schematic band diagrams of a p-Si/n-ZnO heterojunction under compressive strains applied to illustrate the working mechanism of piezo-phototronic effect under the illumination of (b) 442 nm and (c) 1060 nm wavelength. For the color gradient, red represents positive potential and blue represents negative potential. The black, blue and red dash lines show the energy band at different stages (i), (ii), (iii) under high illumination without strains, high illumination with strains, and low illumination with strains. 36

Figure 20 Response time under different compressive strains. The corresponding rise (a) and fall time (b) of the device under different compressive strains, under different power densities of 442 nm (unit: mW/cm2). The corresponding rise (c) and fall time (d) under different compressive strains under different power densities of 1060 nm light. The error bars indicate the range within a standard deviation. 40

Figure 21 The corresponding (a) rise and (b) fall time of the device under different illumination power density of 442 nm wavelength light, under different strains. 45

Figure 22 The corresponding (a) rise and (b) fall time of the device under different illumination power density of 1060 nm wavelength light, under different strains. 46

Figure 23 Processing scheme for fabricating the 3-D structure broadband photodetector based on p-Si/ AlO_x/ n-ZnO NW arrays. (a) Clean the p-type silicon wafer with acetone, and Isopropyl alcohol. (b) Deposit AlO_x via atomic layer deposition. (c) Deposit a thin layer of ZnO on the sample via RF sputter as the seed layer. ZnO is then grown in the growth solution by hydrothermal growth and annealed then. (d) PMMA resist layer is spin coated and cured. (e) The tips of ZnO nanowires are exposed by oxygen plasma treatment via reactive ion etching. (f) Schematic structure of a 3-D structure p-Si/AlOx/n-ZnO NW arrays photodetector. Deposit ITO by RF sputter as the top electrode. (g) Remove PMMA by acetone. (h) Deposit Al by electron beam evaporation. (i) Schematic structure of a 3-D structure p-Si/AlOx/n-ZnO NW arrays photodetector. 49

Figure 24 Device fabrication and structural characterization. a, Schematic structure of a 3-D structure p-Si/AlOx/n-ZnO NW arrays photodetector. A thin film of insulator AlOx is deposited on p-Si substrate. The nanowire arrays were grown vertically on the insulator layer. The ITO layer was core-shelled with the tips of ZnO nanowires, suspended as the ceiling. b-c, SEM images of top surface view of the device, 30° side view of top surface of ITO coating at the edge of the device, respectively. The ceiling top electrode has enoki mushroom-like texture nanostructure. d, TEM images of the cross-section. The red line in (e) is the scanning route of spectrum profile. f, Spectrum profile of the cross-section. g, X-ray diffraction of ZnO nanowires on Si. h, Energy dispersive X-ray Spectroscopy spectrum of the device. 50

Figure 25 Absorption spectra of p-Si, n-ZnO, and the p-Si/AlOx/n-ZnO devices. 51

Figure 26 Output current under different power densities of (a) 442 nm light and (b) 1060 nm light. 52

Figure 27 Response time for the photodetector. (a) The photo response over a relatively large time scale (0-0.1 s). (b) The inset of current- time figure at a small time scale. 53

Figure 28 Optoelectronic characteristics of the PD. Photocurrent of the device under the illumination of 442 nm (a), 1,060 nm (b) with various the power densities. The sensitivity of the devices under illumination power densities of (c) 442 nm light and (d) 1,060 nm light. (e) The responsivities of the devices under illumination power densities of 442 nm light, and 1,060 nm light. 54

Figure 29 Repeatability and time response of the device under the (a) 442 nm, and (b) 1,060 nm light. 55

Figure 30 Principle of p-Si/AlO_x/n-ZnO broadband photodetector. a, C-V characteristics of the p-Si / AlO_x. The p-Si side for the device based on p-si/AlO_x, is connected with the positive electrode. VBF corresponds to the flat-band condition. Ci refers to the capacitance of the capacitor for this accumulation mode. C_p refers the capacitance of the capacitor at the present status. b, C-V characteristics of the AlO_x / n-ZnO NW arrays. The n-ZnO side for the device based on AlO_x / n-ZnO is connected with the negative electrode. c, Energy-band diagram in p-insulator-n for the dual inversion layers mode under an appropriate large negative bias. The carrier charges flow through the insulating layer by quantum mechanical Fowler-Nordheim tunneling. Two inversion layers are formed at two sides of the insulating layer. The conduction and valence band edges bend as shown in the figure, indicating a space charge region similar to that in a pn junction. The conduction band and intrinsic Fermi levels move closer to the Fermi level. The intrinsic Fermi level Ei at the surface is now below the Fermi level EF; thus, the surface of the semiconductor adjacent to the oxide-semiconductor interface has inverted from a p-type to an n-type semiconductor. Similarly, we have created an inversion layer at the interface of oxide/n-ZnO nanowire arrays. 59

Figure 31 Schematic energy band diagram of Folwer-Nordehim tunneling in insulator-semiconductor structure for p-Si / AlOx (a), and AlOx / n-ZnO NW arrays (b). (a) When a sufficiently large negative gate voltage was applied, the bands near the interface bent downward so that the intrinsic Fermi level Ei would lie below the Fermi level EF. The conduction band would get closer to EF than the valence band to EF. At this point, the semiconductor surface adjacent to the oxide-semiconductor interface was n-type, and an inversion layer of electrons was induced at the oxide-semiconductor interface. (b) By an applied negative voltage, the positive space charge region is induced; within this region, the conduction and valence band energies bend upward, and the intrinsic Fermi level has moved above the EF so that the valence band is closer to the Fermi level than the conduction band to EF. This result implies that the semiconductor surface adjacent to the oxide-semiconductor interface inverts from n-type to p-type. An inversion layer of holes has been induced at the oxide-semiconductor interface. 61

Figure 32 Experiment set-up and measurement system for applying strains on devices. The blue block refers to sapphire. The green strands for the sample. Two Kapton tapes were used to fix the sample and sapphire. 62

Figure 33 Study of the effect of AlO_x on electron and hole transport by using piezo-phototronic effect. Current output under different strains at -2 V bias voltage under 442 nm (a) and 1,060 nm (b) light with different power densities. Band diagram of the broadband photodiode under compressive strains at 442 nm light (c) and 1,060 nm light (d). For the color gradient, pink represent positive piezo-charges region and blue represents negative piezo-charges. The blue lines are the energy bands at the initial stage without strain, the short dot lines are the energy bands when the external strains applied. 63

Figure 34 (a) SEM image of CdS_xSe_{1-x} NWs, the inset is a high magnification SEM image of a typical CdS_xSe_{1-x} NW with a catalyst Sn-particle on the tip. (b1) TEM image and (b2) HRTEM image of a typical CdS_xSe_{1-x} NW, (b3) is the corresponding SAED pattern, indicating that the CdS_xSe_{1-x} NW is single crystal and grown along c-axis.(c) Normalized XRD patterns of three representative CdS_xSe_{1-x} NWs obtained at different growth temperatures. (x=0. 85, 0.60 and 0.38).(d) The normalized PL spectra of the obtained CdS_xSe_{1-x} nanobelts excited with an Ar-ion laser (488 nm).(e) Schematic of the measurement setup for studying the piezo-phototronic effect in CdS_xSe_{1-x} NW. The inset is a digital image of the as-fabricated device on flexible PET. (f) Schematic diagram and (g) a typical optical image of the PD device. 68

Figure 35 (a-c) The typical I-V characteristics of the single CdSxSe1-x NW PD as a function of excitation light intensity. Curves (a)-(c) for x=0. 85, 0.60 and 0.38, respectively. The inset in (a-c) is the photocurrent of the NW PD without strain under different illumination intensity with the periodical changing of light irradiation on and off. (d) The typical response time of a single CdSxSe1-x NW PD. (e) Absolute photocurrent and (f) derived photo-responsivity relative to excitation intensity on the three NW devices at bias = 2.0 V. Excitation wavelength = 442 nm. 70

Figure 36 (a-c) Photo-sensitivity relative to excitation intensity of the single NW PD device #(1-3). Excitation wavelength = 442 nm, bias=2.0 V. 72

Figure 37 Repeatable response of (a) $CdS_{0.\ 85}Se_{0.15}$ NW and (b) CdS NW. Excitation wavelength = 532 nm, Bias=2.0 V. 73

Figure 38 (a-c) The typical I-V characteristics of device #1 (CdS0.85Se0.15) under different tensile and compressive strains, with excitation light intensity of (a) 0.2 mW/cm2, (b) 3.5 mW/cm2 and (c) 44 mW/cm2, the inset in (a-c) is the corresponding absolute photocurrent at bias=2.0 V. (d) Changes of photocurrent derived from (a-c), I0 is set as photocurrent under zero strain for this illumination power. (e) The derived change in SBH as a function of strain using the thermionic emission diffusion model. (f) Changes of responsivity derived from (a-c); R0 is set as responsivity under zero strain. Excitation wavelength = 442 nm. 74

Figure 39 (a-c) Column graph of absolute photocurrent under different tensile strains and different excitation intensity at bias = 2.0 V. Graph (a)-(c) for device #1 ($CdS_{0.85}Se_{0.15}$), device #2 ($CdS_{0.60}Se_{0.40}$) and device #3 ($CdS_{0.38}Se_{0.62}$), respectively. (d, e) Dependences of responsivity (R) and relative increases of responsivity ($\Delta R/R_0$) on excitation light intensity

under 0.4% tensile strain and at bias of 2.0 V, derived from (a-c); R_0 is set as responsivity under zero strain. Excitation wavelength = 442 nm. (f) Simulation of the piezopotential distribution in the wire of typical CdS_xSe_{1-x} with x=0.85, 0.6 and 0.32 under tensile strain. 77

Figure 40 Simulation of the piezopotential distribution in the wire under tensile strain (a) for CdS, (b) for CdSe. The diameter and length used for calculation is about 500 nm and 200 μ m, respectively. 79

Figure 41 Schematic Energy band diagram for illustrating the piezo-phototronic effect on a Schottky contacted metal-semiconductor interface when (a) only illumination, (b) tensile strain and illumination, (c) compressive strain and illumination are applied to the single CdS_xSe_{1-x} NW device. 81

Figure 42 General characteristics of GaN MW-based LEDs. (a) Atomic structure model (overall and cross-section view) of the GaN MW (a1) and schematic image of the fabricated LED (a2). (b) Schematic image showing the light emission escaped from the distal end of the GaN MW. Upper inset: light spot of the MW-based LED observed under microscope. Lower inset: SEM image of the trapezoid-shaped end surface of GaN MW. (c) *I–V* characteristic of the as-fabricated LED. Inset: photograph of a real MW-based LED device. (d) Room-EL spectrum collected from the MW-based LED device and corresponding peak-deconvolution with Gaussian functions of the EL spectrum. 87

Figure 43 Electrical and optical properties of the fabricated LEDs. (a) Conformation of good Ohmic contact when n-GaN MW and p-GaN film contact with two ITO electrodes. (b) EL spectra at various injection currents collected from the fabricated micro-LED. (c) Micro-PL spectrum of a single n-GaN MW; Inset: corresponding peak peak-deconvolution with Gaussian functions of the micro-PL spectrum. (d) The calculated effective barrier height of the PN junction in the GaN MW-based LEDs under various compressive strains. 88

Figure 44 Enhancement of emitted light intensity by piezo-phototronic effect. (a) Schematic diagram of the homemade measurement system for characterizing the performances of MW-based LEDs under compressive strain. (b) I−V characteristic of the as-fabricated LED at forward bias with the variation of the applied compressive strain. (c) Optical spectra collected from the MW-based LED at 20 μA injection current under various compressive strains (lower panel) and corresponding CCD images recorded from the emitting end of the GaN MW under different applied strain. (d) Change of the integrated EL intensity (magenta) and relative EQE (blue) of the MW-based LED with increasing externally compressive strain. 89

Figure 45 Suppression of efficiency droop by piezo-phototronic effect. (a) EL spectrum under various injection current density from 3.3 to 83.3 A cm^{-2} under continuous (left) and pulsed (right) current injection mode. (b) Evolution of the peak wavelength as increasing injection current density under continuous (magenta) and pulsed (blue) mode. (c) Corresponding relative EQE (η_{ex}) of the MW LED devices represented by Ψ/J at each

injection current density (*J*) point under various compressive strains. (d) Droop onset current densities and the change of efficiency drop values as a function of the external applied strains. (e) Relative change of η_{ex} at each injection current density condition. 91

Figure 46 Theoretical simulation results and physical mechanisms. (a) Under a −0.12% compressive strain, the overall view of piezo-potential distribution. (b) Piezo-potential values across the LED device normal to the p–n junction interface; inset: cross-section view of piezo-potential distribution within the GaN MW-based LEDs under −0.12% compressive strain. (c) Generation of piezo-potential and corresponding energy band profile of the LED devices under strain-free (left) and compressive strain (right) conditions. 96

Figure 47 (a) Reduction of GaN bandgap (*ΔEg*) and built-in electric potential difference (*ΔVd1*) caused by the strain-induced deformation as a function of externally applied compressive strain. (b) Theoretically simulated energy band diagram of GaN p-n junction. (c) The calculated total reduction of built-in electric field (*ΔVd*) caused by external strain as a function of externally applied compressive strain. 98

Figure 48 Experimental and theoretical simulation results of the GaN MW-based LEDs with inverted *c*-axis orientation for *n*-GaN MW. (a) Overall view SEM image of the as-fabricated LEDs; Inset: The corresponding end surface of *n*-GaN MW. (b) EL characteristics of this kind LEDs are collected under various compressive strains. (c) Under -0.12% compressive strain, the overall view of piezo-potential distribution within the GaN MW-based LEDs. (d) Piezo-potential values across the LED device normal to the *p*-*n* junction interface; inset: cross-section view of piezo-potential distribution within the GaN MW-based LEDs under -0.12% compressive strain. 100

SUMMARY

Third-generation semiconductor materials have superior performance with high voltage resistance, high frequency, high efficiency, high-temperature resistance and high radiation resistance, that they look to be the “core” of a new generation of information technology, energy saving, and smart manufacturing. They can have broad application prospects in many fields, and have attracted the attention of governments, industries and research communities all over the world and achieved rapid development. The typical materials such as GaN and ZnO simultaneously exhibit piezoelectric, semiconducting and photoexcitation properties. The piezoelectric polarization charges can be utilized to control/tune the charge carrier transport characteristics in these materials (piezotronic effect), and also used to tune the generation, transport, separation and/or recombination of charge carriers (piezo-phototronic effect). The coupling of these properties in these materials has resulted in both novel fundamental phenomenon and unprecedented device application, leading to the increasing research interests in the emerging field of piezotronics and piezo-phototronics. Functional electronic and optoelectronic devices are presented to illustrate the practical applications of the piezotronic and piezo-phototronic effects. Fundamental physics about the piezotronics and piezo-phototronics are further studied in this work. This will help to develop a full understanding of piezotronics and piezo-phototronics, and it also enables the development of the better performance of optoelectronics. By applying the two effects in a wide range of electronics/optoelectronics, we have shown they are effective approaches to modify the physical properties in

piezoelectric semiconductors and a useful tool to study the physical model in a complex system.

CHAPTER 1. INTRODUCTION

1.1 Motivation

Semiconductor refers to a material of conductivity between the conductor – such as copper, gold etc. – and an insulator, such as glass. During the growing digital information stage, the semiconductor industry supports the development and progress of information technology in society as a whole and further changes the way of life, production, communication and thinking. The first-generation semiconductor materials specifically refer to silicon materials, which are the backbone of electronics from radios to computers now. And the second-generation semiconductor materials typically refer to GaAs and InP materials, which are widely used in the manufacture of devices such as microwave frequency integrated circuits, communication system, solar cells and detectors. Advances in power semiconductor technology have improved the efficiency, size, weight and cost of power electronic systems. New components based on wide band gap materials are on the way to be the next generation of advanced applications. Wide bandgap semiconductors (WBG) such as SiC, GaN, ZnO and AlN show superior material properties compared to Silicon, as shown in the Figure 1. Due to these unique characteristics, these WBG become the unique material of choice to help solving the energy problems of the future. Recently, the third-generation semiconductor materials represented by WBG semiconductors achieves rapid development, they have attracted the attention of governments, industries and research communities all over the world. They have high voltage resistance, high frequency, high efficiency, high temperature resistance and high radiation resistance. They look to be the “core” of a new generation of information technology, energy saving and

smart manufacturing and used to produce high voltage, high power devices and have broad application prospects in many fields such as consumer electronics, industrial drives, agricultural machinery, power transmission, rail transit and military applications. The prominent spontaneous and piezoelectric polarization effects and flexibility in inserting appropriate heterojunctions thus dramatically broadening the device design space.

The typical materials such as GaN and ZnO simultaneously exhibit piezoelectric, semiconducting and photoexcitation properties. Piezoelectricity is an effect that the electric charge that accumulates in certain solid materials in response to applied mechanical stress. Piezoelectric effect has been widely used in electromechanical sensing, actuation and energy harvesting, which produces polarization charges under mechanical deformation in materials lacking inversion symmetry or with polarization domains.

The coupling of piezoelectric polarization with semiconductor properties in these materials has resulted in both novel fundamental phenomenon and unprecedented device applications, leading to the increasing research interests in the emerging field of piezotronics and piezo-phototronics. The basic of piezotronics and piezo-phototronics lies in the fact that strain-induced polarization charges at interface can effectively modulate the local band structure and hence the charge carrier transport across local junctions/contacts by exerting substantial influence on the concentration/distribution of free carriers and interfacial electronic charged states in the device.

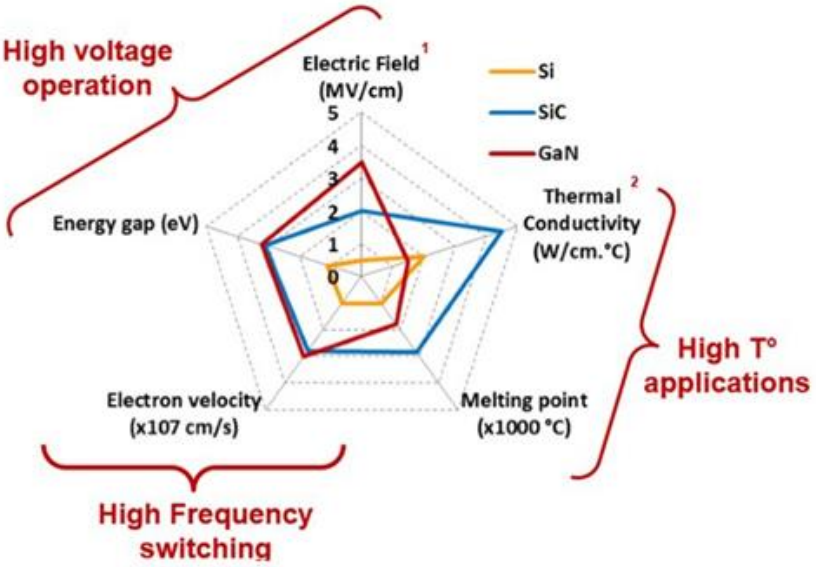

Figure 1 Illustration of the superior material properties of wide bandgap semiconductors over silicon.[1]

In this work, functional electronic/optoelectronic devices based on piezoelectric semiconductor materials are presented to demonstrate the practical applications of the piezotronic and piezo-phototronic effects, including nanowire/microwire transistors, bio/chemical sensors, photo detectors and light-emitted diode (LED). Fundamental physics about the piezotronics and piezo-phototronics are systematically studied. By successfully applying the piezotronic and piezo-phototronic effects in a wide range of electronics/optoelectronics, we have shown the universality of these two effects to be utilized in various practical applications as effective approaches to modify the physical properties of charge carriers in piezoelectric semiconductors.

1.2 Piezoelectric

The phenomemon of piezoelectricity was discovered as early as 1880 by Jaques and Pierri Curie. Materials that belong to the class of noncentrosysmmetric crystals are

classified as piezoelectric materials. When these materials are subjected to an external strain by applying pressure or stress, the electric dipoles in the crystal get oriented such that crystal develops positive and negative charges on opposite faces, resulting in an electric field across the crystal. The effect is called the direct piezoelectric effect (Figure 2).

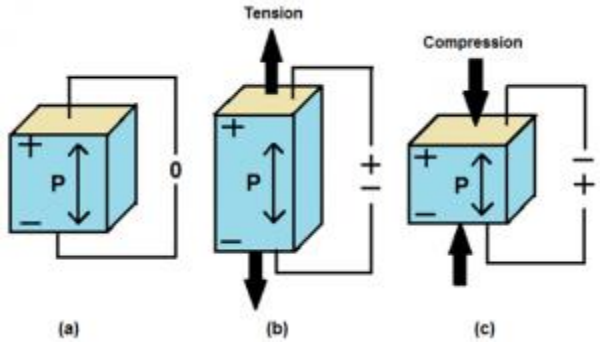

Figure 2 The piezoelectric effect is a property of certain crystals in which mechanical strain generates an electrical current. Specifically, pressing or deforming the crystal will create a voltage across its two sides. If the material is connected to a circuit, it will generate current. The materials also have a reverse effect: apply electricity to the crystal and it will deform or vibrate.

When these materials are subjected to an external electric field, there will be asymmetric displacements of anions and cations that cause considerable net deformation of the crystal. The resulting strain is directly proportional to the applied electric field unlike electrostrictive materials in which the strain is proportional to E^2. The polarity of the applied filed determines the strain in a piezoelectric material, whether it is extensive or compressive. This effect is called indirect piezoelectric effect.

The piezoelectric materials have gained importance over the last few decades due to the rapid development of Internet of Thing (IoT), artificial intelligence and smart materials. These materials can convert mechanical energy into electrical energy, which are

useful as sensitive sensors of mechanical inputs such as pressure, strain, vibration, rotation, sound, ultrasound, etc. They belong to the class of smart materials and are now become the essential parts of smart systems in machines. Piezoelectric devices are being used in field such as aerospace, automotive, industrial equipment, defense equipment, robotics, household appliances, etc. The applications also include generation and detection of ultrasonic waves, pressure sensors, and actuators. Ultrasonic is extensively used in both in engineering and medical fields. In engineering, it is used in non-destructive tesing of materials (NDT), underwater acoustics (SONAR), ultrasonic drilling, energy harvesting, etc., and in medical fields, it is used for diagnosis (sonography), therapy (drug delivery), and surgery.

There are many piezoelectric materials, both natural and synthetic, which exhibit piezoelectric properties due to their noncentrosymmetric crystal structure. Barium titanate and zinc oxide thin films are typical significant piezoelectric materials. The crystal structure of ZnO is hexagonal wurtzite with symmetry of 6mm, thus, a single crystal of ZnO has a unique direction (c-axis), which is the polar direction. ZnO thin films with high C-axis orientation exhibit good piezoelectric properties. Nanostructural ZnO crystals, such as nanowires and nanotubes have been studied extensively for various piezoelectric applications. The typical techniques are RF sputtering, sol-gel spin coating, chemical vapour deposition, hydrothermal synthesis and pulsed laser deposition.[2-4] ZnO nanocrystals grown in form of thin fibers have been investigated for applications as nanogenerators.[5, 6] Nanobelts, nanorings, and nanosprings could be used for nanoactuators and sensors.[7] The piezoelectric ZnO thin films as ultrasonic tranducer arrays is also reported.[8]

1.3 Piezotronic and Piezo-phototronic

The wurtzite materials, such as ZnO, GaN, InN, and ZnS, has a non-central symmetric crystal structure, which naturally produces piezoelectric effect once the materials is strained. Wurtzite crystal has a hexagonal structure with a large anisotropic property in c-axis direction and perpendicular to the c-axis. Simply, the Zn^{2+} cations and O^{2-} anions are tetrahedrally coordinated and the centers of the positive ions and negative ions overlap with each other. If a stress is applied at an apex of the tetrahedron, the center of the cations and the center of anions are relatively displaced, resulting in a dipole moment. A constructive add-up occurs of the dipole moments created by all of the units in the crystal results in a macroscopic potential drop along the straining direction in the crystal. This is the piezoelectric potential, as shown in Figure 3. Piezopotential can serve as the driving force for the flow of electrons in the external load once subject to mechanical deformation, which is the fundamental of the nanogenerator.

The induced flow of electrons in the external circuit by the piezoelectric potential is the energy generation process. The presence of the piezopotential can drastically change the transport characteristic of a NW-based FET. To systematically represent the piezoelectric-semiconductor coupled properties of such a system, Wang introduced the concept of nano-piezotronics.[9, 10]

To better understand the piezotronic effect, the two fundamental structures of Schottky contact and p-n junction is presented (Figure 4). When a metal and a n-type semiconductor forms a contact, a Schottky barrier is created at the interface if the work

function of the metal is appreciably larger than the electron affinity of the semiconductor (Figure 4a).

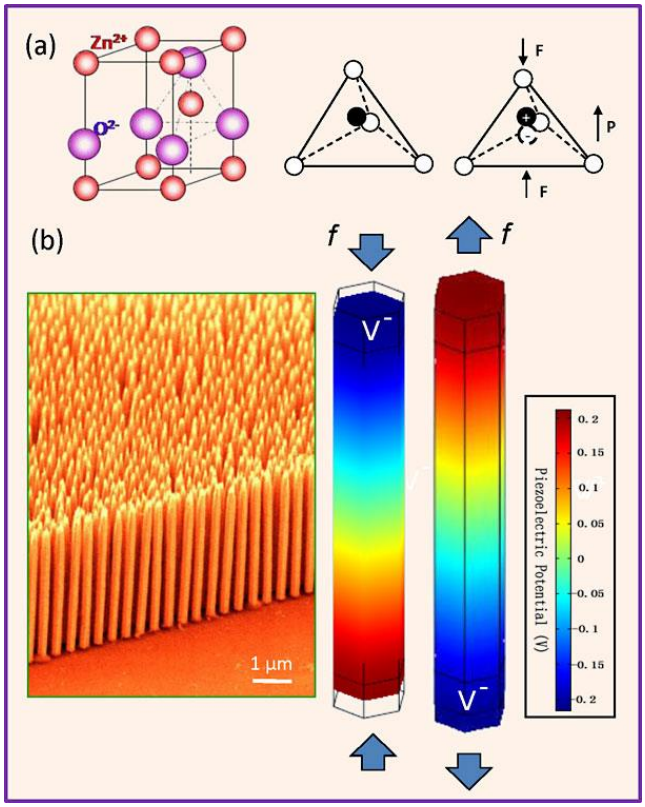

Figure 3 Piezopotential in wurtzite crystal. (a) Atomic model of the wurtzite-structured ZnO. (b) Aligned ZnO nanowire arrays by solution based approach. Numerical calculated distribution of piezoelectric potential along a ZnO NW under axial strain. The growth direction of the NW is c-axis. [11, 12]

Strain in the structure would produce piezo-charges at the interfacial region. It is important to note that the polarization charges are distributed within a small depth from the surface at the interface and they are ionic charges, which are non-mobile charges located adjacent to the interface. The positive piezo-charges effectively may lower the barrier height at the local Schottky contact, while the negative piezo-charges increase the barrier height (Figure 4b and c). The role of the piezopotential is to effectively change the local contact characteristics through an internal field depending on the crystallographic

orientation of the materials and the sign of the strain, thus, the charge carrier transport process is tuned/gated at the M-S contact. Therefore, the charge transport across the interface can be largely dictated by the created piezopotential, which is the gating effect. By switching the strain from tensile to compressive, the piezopotential polarity is changed, the local contact characteristics can be tuned and controlled by the magnitude of the strain and the sign of strain. These are the cores of the piezotronic effect.

When a p-type and a n-type semiconductors form a junction, the holes in the p-type side and the electrons in the n-type side tend to redistribute to balance the local potential, the interdiffusion and recombination of the electrons and holes in the junction region forms a charge depletion zone. The piezo-charges will be mostly preserved without being screened by local residual free carriers. The presence of such a carrier-free zone can significantly enhance the piezoelectric effect. For simplicity, the p-n homojunction is considered here. As shown in Figure 4d, if the n-type side is piezoelectric and a strain is applied which induced positive piezo-charges at the junction, the piezopotential tends to lower the local band slightly and introduce a slow slope to the band structure, as shown in Figure 4e. Alternatively, if the applied strain is switched in sign, the negative piezo-charges at the interface tends to raise the local band. Therefore, with the creation of a piezopotential in one side of the semiconductor materials under strain, the local band structure near the p-n junction is changed/modified, as shown in Figure 5. The fundamental working principles of the p-n junction and the Schottky contact are that there is an effective barrier that separates the charge carriers at the two sides to across. The height and width of the barrier are the characteristic of the device. In piezotronics, the role played by the piezopotential is to effectively change the width of p-n junction or height of SB by piezoelectricity.

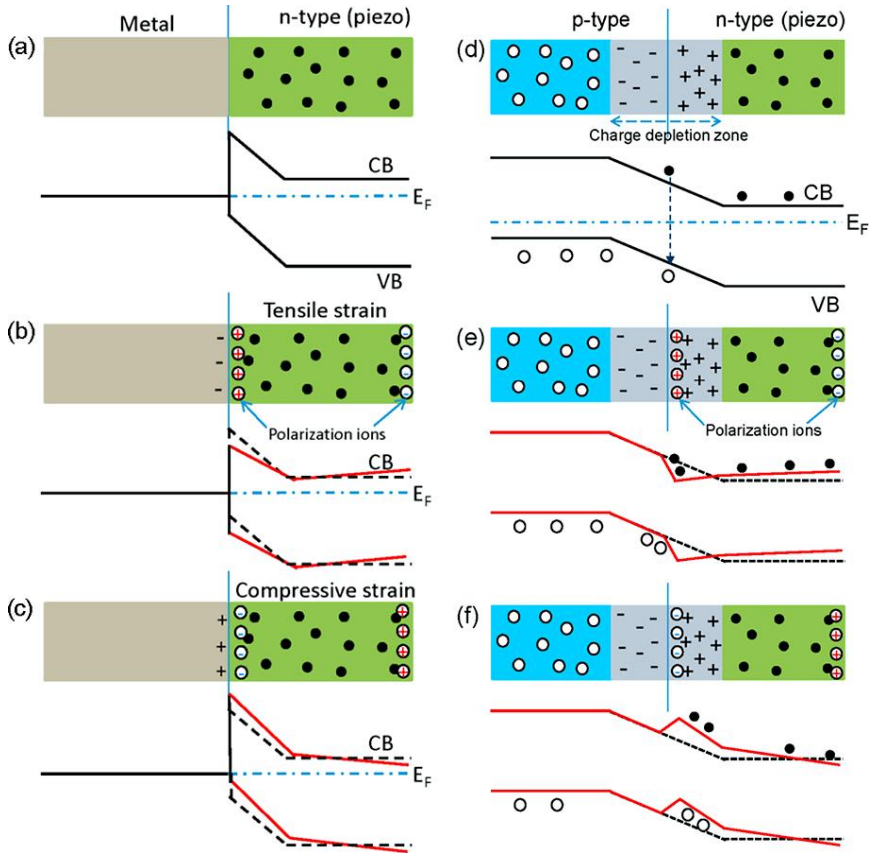

Figure 4 (a-c) Energy band diagram for illustrating the effects of piezoelectric polarization charges on a Schottky contacted metal-semiconductor interface without and with the presence of non-mobile, ionic charges at the metal-semiconductor interface. The piezoelectric charges are indicated at the interface. (d-f) Energy band diagram for illustrating the effect of piezoelectricity on a p-n junction that is made of two materials of similar bandgaps. The distorted band with the presence of piezoelectric charges is indicated by red lines. [11, 12]

Semiconductor physics and piezoelectric theories are used for describing the process involved in a piezo-phototronic device that is fabricated by piezoelectric semiconductor. The static and dynamic transport behavior of the charge carriers and the interaction of a photon and an electron in semiconductors are described by semiconductor physics. The behavior of the piezoelectric material under dynamic straning is described by piezoelectric theories. Therefore, electrostatic equations, current-density equations, continuity equations, and piezoelectric equations are applied as basic governing equations for characterizing piezo-phototronics devices.

The electrostatic behavior of charges in piezoelectric semiconductor is described by the Poisson equation:

$$\nabla^2 \Psi_i = -\frac{\rho(r)}{\varepsilon_s} \tag{1}$$

where Ψ_i, $\rho(r)$ and ε_s are the electric potential distribution, the charge density distribution, and the permittivity of the material.

The drift and diffusion current-density equations that correlate the local fields, charge densities, and local current are

$$\begin{cases} \boldsymbol{J}_n = q\mu_n n\boldsymbol{E} + qD_n \nabla n \\ \boldsymbol{J}_n = q\mu_p p\boldsymbol{E} - qD_p \nabla p \\ \boldsymbol{J} = \boldsymbol{J}_n + \boldsymbol{J}_p \end{cases} \tag{2}$$

where J_n and J_p are the electron and hole current densities, q is the absolute value of unit electronic charge, μ_n and μ_p are electron and hole mobilities, *n* and *p* are electron and hole mobilities, n and p are concentrations of free electrons and free holes, D_n and D_p are diffusion coefficients for electrons and holes, respectively, $\boldsymbol{E}$ is electric field, and $\boldsymbol{J}$ is the total current density.

The charge transport under the driving of a field is described by the continuity equations

$$\begin{cases} \dfrac{\partial n}{\partial t} = G_n - U_n + \dfrac{1}{q}\nabla \cdot J_n \\ \dfrac{\partial p}{\partial t} = G_p - U_p - \dfrac{1}{q}\nabla \cdot J_p \end{cases} \tag{3}$$

where G_n and G_p are the electron and hone generation rates, U_n and U_p are the recombination rates, repectively.

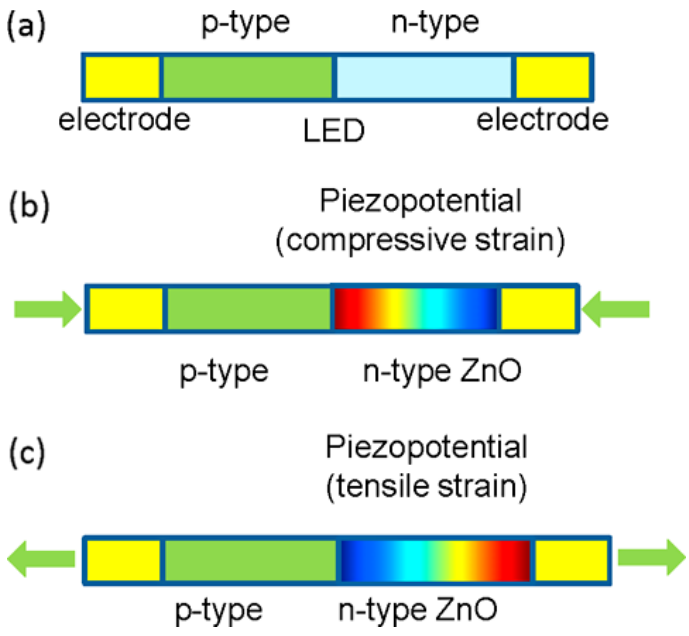

Figure 5 Schematic of (a) a general n-type piezoelectric nanowire LED fabricated using p-n heterojunction structure. Schematic of a piezo-phototronic devices: piezo-LED under (b) compressive strain and (c) tensile, where the sign and magnitude of the piezopotential tunes/controls the photon emission, carrier generation and transport characteristics. The color represents the distribution of the piezopotential at the n-type nanowire.

The relationship between polarization **P** vector and a small uniform mechanical strain S is given by

$$(\mathrm{P})_i = (e)_{ijk} S_{jk} \tag{4}$$

where the third order tensor S_{jk} is the piezoelectric tensor. The constituent equations can be written as

$$\begin{cases} \sigma = c_E S - e^T E \\ D = eS + kE \end{cases} \tag{5}$$

where σ and c_E are the stress tensor and the elasticity tensor, respectively. E, D, and k are the electric field, the electric displacement, and the dielectric tensor, respectively.

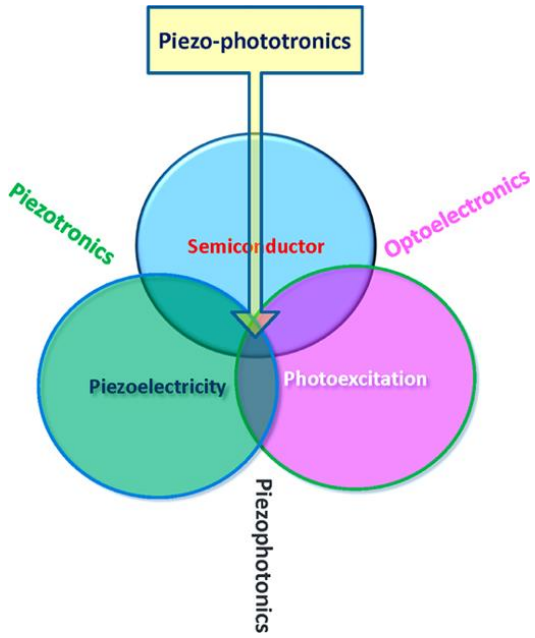

Figure 6 Schematic diagram showing the three-way coupling among piezoelectricity, photoexcitation and semiconductor. The core of these coupling relies on the piezopotential created by the piezoelectric materials. [11, 12]

The optoelectronics is a well-known effect of semiconductor with photon excitation process. For a material that simultaneously has semiconductor, photon excitation and piezoelectric properties, there are two other fields that a coupling a semiconductor with piezoelectric to form a field of piezotronics, and piezoelectric with photon excitation to form a field of piezophotonics. A coupling among semiconductor, photon excitation and piezoelectric is a field of piezo-phototronics (Figure 6). This is the basis for fabricating piezo-photonic-electronic nanodevices. The piezo-phototronic effect is to use the piezopotential to tune/control the charge generation, separation, transport and/or recombination at an interface/junction for achieving superior optoelectronic processes.

An effective electron-hole separation at a Schottky contact or p-n junction is important for the efficiency of a photon detector. The piezo-phototronic effect can be used to largely improve the responsivity of a photon detector in a whole range from visible to ultraviolet and even near-infrared light. As a classical device, the performance of an LED is dictated by the structure of the p-n junction and the characteristics of the semiconductor materials. The piezo-phototronic effect can be very effectively used for enhancing the efficiency of energy conversion in today's green and renewable energy technology.

CHAPTER 2. SYNTHESIS OF PIEZOELECTRIC NANOMATERIALS

2.1 ZnO Nanowire Arrays

A variety of techniques have been proposed to synthesize ZnO nanowires, each with their own strengths and weaknesses. Vapor based techniques such as vapor-liquid-solid or vapor-solid-solid, produce long length of single crystalline nanowires with a low defect density.[13] These methods require very high temperatures, on the order of 900-1300 ℃, which limits the choice of substrates for growth. Molecular beam epitaxy (MBE) could produce high purity single crystalline ZnO nanorods,[14] but it is a costly and slow process and requires high vacuum.

Solution based hydrothermal growth has become one of the most popular means of producing ZnO nanowires. It has many advantages over the aforementioned methods. First, it is low cost. The precursors and growth solution are inexpensive, and no special equipment is needed except a low-temperature oven and glass jars. Second, it is available for most substrates, including polymers, due to the low growth temperature (65-95 ℃), enabling applications in flexible electronics. The growth is uniform and easy to control, allowing for uniform wafer scale growth.[15] Finally, the nanowire dimensions can be easily tuned by adjusting growth parameters such as temperature, time, or precursor concentrations.[16]

Hydrothermal synthesis of ZnO nanowire arrays is performed by mixing a zinc salt, such as zinc nitrate or zinc chloride, with equal molar parts of hexamethylenetetramine

(HMTA) in water. A substrate with a seed layer is placed in the solution, and then is heated in an oven for some time. To avoid agglomeration of homogeneously nucleated material on the substrate, it is typically floated on the solution surface, seed layer down. HMTA acts as a weak base, which slowly hydrolyzes water to provide oxygen as shown in the following reactions: [17]

$$(CH_2)6N_4 + 6H_2O \leftrightarrow 4NH_3 + 6HCHO \quad (6)$$

$$NH_3 + H_2O \leftrightarrow NH_3 \cdot H_2O \quad (6)$$

$$NH_3 \cdot H_2O \leftrightarrow NH^{4+} + OH^- \quad (7)$$

The resulting OH^- anions react with the Zn^{2+} cations from the salt to form ZnO as follows:

$$Zn^{2+} + 2OH^- \leftrightarrow Zn(OH)_2 \quad (8)$$

$$Zn(OH)_2 \leftrightarrow ZnO + H_2O \quad (9)$$

As a result, the growth rate is highly dependent on the pH of the solution, and has been shown to reach a maximum at a pH of 10.6.[18] At higher levels, it has been suggested that subreactions such as the dissolution of ZnO occur, slowing down growth. ZnO naturally forms aligned wires as it grows preferentially along the [0001] direction.[19] Form a wire would minimizes the surface area of the high energy (0001) surface.

The growth of nanowires could be controlled by adjusting parameters. Temperature was found to be an important determinants of the nanowire morphology. This was attributed to basic kinetics of nucleation and growth. At low temperatures, the Zn ions can not diffuse easily, which results in large nuclei. On the other hand, if the temperature is too

high, the growth materials will have a higher affinity to the nuclei formed, resulting in more growth, but less nucleation. Similarly, changes in precursor concentration is observed to affect the growth. Increasing the concentration of zinc nitrate and HMTA improves deposition density until it reaches a saturation pint. With a higher precursor concentration, more nucleation sites are needed to balance out the increased chemical potential. Once the concentration goes beyond the saturation point, it is more probable that the Zn ions will attach to the existing nanorods rather than form new nuclei. At the initial stages, lateral growth dominates. Next, the nanowires will grow axially while the width remained constant. Eventually, the wires will continue to grow in both direction, becoming longer and wider. During growth, material is lost due to homogeneous nucleation and growth in solution, depleting nutrients away from the seeded substrate where growth is desired. While the increase in pH should cause ZnO to precipitate out, the ammonia groups complex with the Zn^{2+} ions to inhibit nucleation. The ammonia slowly evaporates and release Zn^{2+} for the reaction to progress. Using this system, it is possible to produce uniform and long nanowire arrays.

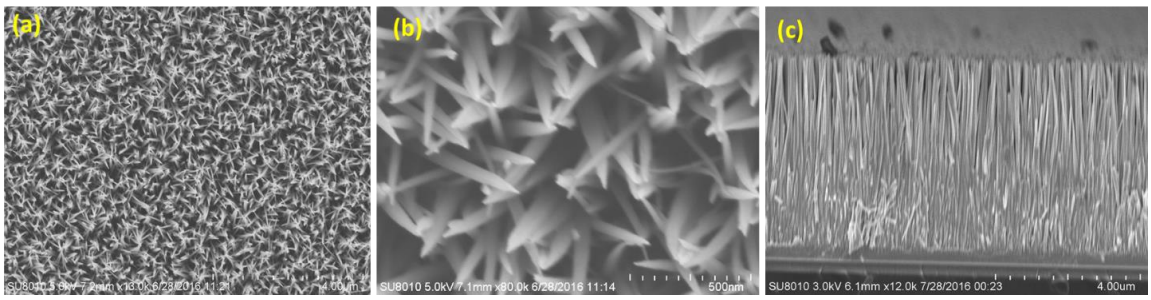

Figure 7 (a-b) Top view of ZnO nanowire arrays at low magnification and high magnification. (c) Cross-section view of ZnO nanowire arrays.

2.2 A-axis GaN Nanowires

A rational method was proposed to grow controllable GaN-based nanowire heterostructures on patterned (100) silicon by metal organic chemical vapor deposition (MOCVD). By adjusting the pattern on the silicon substrate and tuning the growth parameters, the spatial density, dimension and chemical composition of nanowires can be controlled precisely and effectively.

To fabrication of patterned Si (100), this procedure started from depositing a 100-nm-thick SiO2 film on Si (100) substrates by plasma-enhanced chemical vapor deposition. The SiO2 periodic stripes (2 μm spacing/2 μm width) along the <1120 > direction of GaN were formed by photolithography and wet chemical etching. The substrates then underwent anisotropic etching in a KOH solution (30 wt %) at 40 ℃ solution to fabricate 400-nm-deep trapezoidal grooves with two opposed Si (111) facets separated by a bottom Si (100) facet. After that, the periodical lateral ditches with spacing of 3000 μm, width of 10 μm and depth of 30 μm, perpendicular to the <110 > direction of Si, was fabricated by inductive coupled plasma-reactive ion etching. The trapezoidal grooves along the <1120 > direction are perpendicular to the lateral ditches and severed periodically by them. Prior to growth, the substrates were immersed in HF (7 %) to yield an oxide-free hydrogen-passivated Si surface. Thereafter, the substrates were cleaned with deionized water and loaded into a metal-organic chemical vapor deposition reactor for epitaxial growth.

Nanowire structures were synthesized on a patterned Si (100) substrate in a metal–organic chemical vapor deposition reactor (Thomas Swan Scientific Equipment Ltd) using trimethylgallium (TMG), trimethylAluminium (TMAl), trimethylindium (TMIn) and ammonia (NH3) as Ga, Al, In and N sources, respectively. GaN cores were selectively grown on the two opposite Si (111) facets in hydrogen at 1050 ℃ and 400 mbar for 800 s

using TMG (50 standard-state cubic centimeter per minute (sccm)) and NH3 (5000 sccm). Under this condition, the diameters of most GaN cores were of 700–800 nm.

The nanowires/patterned silicon substrate was immersed in BOE solution to eliminate SiO2 mask layer. Afterward, it was ultrasonicated in ethanol for 30 min after etching in KOH (30 wt %) at 40 ℃ solution for 20 min to separate the nanowires from the patterned silicon substrate. The residue was then separated by centrifuging the solution at 1000 rpm for 30 s and decanting, thereby eliminating most of the Si particles from the solution. For the structure and optical analysis, nanowires were transferred by dropping a small droplet of nanowire suspension on an oxidized Si (600 nm thermal SiO2) substrate allowed to dry.

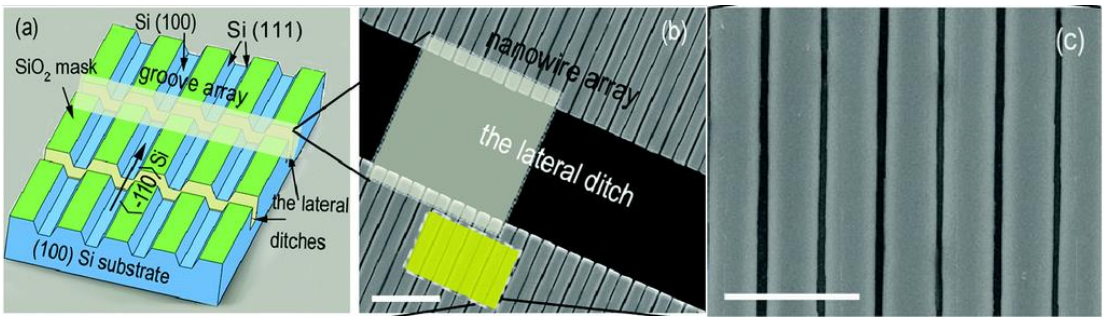

Figure 8 (a) Schematic illustration of the patterned silicon substrate. (b) SEM images of the nanowires in the plane of the Si substrate; scale bar is 3 µm. (c) SEM images of the nanowire array; scale bar is 2 µm.

Figure 8a schematically shows the prepared patterned Si substrate. The trapezoidal grooves along the <110> axis of the Si substrate are perpendicular to and periodically severed by the lateral ditches. Two opposite Si (111) facets of the trapezoidal groove are separated by a bottom Si (100) facet. According to the epitaxial relationship between GaN and Si, the growth of GaN-based nanowires was performed on the sidewall of Si (111) facets selectively. The length of nanowires, corresponding to the length of trapezoidal

groove trenches, can be adjusted by varying the distance between the adjacent lateral ditches. Figure 8b and c are the representative SEM images of the synthesized nanowires arrays in the plane of patterned Si. Figure 9 show the cross section images of the substrate.

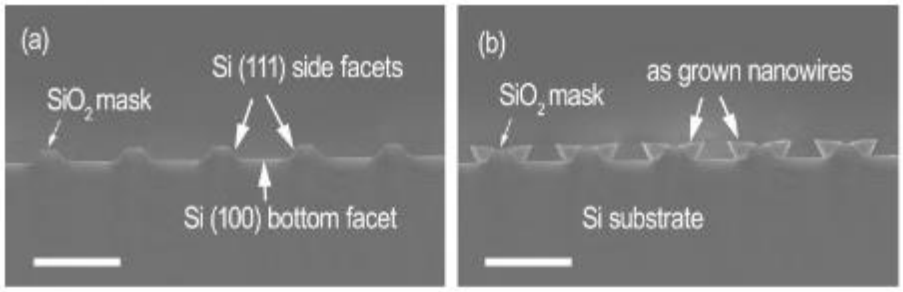

Figure 9 (a) Cross-sectional SEM images of the patterned Si substrate; scale bar is 4 μm; (b) Cross-sectional SEM images of the as grown nanowire on the patterned silicon; scale bar is 4 μm.

2.3 CdS_xSe_{1-x} Nanowire

CdS_xSe_{1-x} NWs were fabricated via a simple one-step chemical vapor deposition (CVD) process in the presence of Sn catalyst. Briefly, the mixed semiconductors powders of CdS (0.1g, Alfa Aesar, 99.995% purity), CdSe (0.05g, Alfa Aesar, 99.995% purity) and SnO_2 (0.01g, 99.5% purity) was selected as source materials and were placed in the central of the tube furnace. Several pieces of Si wafers were placed separately about 6-10 cm to the center downstream. Typically, the temperature of the central site was hearted to 1000°C at a rate of about 50°C /min, kept at this temperature for 60 min, and then naturally cooled to room temperature. During the growth process, the 40 sccm mixture of carrier gas (Ar+H_2 (10%)) was pumped into the tube. After the reaction, bright-yellow to brown-red products were deposited on the surface of silicon wafers and on the inner wall of the quartz tube at the deposition temperature of 600-800 °C downstream. Then, the morphology and composition of the product were characterized by scanning electron microscope (SEM:

Hitachi SU8010) and transmission electron microscope (TEM: FEI F30) with an Energy Dispersive X-ray Spectrum (EDS). The structure was investigated by X-ray powder diffraction (XRD, Siemens D-5000). The room-temperature photoluminescence (PL) measurements were carried out by exciting the sample with a 488 nm Ar-ion laser within an optical cryostat.

CHAPTER 3. PIEZO-PHOTOTRONIC EFFECT ON PHOTOVOLTAICS PROCESSES

3.1 Broadband Photodetector Based on p-Si/n-ZnO Nanowire Arrays

3.1.1 Sensitivity and Responsivity from Near-UV to Near-IR

Extensive applications of photodiodes in communication systems, medical, thermal imaging, environmental monitoring, and defense technology,[20-27] have increased the need for high-speed, sensitive broadband photodetectors. Silicon is the most used semiconductor for discrete devices and integrated circuits, on account of the excellent compatibility with integrated circuits and fast development of nanofabrication techniques and nanomaterials.[28-30] However, for silicon photonics, because of its weak absorption over the wavelength band 0.9 μm due to the indirect absorption mechanism[31, 32] and highly reflective surface across the electromagnetic spectrum,[33] Si-based broadband photodiodes indicate an unsatisfactory response to a wide wavelength range of lights.

Most of the reported silicon-based nano/micro-sensors are still suffering from difficulties of further improving the responsivity and lacking of adjustability. Piezo-phototronics is an effective approach to tune/modulate the charge carries generation, separation or recombination, transport of electron-hole pairs at the interface/junction by the piezoelectric potential. The piezoelectric potential is generated due to dipole moments caused by strains in a noncentrosymmetric wurtzite semiconducting crystal.[34-37] Significant improvements have been demonstrated on the performance of solar cells,[38] photodiodes,[39, 40] light-emitting diode,[41, 42] and even electrochemical processes and energy storages.[43]

Although, extensive investigations in piezotronic and piezo-phototronic effects in both theoretical analysis and device applications have been carried out, the tuning effects are studied based on the charge carriers of both electrons and holes in the depletion region. In order to develop a full understanding of the theory of piezotronics and enable the development of a high-performance electronics, optoelectronics, smart MEMS/NEMS and human-machine interfacing, it is essential to investigate how the piezo-phototronic effect influences on the electron or hole transport at the interface separately, and how these affect the performance.

Here, we fabricated high-performance broadband photodiodes based on p-Si and vertical ZnO nanowire arrays heterojunction operating in the wide range of lights from visible to NIR wavelengths. The performances are significantly enhanced by applying the piezo-phototronics effect because of the modification of the interface properties at the Si/ZnO heterojunction. The enhancement of responsivity could reach a maximum of 78% for 442 nm illumination, and 18% for 1060 nm illumination. The linearity and saturation limit of 1060 nm light detection are significantly increased by applying external strains. Our results show that the fabricated p-Si/n-ZnO nanowire arrays heterojunction photodiodes have high sensitivity, fast response, and great stability, which are entirely suitable for operating at relatively high-speed response conditions in wide spectral bandwidth for various applications, such as nanorobotics, imaging, medical, analytical fields, optical-fiber communication systems.[22] Furthermore, by employing two different wavelengths of lights, electrons-hole pairs are excited only on one side of the depletion region so as to restrict the kind of carriers (either electrons or holes) flowing across the interface of p-n junction in the depletion region. In this way, the type of the charge carriers

could be controlled at the interface of p-n junction, thus the piezo-pototronics on the transport of either electrons or holes could be studied separately. The strain effect on the response time of the photodiodes is also studied in a systematic manner. These are all important and essential to study the basic principles to develop a full understanding of the theory of piezotronics and enable the development of the better performance of optoelectronics, solar cell, light emission diodes, and so on.

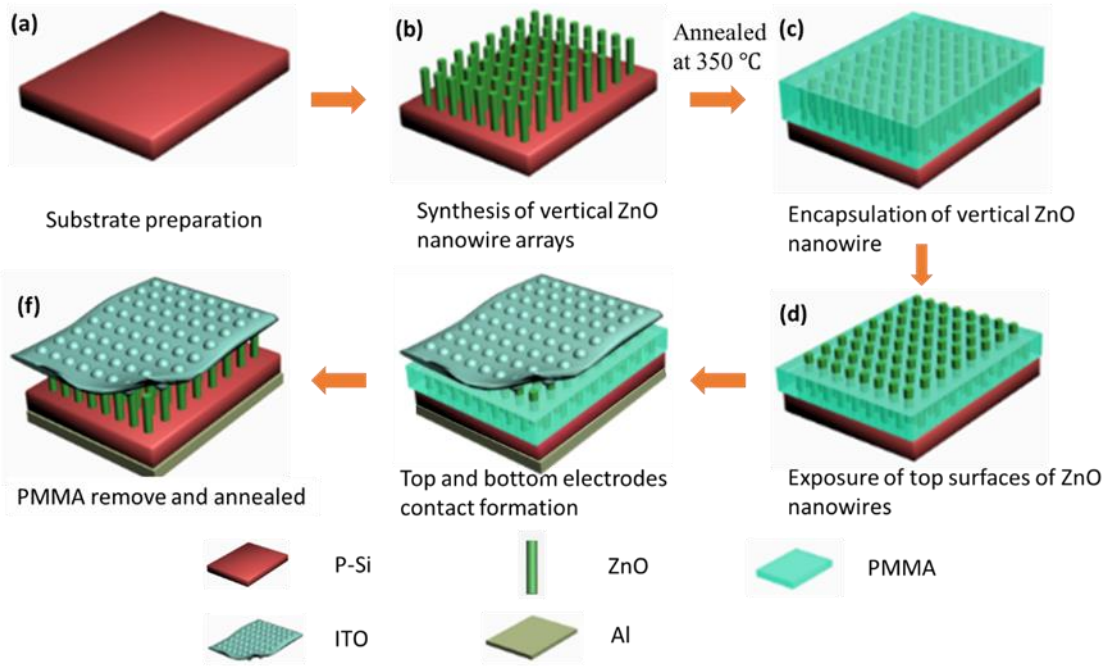

Figure 10 Schematic illustration of processing steps for fabricating the p-Si/n-ZnO nanowires array broadband photodiode.

The fabrication process of p-Si/n-ZnO broadband photodiode is schematically illustrated in Figure 10. A piece of p-type Si wafer (about 10 mm × 10 mm) was cleaned by acetone, isopropyl alcohol, and deionized (DI) water, and then was dried via a Nitrogen gas gun. A thin seed layer (100 nm) of ZnO was sputtered on the silicon wafer, for hydrothermal growth of ZnO nanowire arrays at 95 ℃ for 90 minutes with diameters of 70-100 nm and length of ~2 μm. Figure 11a shows the top view of ZnO nanowire arrays

on a large scale to demonstrate the uniformity of the ZnO nanowire arrays. As indicated in Figure 11b, the samples have a strong XRD diffraction peak at $2\theta=34.5^{\circ}$, corresponding to the (0002) plane of Wurtzite ZnO, which is responsible for the piezoelectric property. The ZnO nanowires have a high degree of alignment and are grown along +c axis on (100) plane of Si substrate. Then the samples were annealed at 350 °C for 2 hours. If the ITO electrode was directly deposited, the ITO could go deeper into the bottom through the gaps between the nanowires, and contact with p-Si or seed layer, causing short circuit and current leakage. To avoid these, a special design of mushroom-like ceiling top electrode is proposed. ZnO nanowire arrays were firstly fully encapsulated by a layer of PMMA via spin coating and etched by oxygen plasma for 4 minutes to expose the top tips of the nanowires. The side-view and 30° tilt view SEM images (Figure 11c, d) show that the tips of ZnO nanowires were exposed. Indium-tin oxide (ITO) with the thickness of ~100 nm was deposited on the exposed tips of the nanowires to create core shelled ZnO/ITO and flat PMMA plane to form a continuous ITO film. The top electrode then has a mushroom-like nanostructured surface as the top surface and a flat surface at the bottom. From Figure 11e, the sharp tips of the nanowires turn into round heads like mushrooms, which are fully core-shell covered by ITO, and connected with each other via continuous ITO film. Aluminum was deposited on the back of p-Si wafer as the bottom electrode. Devices were cleaned by acetone to remove the PMMA, and then were heated to 350 °C again for burning out all PMMA residues, building up better Al-Si contact, and improving the transmission of ITO. Figure 11f shows the 30° tilt view SEM image of the edge of the device after applying compressive strains repeatedly. The PMMA was all removed leaving the empty space between the nanowires. The continuous ITO film is supported by nanowires. We have

found that the contact was firm and the nanowires showed the necessary flexibility, even when the p-Si substrate was cracked due to the excessive compressive strain, the ITO electrode and nanowires were not damaged or broken. Thus, the mushroom-like ceiling top transparent electrode was formed. It provides a novel method for fabricating top electrodes for nanowire arrays, allows for annealing at high temperature for nanowire arrays, and eliminates the direct contact of the top electrode and bottom layer. Such special design is later found to significantly contribute to a low dark current, high rectifying ratio and light absorption.

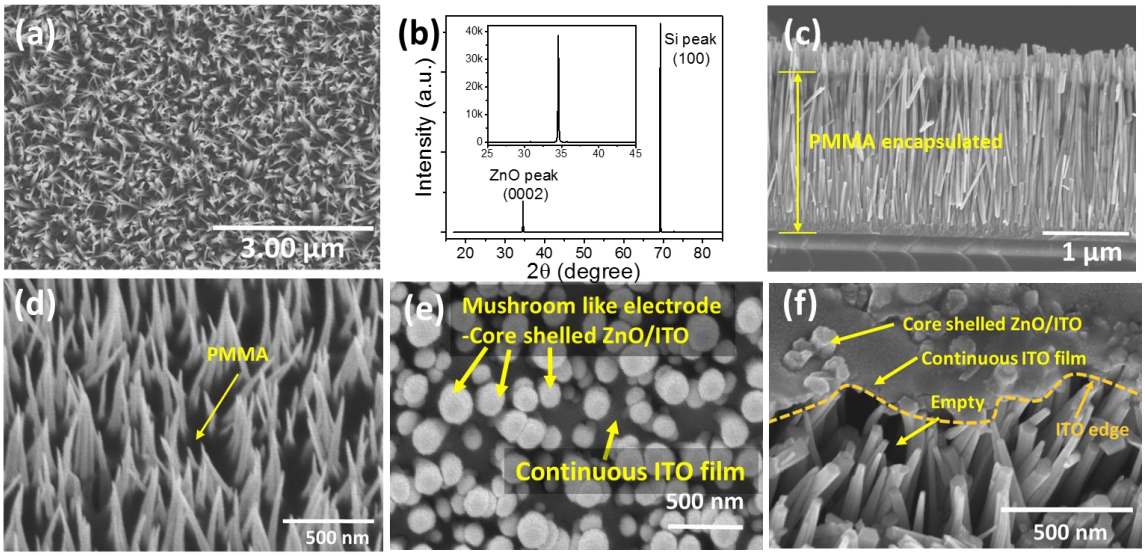

Figure 11 Device fabrication and characterization. SEM images of n-ZnO nanowires from (a) top view before PMMA spin coating, (b) XRD diffraction pattern obtained from the ZnO/p-Si heterostructure, (c) side view and (d) 30° tilt view of p-Si/n-ZnO heterojunction after PMMA spin coating and oxygen etched, (e) ITO coating as top electrode. (f) 30° tilt view of ITO coating at the edge of the device after applying strains repeatedly.

Silicon has a weak absorption of the light over the wavelength of 0.9 µm due to the indirect absorption mechanism.[31] For this hybridized broadband photodiode, the absorption in this region was greatly enhanced due to the nanostructured/textured top surface of ZnO

and ITO (Figure 12a). The mushroom-like ceiling ITO electrode has a textured structure top surface that acts as an anti-reflection coating layer to reduce the reflection of NIR light, and it also has a flat surface at the bottom to enhance the reflection so that light could be reflected back again to be absorbed. To illustrate the photoresponse of different materials, a reference sample of ZnO nanowire arrays was grown on a glass (2 μm thick) with the same preparation conditions. The absorption spectra (Figure 12a) and transmission spectra (Figure 12b) show that n-ZnO nanowires are transparent to 1060 nm wavelength light because photons have less energy ($h\upsilon<E_g$) than the band gap needed to generate electron-hole pairs in ZnO; because of the by local defect levels within the band gap,[35, 44-46] the ~2 μm thick of ZnO nanowire arrays absorb most of 442 nm wavelength light, the light intensity is greatly reduced when the light transmitted through the ZnO nanowires and the part (<4%) absorbed by p-Si are negligible.

Figure 12c shows the I-V characteristic of the broadband photodiode in dark (black line), under the illumination of 442 nm (red line) and 1060 nm (purple line) with power densities of 26.45 mW/cm^2 and 18.9 mW/cm^2, respectively. The photodiode presents a typical rectifying characteristic of a p-n junction diode between -2 to 2 V. Figure 12d shows the sensitivity of the device measured under photoconductive mode at a reversed bias of -2 V, under different power densities of illumination. The sensitivity defined as $(I_{light} - I_{dark}) / I_{dark}$ [47] is found to be about 5200% and 4000% (Figure 12d) at the power densities mentioned above. The photodiode still has a good sensitivity of 450% at low power densities of 0.3 mW/cm^2 for 1060 nm light, and 650% at 0.62 mW/cm^2 for 442 nm light.

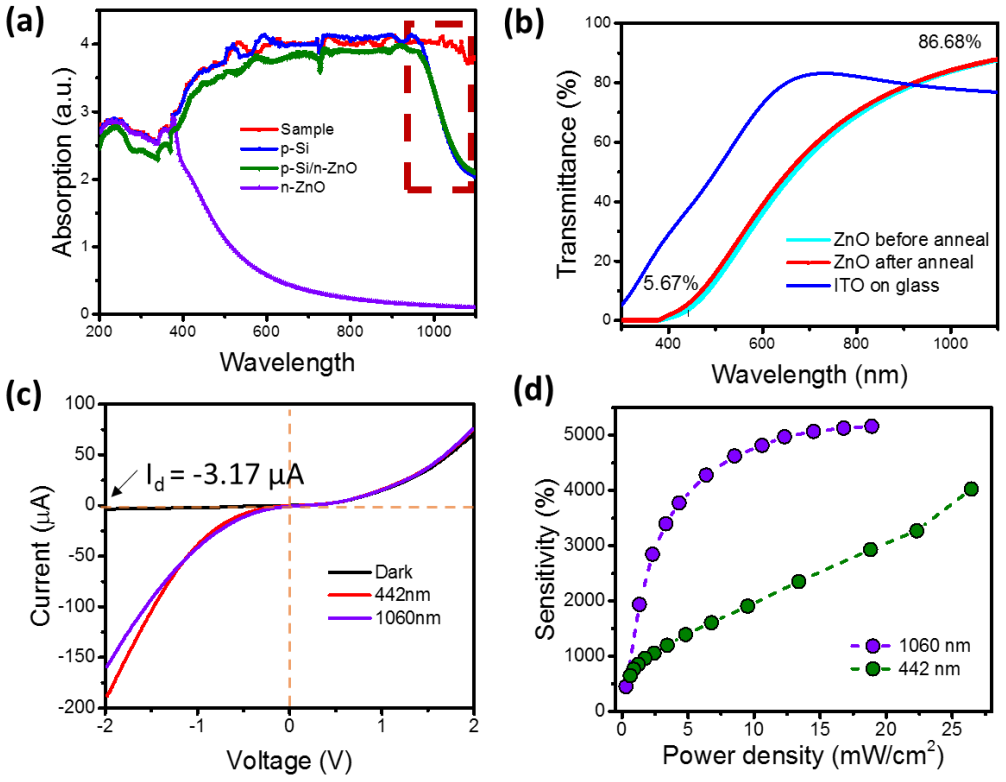

Figure 12 Optical properties of the device. (a) Absorption spectra of p-Si, n-ZnO, p-Si/n-ZnO nanowire arrays without top electrode, and the sample with mushroom-like ceiling top electrode. (b) Transmission spectra of ITO, ZnO NWs array on the glass before annealed and after annealed. (c) I-V characteristics of the device in dark, under the illumination 442 nm and 1060 nm wavelength with the power densities of 26.45 mW/cm^2, 17.42 mW/cm^2 respectively. (d) The sensitivity of the device under different illumination power densities.

The broadband photodiodes exhibit good photosensing properties under the illumination of light at wavelength ranged from 442 nm to 1060 nm at low power consumption (-2 V). The rise time, defined as the time interval for the response to rise from 10 to 90% of its peak value,[31, 48] is 1.071 ms under 442 nm light with 0.62 mW/cm^2 and 0.849 ms under 1060 nm light with 3.32 mW/cm^2 at the on-off frequency of 20 Hz. Similarly, the fall time, defined as the time interval for the response to decay from 90 to 10% of its peak value, is 1.304 ms for 442 nm light, and 1.277 ms for 1060 nm light, at the conditions mentioned above respectively. The broadband photodiode has excellent stability and repeatability as shown in Figure 13a and b, as there is no observable deviation for more than 50 cycles.

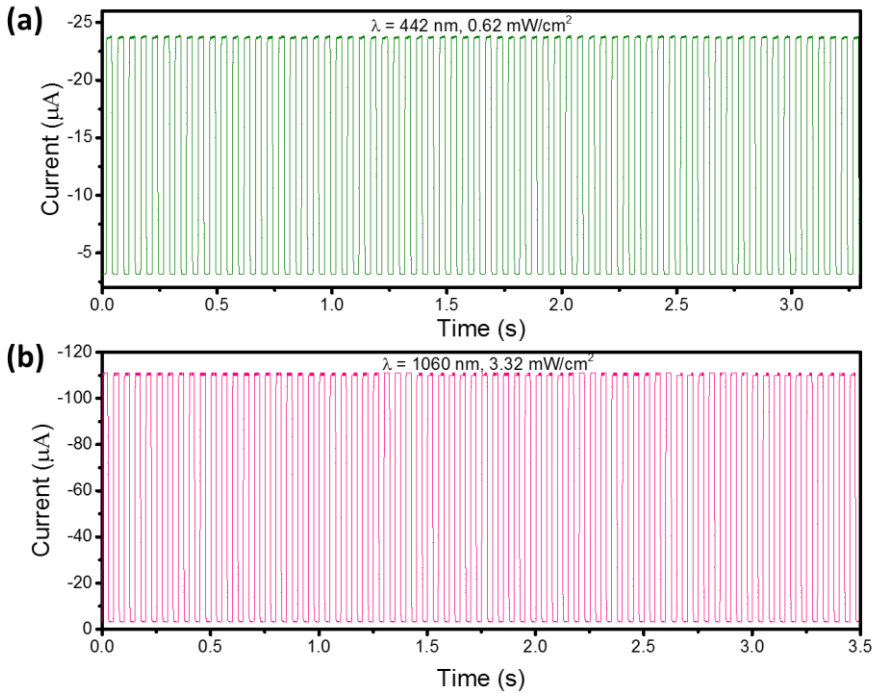

Figure 13 Repeatability and time response of the device under (a) 442 nm light with a power density of 0.62 mW/cm^2 and (b) 1060 nm light with a power density of 3.32 mW/cm^2. The chopper on/off ratio is about 20 Hz. The devices were all measured at -2 V bias voltage.

Consequently, the results imply that the p-Si/n-ZnO heterojunction photodiodes have good performance, and are entirely suitable for operations at relatively high-speed conditions, as compared to other nanostructure photodiodes, as shown in Table 1 and some commercial silicon photodiode.[49, 50] The excellent photoresponse characteristic of ZnO significantly attributes to some factors such as the presence of defect concentration in the ZnO grown, quality of ZnO nanowires, crystallographic orientation, and processing condition.[51]

Table 1 A comparison of photosensing properties for various nanostructure photodiodes.

Material and structure	Device type	Light of detection (nm)	Bias (V)	Dark current	Current	Rise time	Fall time	Reference
ZnO NW arrays/p-Si	p-n junction	442-1060	-2	3.17 μA	131 μA (442 nm) 167 μA (1060 nm)	0.97 ms (442 nm) 0.84 ms (1060 nm)	~1.30 ms (442 nm) ~1.28 ms (1060 nm)	Our work
ZnO nanorods	M-S	450	-	1 nA	~25 nA	3.7 s	~60 s	[52]
ZnO hollow-sphere nanofilm	M-S	350	5	50 nA	2.6 μA	<5 ms	<5 ms	[53]
ZnS/ZnO	p-n junction	320	1	0.2 μA	1.0 μA	<0.3 s	~1.7 s	[54]
ZnO NWs/i-MgO/n-Si	n-i-n	365	-5	~6.4 nA	~8.6 μA	<160 ms	<350 ms	[55]
ZnO NW arrays/p-Si	p-n junction	442	2	60 μA	60 μA	110 -229 ms	57 ms	[56]
TiO_2 nanorod/p-Si	p-n junction	405	3	~70 μA	~140 μA	9 ms	9.7 ms	[57]

The piezo-phototronic effect was applied to modulate the optoelectronic processes and the performance as well, the experimental set-up is shown in Figure 14. Under various strains, the broadband photodiode was first illuminated by 442 nm light, and then 1060 nm. I-V characteristics were measured under the high intensity of illumination with the power density of 26.5 mW/cm^2 of 442 nm light, then 18.9 mW/cm^2 of 1060 nm light, which are shown in Figure 15a and d.

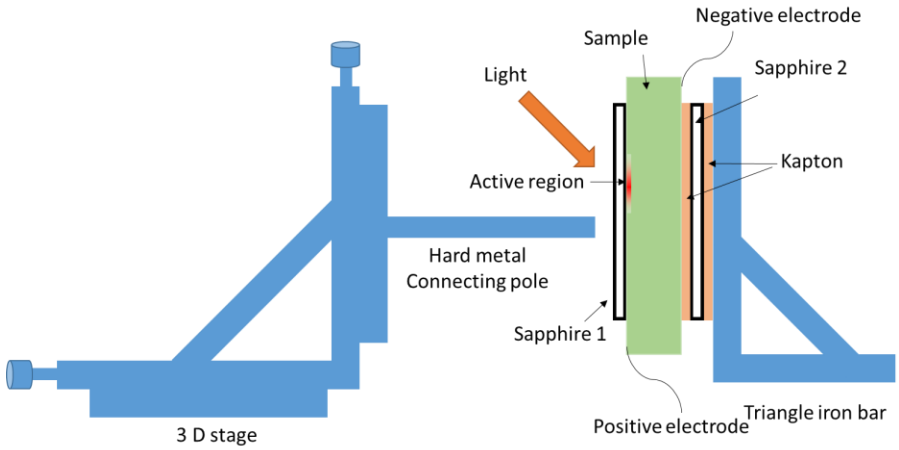

Figure 14 Experiment set-up and measurement system. External strains are applied onto the p-Si/n-ZnO PD by pressing the surface of the device through a piece of sapphire.

The amount of strain applied to the ZnO NWs is calculated based on Young's modulus ratio among different materials by assuming a uniform distribution of forces among each layer of the device for the state of mechanical equilibrium. Tensile strain is defined as positive and compressive strains as negative.[41] The insets are the enlarge figures showing that under the above illumination conditions, the output current over various strains increases as the strains go higher from 0% to -1.42%. The intensity dependences of photocurrents ($|\Delta I| = |I_{light} - I_{dark}|$) under different strains are plotted in Figure 15b,d. When the samples are illuminated at 442 nm, the photocurrent all rises as the strain increases between the power density of 0.6-26 mW/cm^2, as shown in Figure 16a. From Figure 15d, when the samples are illuminated at 1060 nm without strains, the photocurrent has a saturation limit at high power levels (above 16 mW/cm^2), that there are no additional photocurrent outputs from the photodiode as the incident optical power increases.

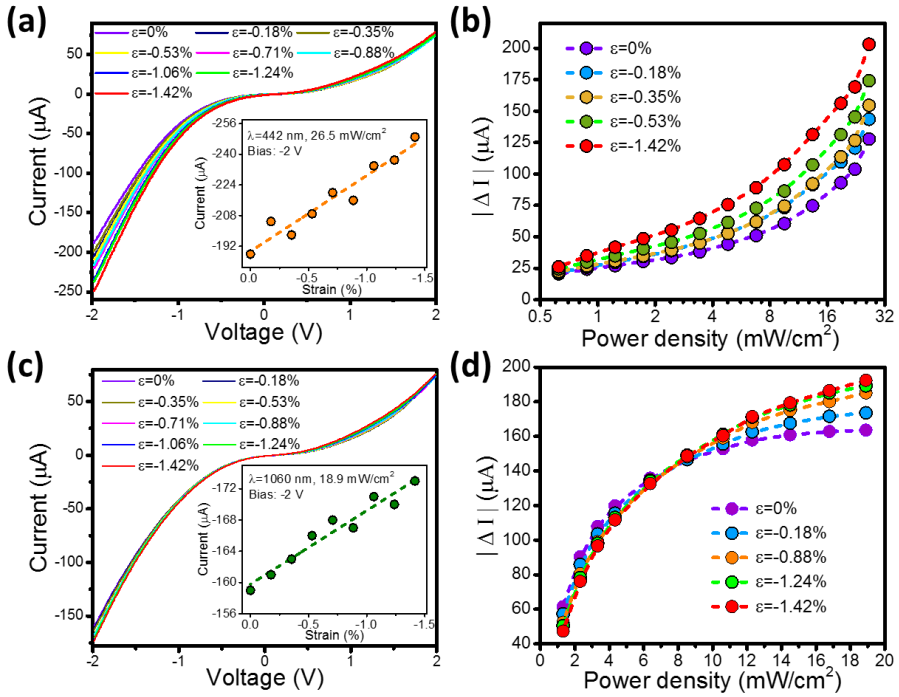

Figure 15 Piezo-phototronic effect on photo response. I-V characteristics of the device under illumination of (a) 442 nm and (d) 1060 nm wavelength with the power densities of 26.5 mW/cm^2, 18.9 mW/cm^2 respectively. The insets are the output current under different strains at -2 V bias voltage at the above illumination condition. Photocurrent of the device under (b) 442 nm, (e) 1060 nm under different strains and illumination conditions, biased at -2 V.

By applying compressive strains, the device showed a better linearity and higher saturation limit, which demonstrates that the photo response is greatly enhanced (Figure 15d), even though the photocurrent decreases with the strains increases at low illumination power levels (below 6 mW/cm^2, Figure 16b). When the applied strain increases at high illumination power levels of 1060 nm light (above 10 mW/cm^2), the photocurrent increases. The turning point of photocurrent under compressive strains from decreasing to increasing under the illumination of 1060 nm light is about 7 mW/cm^2. This is because that the flowing free electrons at the interface would be trapped by local immobile piezoelectric positive charges at low intensity of illumination; while at high intensity of illumination, the large photocurrent would screen part of the piezoelectric potential (a dip is not created), so

that the trapping force would be much lower, and the enhanced built-in field would be easier to promote electron transition from the p-side to the n-ZnO side. This will be further explained by bandgap diagram in Figure 19.

The total responsivity of the photodiode, R, is defined as

$$R = \frac{I_{light,s} - I_{dark,s}}{P_{ill}} = \frac{\eta_{ext}}{hv}\Gamma_G \qquad (10)$$

where $P_{ill} = I_{ill} \times S$ is the illumination power on the photodiode, $I_{light,s}$ and $I_{dark,s}$ represent the photon and dark current respectively under the corresponding external strain, Γ_G is the internal gain, η_{ext} is the external quantum efficiency (EQE), q is the electronic charge; h is Planck's constant, v is the frequency of the light; I_{ill} is the excitation power density, and S is the effective area of the photodiode.

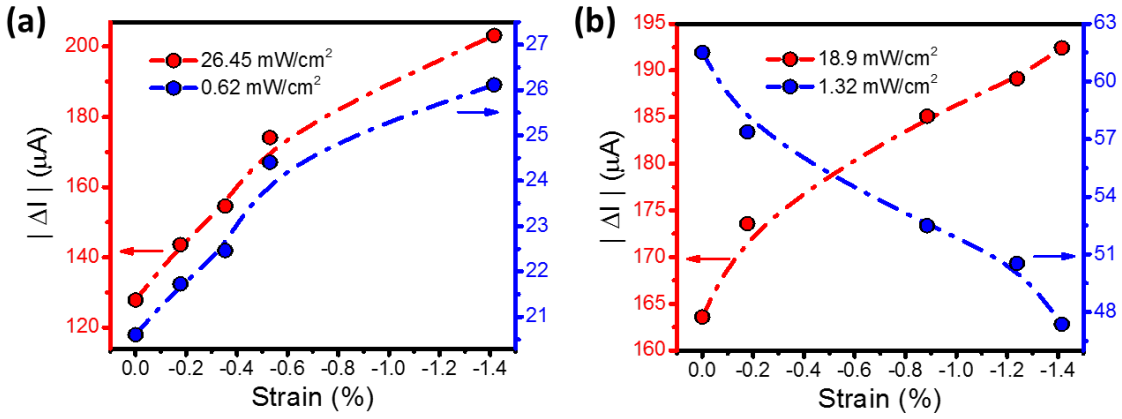

Figure 16 The enlarge figure of photocurrent under different compressive strains at (a) 442 nm light with relative high power densities of 26.45 mW/cm^2 (red dots and dash line) and 0.62 mW/cm^2 (blue dots and dash line) and (b) 1060 nm light with a relatively high power density of 18.9 mW/cm^2 (red dots and dash line) and a low power density of 1.32 mW/cm^2 (blue dots and dash line).

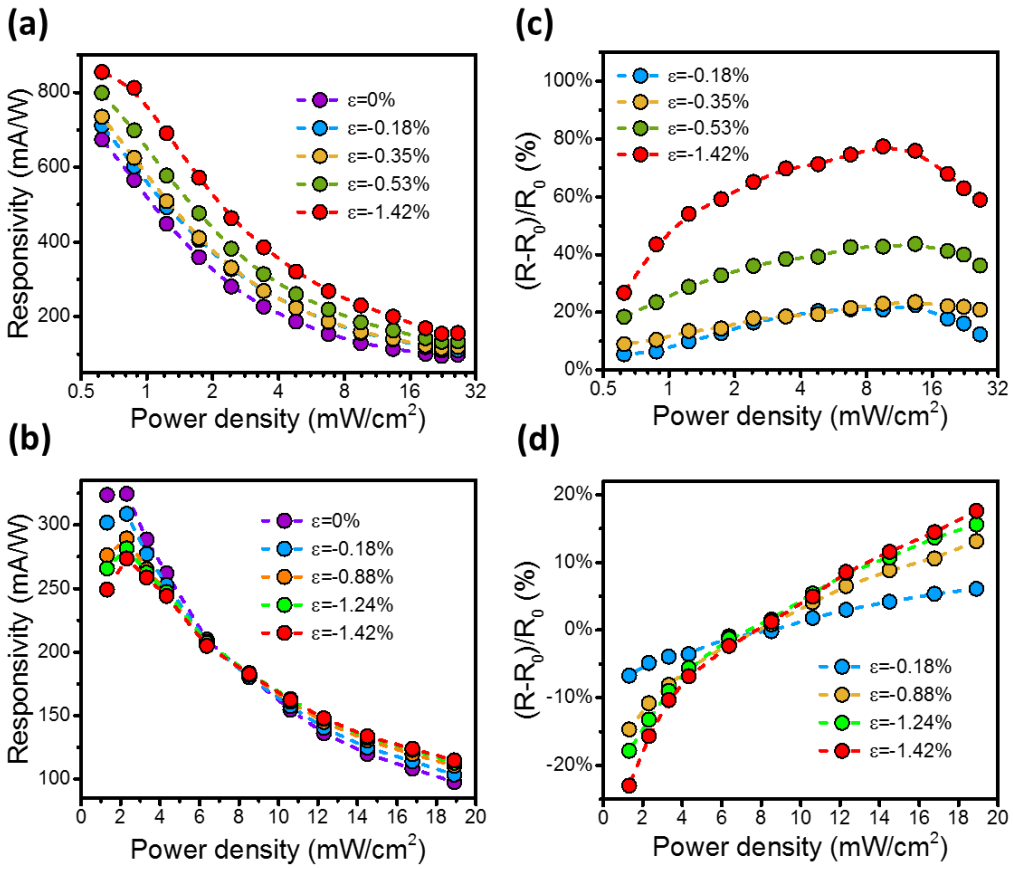

Figure 17 Piezo-phototronic effect on responsivity. Photo responsivity (a-b) and relative changes (c-d) of photoresponsivity of the device under different strains and illumination conditions, biased at -2 V. (a, c) are under the illumination of 442 nm wavelength, and (b,d) are under the illumination of 1060 nm wavelength.

The photoresponsivity R is calculated as shown in Figure 17a and b for all the power density under various external strain conditions at the reverse bias of -2 V. When compressive strain increases at the 442 nm light, the responsivities of device increase. However, under the 1060 nm light, the responsivity decreases first and then increases with the turning point at about 6-8 mW/cm^2. The relative change of responsivity is shown in the Figure 17c and d, which is defined as $(R-R_0)/R_0 \times 100\%$, where R is the responsivity under certain strain, and R_0 is the responsivity without strain. The enhancement can reach maximum 77.5% for 442 nm illumination, and 17.6% for 1060 nm illumination.

3.1.2 Selective Electrons or Holes Transport

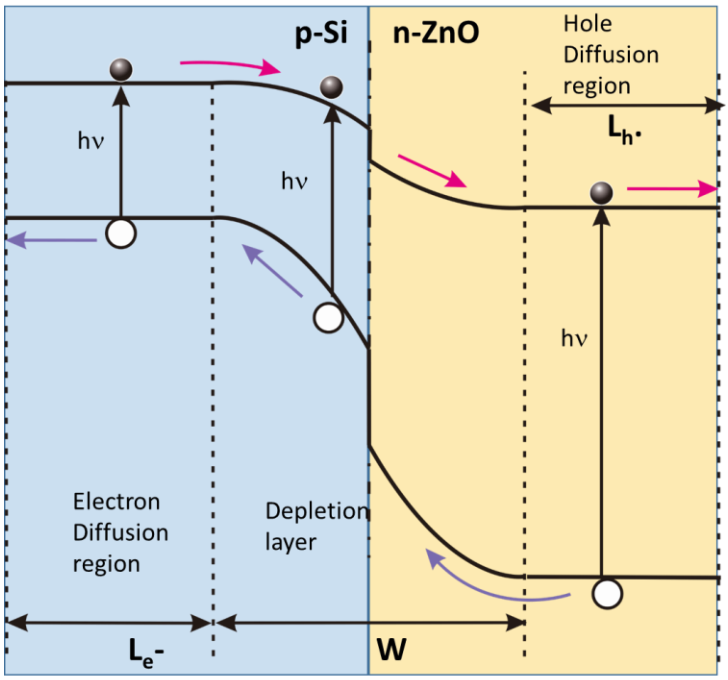

Figure 18 Working mechanism. Photoexcitation and energy-band diagram of the broadband photodiode.

For a semiconductor p-n junction photodiode, the photo-generated charge carriers are normally generated in two active regions: the depletion layer and the diffusion regions.[31] When the devices were illuminated at 442 nm at low power levels of illumination, the charge carriers were generated in the diffusion region near the surface (e.g., ZnO); while at high power levels, it would penetrate through the surface to a deep depth near or in the depletion layer. The 1060 nm wavelength light penetrates through the ZnO layer, and directly reaches the depletion layer at the interface/junction. When the intensity of light increases, the active regions would also include the diffusion region. The electrons in the p-side diffusion region or the holes in the n-side diffusion region, can reach the depletion by diffusion and then are swept to the other side by the internal field. The

same is true for the minority carriers generated in the depletion region, as illustrated in Figure 18.

The band diagrams of the p-Si/n-ZnO heterojunction broadband photodiode are shown with reversed biased voltage under the illumination of 442 nm (Figure 19a) and 1060 nm (Figure 19b) with external compressive strain based on Anderson's model.[58, 59] The band gap and electron affinity values for Si and electron affinity values for Si and ZnO are $E_{g,Si}$=1.12 eV, χ_{Si}=4.05eV[58] and $E_{g,ZnO}$=3.37 EV, and χ_{Si}=4.35,[60] respectively. There are a conduction band edge offset ΔE_c=0.3 eV and a valence band edge offset ΔE_v=2.55 eV.

As discussed above, the ~2 μm ZnO nanowire arrays have almost a full absorption of 442 nm light and are completely transparent to 1060 nm light. Upon visible 442 nm wavelength light, electron-hole pairs are generated only in the n-ZnO region and the transport of free electrons and holes upon the electric field results in an increase of output current. Under such conditions, due to the electric field effect, we consider only holes that pass through the depletion regions, and electrons are directly migrated to the electrode side (Figure 19a, the red arrowhead is marked with a black cross, which means that few electrons flow across the interface in this case). Similarly, upon the illumination of 1060 nm light, electrons and holes are only generated on the p-Si side. No photoexcited holes transport through the depletion region to the p-Si side, instead they are directly collected at the electrode side under the applied bias (Figure 19b, the purple arrow is marked with a black cross, which means that no hole flows across the interface).

We now consider the case of strong illumination intensity of 442 nm or 1060 nm lights above ~9 mW/cm^2, with the corresponding band structure shown as stage (i) in Figure 19(a, b) (dark dashed lines). When a compressive strain is applied along the c-axis of ZnO, the band structure is shown as stage ii in Figure 19(a,b) (light blue lines), positive polarization charges are induced within the depletion region.

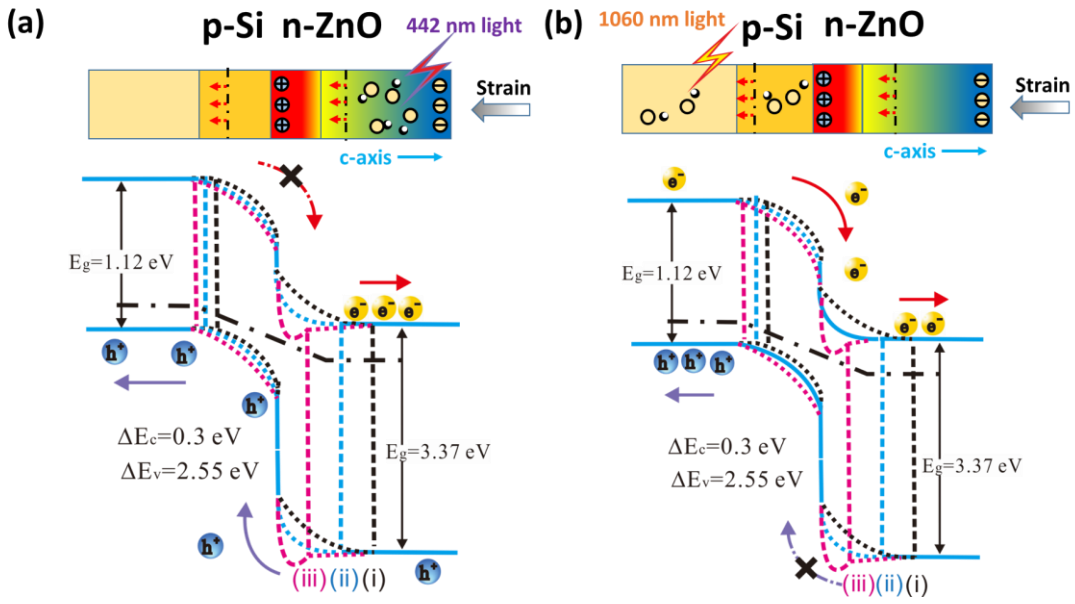

Figure 19 Schematic band diagrams of a p-Si/n-ZnO heterojunction under compressive strains applied to illustrate the working mechanism of piezo-phototronic effect under the illumination of (b) 442 nm and (c) 1060 nm wavelength. For the color gradient, red represents positive potential and blue represents negative potential. The black, blue and red dash lines show the energy band at different stages (i), (ii), (iii) under high illumination without strains, high illumination with strains, and low illumination with strains.

The piezo-charges will be mostly preserved without being screened by local residual free carriers, because the presence of depletion region can significantly enhance the piezoelectric effect. The conduction and valence bands in the junction region are lowered locally, the depletion layer will shrink on the n-type side and expand on the p-type side.[59, 61] Note, a dip is not created at the interface due to the screening effect of the light-

induced electrons to the piezoelectric charges. As shown in Figure 19(a,b), the edge of depletion shift from the position of the black short dash lines (stage (i)) to the position of blue dashed lines (stage (ii)), thus increasing the barrier height. It will strengthen the built-in field and reduce the recombination that leads to having a higher collection probability for the carriers,[38, 47] leading to the increase of photocurrent; simultaneously, the responsivity is increased under compressive strain. Therefore, when strain is introduced under the high illumination intensity, the piezoelectric polarization on the n-ZnO side can effectively modulate the redistribution of charge carriers that leads to the increase of the photocurrent under the illumination of both 442 and 1060 nm lights.

In the case of weak illumination intensity of 442 nm or 1060 nm lights and under compressive strains (stage (iii)), less free electrons and holes are generated and accumulated, reducing the screening effect on the piezoelectrical potential, so that the strain induced polarization charges at the interface have a stronger effect. This results in further downward bending in the local conductive valence band[62] and shrink of the depletion region on the n-ZnO side. The positive piezo-polarization charges will attract and trap some of the photogenerated electrons, which is equivalent to forming a dip at the interface.[35, 59, 61] Consequently, it hinders the separation and reduces the photocurrent generated by the 1060 nm light (stage (iii), see the pinky dashed curve in Figure 19b). The more strain applied, the larger positive piezo-polarization charges displayed, and then more free electrons could be trapped. But for the carriers generated by the 442 nm light, the holes will not be trapped by the presence of the piezoelectric charges (stages (iii), see the pinky dashed curve in Figure 19a), because they are both positively charged, and there is no attraction force between them.

3.1.3 Response Time

Response time is mainly determined by the processes of the generation, separation, recombination and transport of the charge carriers. Therefore, it is very critical to study how the piezo-phototronic effect on the response time since it intimately correlates with these processes. For a given photodiode, the response time is most determined by t_{drift}, the charge collection time of the carriers in the depleted region of the photodiode and $t_{diffused}$, the charge collection time of the carriers in the diffusion region of the photodiode.[22, 31] The carriers have small mobility in n-ZnO, so when we consider the rise time and fall time, we would mostly focus on the n-ZnO side. The rise time is mostly dominated by the carriers' transport in the diffusion region,[31] the fall time here possibly depends on the minority carrier transit time in the depletion region.[31, 48, 63]

For a photodiode operating in photoconductive mode under a reverse bias, the rise time of the photocurrent to an optical signal is determined by two factors: (1) drift of the electrons and holes that are photogenerated in the depletion layer and (2) diffusion of the electrons and holes that are photogenerated in the diffusion regions.[22, 31] The shape of the photodiode response illuminated at 442 nm wavelength with high power density has a fast component that photons absorbed in the depletion regions and slow components which some photons are absorbed in the diffusion regions. The drift of the carriers across the depletion layer is a fast process-given by the transit times of the photogenerated electrons and holes across the depletion layer. Diffusion of the carriers is a slow process, caused by the optical absorption in the diffusion regions outside of the high-field depletion regions.

For the fall time, the solid-state process of recombination of photogenerated electron-hole pairs is important.[63] When light is off, the energy status drops to low level, the photogenerated pairs are largely reduced, they can recombine in the diffusion region before they reached the depletion; but in the depletion layer, there are no the free carriers to recombine, they have to transit through the depletion to the other side. Free carriers remained in the depletion layer has no chance to recombine until they pass through the depletion region to reach the edge, and recombine in the diffusion region to recovery to the original status. The fall time here is possibly mainly determined by the transit time of free carriers through the depletion layer.

We measured the photo response under 442 nm and 1060 nm wavelength light illumination for about 50 cycles at the on-off frequency of 20 Hz under different light intensities. We calculate all cycles' response time and deviation, which is shown in Figure 20. From Figure 20a, under the illumination of 442 nm light from 0.62 to 3.42 mW/cm^2, the rise time rises from 1.2233 to 1.3493 ms when the compressive strain increase to 1.42%. Since it is under the relative low illumination power, the free charge carriers are mostly generated at the surface of ZnO. Electrons are directly collected at the surface, and the diffusion length of electron does not change, but the diffusion length of hole $L_{h\cdot}$ increases because of the shrink of depletion layer on the n-ZnO side (see Figure 19a), which leads to the increase of fall time. From Figure 20b, the fall time all drop by ~ 5%-6% off as the strain increases to 1.42%. The physical model of Figure 19 indicates that when light is off, the holes remained in the depletion layer has less drift length on the n-ZnO side due to the depletion shift. Also, the strain induced positive polarization charges in the n-type region

would repel the holes remained on the p-Si side, which would provide an additional driving force to accelerate the hole migration to recombine and return to equilibrium state.

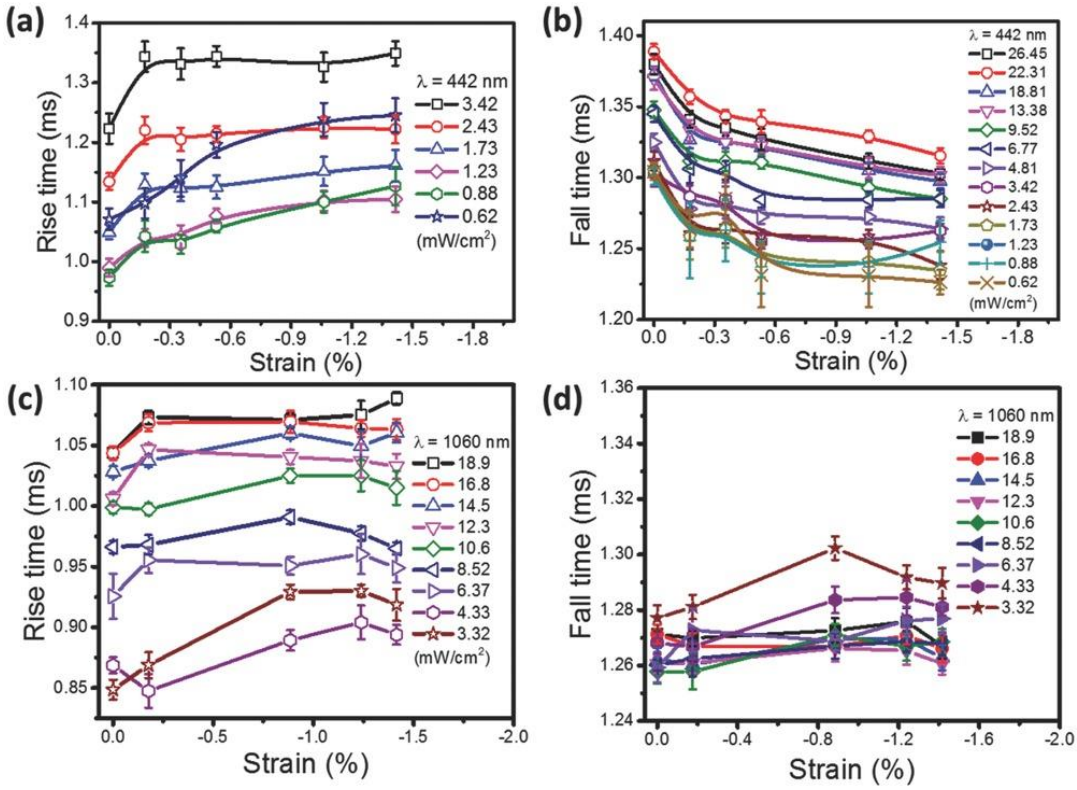

Figure 20 Response time under different compressive strains. The corresponding rise (a) and fall time (b) of the device under different compressive strains, under different power densities of 442 nm (unit: mW/cm2). The corresponding rise (c) and fall time (d) under different compressive strains under different power densities of 1060 nm light. The error bars indicate the range within a standard deviation.

Figure 20c and d show the rise time and fall time with various power densities under different strains, when the devices were under the illumination of 1060 nm. The rise time increases slightly when applied compressive strain increases. The induced positive polarization charges would cause trapping of electrons, and decelerate electrons moving from depletion to electrode. Also, the depletion width of the n side shrink, resulting in the increase of the electrons diffusion length. Both of these contribute to the increase of rise time. There are relatively small changes of fall time caused by strains when it was

illuminated by 1060nm light (Figure 20d). The electron drift length decreases because of the shift of the depletion region, which should reduce the response time. But on the other hand, the strain induced polarization positive charges attract the electrons from diffusing away from the depletion region (see Figure 19b). The two processes counteract against the other, so that the fall time has no significant change under various compressive strains.

3.1.3.1 General principle of the p-Si/n-ZnO nanowires array broadband photodiode

To better explain the complex relationship of current, rise time, strains, and intensity, firstly we have to study on the generation and transmission of charge carriers of this device. The photoresponse of a photodiode results from the photogeneration of electron-hole pairs through band-to-band optical absorption. For a semiconductor p-n junction photodiode, the areas where electron-hole pairs are generated by optical absorption are divided into three parts: the depletion layer, the diffusion regions and the homogeneous regions.[31] In the depletion layer, the immobile space charges create an internal electric field and result in band-bending, as illustrated in Figure 18. When an electron-hole pair is generated in the depletion layer, the internal field sweeps the electron to the n side and the hole to the p side. This process produces a drift current that flows in the reverse direction from the n side to the p side. If an electron-hole pair is generated within one of the diffusion regions at the edges of the depletion layer, the electron in the p-side diffusion region or the hole in the n-side diffusion region, can reach the depletion layer by diffusion and then be swept to the other side by the internal field. This process results in a diffusion current that also flows in the reverse direction. For an electron-hole pair generated in the p or n homogeneous region, no current is generated because there is no internal field to separate the charges and a minority carrier generated in a homogeneous

region cannot diffuse to the depletion layer. Thus, the active region of a photodiode mainly consists of the depletion layer and the diffusion regions. Consequently, the photocurrent of the junction photodiode mainly includes: a drift current from photogeneration in the depletion layer and a diffusion current from photogeneration in the diffusion regions.

In our case, the photoexcited electron-hole pairs illuminated at 442 nm are first generated within the n-ZnO diffusion region near the depletion layer, the hole in the n-ZnO diffusion region can reach the depletion layer by diffusion and then be swept to the other side by the internal field. When the intensity goes higher, the photons can reach the depletion layer to generate electron-hole pairs in the depletion layer in the n-ZnO side. The hole will be swept to the p-Si side and electron will be collected at the electrode side drove by the external electric field.

3.1.3.2 General principles of response time

Transmitted light is attenuated via absorption as it passes through the semiconductor, generation of carriers related directly to the number of photons absorbed.

$$N_{ph} = N_s e^{-\alpha x} \#(11)$$

where N_{ph} is the number of photons, N_s is the photons at the surface, α is the absorption coefficient, x is the distance in the materials. Absorption depth (1/ α) in the material where the light intensity falls by 1/e.

For a photodiode operating in photoconductive mode under a reverse bias, the rise time of the photocurrent to an optical signal is determined by two factors: (1) drift of the electrons and holes that are photogenerated in the depletion layer and (2) diffusion of the

electrons and holes that are photogenerated in the diffusion regions.[22, 31] The shape of the photodiode response illuminated at 442 nm wavelength with high power density has a fast component that photons absorbed in the depletion regions and slow components which some photons are absorbed in the diffusion regions. The drift of the carriers across the depletion layer is a fast process-given by the transit times of the photogenerated electrons and holes across the depletion layer. Diffusion of the carriers is a slow process, caused by the optical absorption in the diffusion regions outside of the high-field depletion regions.

For the fall time, the solid-state process of recombination of photogenerated electron-hole pairs is important.[63] When light is off, the energy status drops to low level, the photogenerated pairs are largely reduced, they can recombine in the diffusion region before they reached the depletion; but in the depletion layer, there are no the free carriers to recombine, they have to transit through the depletion to the other side. Free carriers remained in the depletion layer has no chance to recombine until they pass through the depletion region to reach the edge, and recombine in the diffusion region to recovery to the original status. The fall time here is possibly mainly determined by the transit time of free carriers through the depletion layer.

3.1.3.3 Diffusion time τ_{diff} and diffusion distance

Diffusion of the electrons here is a slow process. The free charge carriers encounter frequent collisions with lattice ions and impurity ions, and suffer random decelerations, which largely increase the rise time. Therefore, diffusion time of electrons τ_{diff} has the dominating effect on the value of response time. Diffusion time of carriers generated

outside the depletion region: carrier diffusion time $\tau_{diff,}$ for carriers to diffuse a distance d is

$$\tau_{\text{diff}} = \frac{d^2}{2D} \tag{12}$$

where D is the minority carrier diffusion coefficient.

3.1.3.4 Drift time τ and depletion layer width W

The constant electric field E presented causes its free charge carriers to accelerate. The accelerated free carriers then encounter frequent collisions with lattice ions moving about their equilibrium positions via thermal motion and imperfections in the crystal lattice (eg. Associated with impurity ions). These collisions cause the carriers to suffer random decelerations. The mean drift velocity of a carrier

$$V_d = \left(\frac{eE}{m}\right)\tau_{\text{col}} = \mu E \tag{13}$$

where m is the effective mass, τ_{col} is the mean time between collisions, $\mu = e\,\tau_{col}/m$ is the carrier mobility.

The longest transit time τ_{tr} is for carriers which must traverse the full depletion layer width W:

$$\tau_{tr} = \frac{W}{v_d} \tag{14}$$

where v_d is the maximum drift velocity.

3.1.3.5 Response time and light intensity

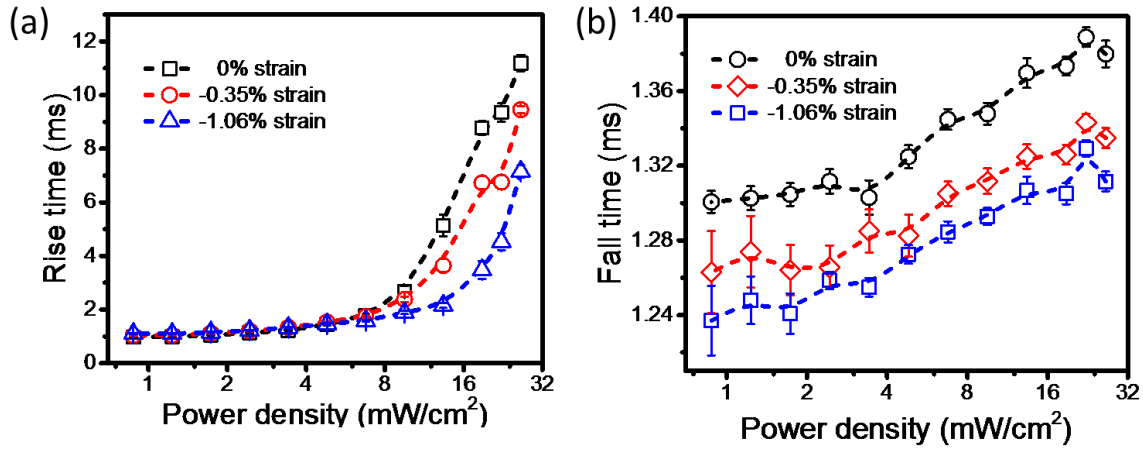

Figure 21 The corresponding (a) rise and (b) fall time of the device under different illumination power density of 442 nm wavelength light, under different strains.

Figure 21 shows the rise time (a) and fall time (b) over various 442 nm light intensity under different strains. When the intensity of light goes higher, the rise time illuminated at 442 nm increase significantly from 0.9732 ms to 11.193 ms. Because of low diffusion coefficient of electrons D_{e^-} due to the collision with solids, $\tau_{diff,}$ of electrons play an important role on response time. At high power density levels of illmuniation, more electron-hole pairs generated at the deeper depth, electrons have to diffuse longer length to be collected by the electrode, so it has much longer response time, as shown in **Figure S**8 (a). At low power density levels, the carriers most generated at the surface of ZnO, the electrons excited at the edge can be collected by the electrode directly. Differently, the holes would not have collision with solids, they are empty spaces, thus the rise time is smaller at low power density.

The large quantity of photo-induced electrons causes the expansion of the depletion layer of the n side (upward bending of the band), and the holes cause the shrink of the depletion layer of the n side (down bending of the band).[62] Reversely, when the

light is cut off, the amount of free holes reduces to turn back into the original state, thus results in the expansion of the depletion layer and increase of the hole drift distance, therefore the rise time increases.

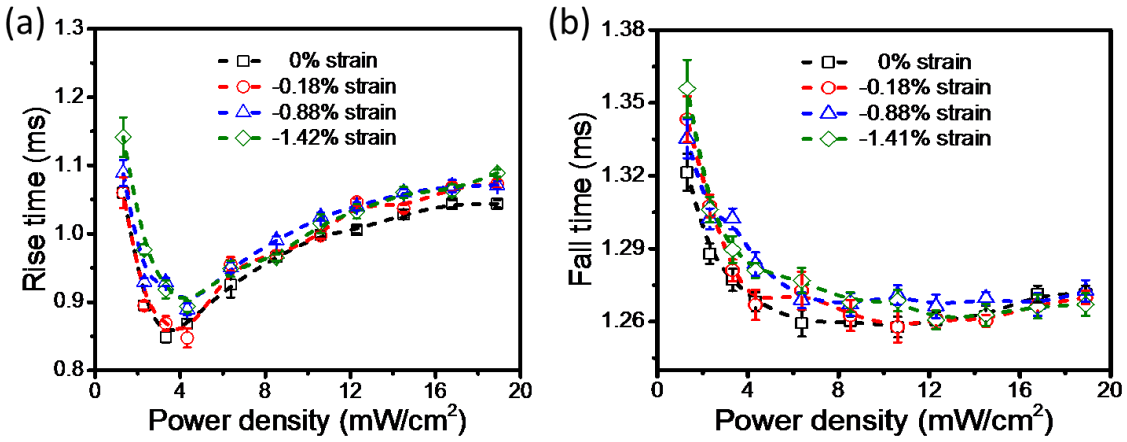

Figure 22 The corresponding (a) rise and (b) fall time of the device under different illumination power density of 1060 nm wavelength light, under different strains.

As the power density of 1060 nm light increases from 1.32 to 18.9 mW/cm^2 (Figure 22, the rise time decreases first and then increases when the power density is above about 4 mW/cm^2. The photo-induced electrons cause the expansion of the depletion of n side (upward bending of the band) while the heat absorption shrinks this depletion region reversely,[62] especially heat effect will dominate as the light intensity increase. The two above-described processes will compete with the increase of irradiation power.

Different from the situation of 442 nm light, when the 1060 nm light is cut off, the amount of free electrons reduces to turn back into the original state, thus results in the shrink of the depletion layer instead of expansion, and decrease of the electron drift distance in the n-ZnO region, therefore the fall time decreases.

3.2 Broadband Photodetector Based on p-Si/AlOx/n-ZnO Nanowire Arrays

Silicon photonics is an evolving technology that has revolutionized a great many application areas, including the communication system, computing, biomedical diagnostics, imaging, and sensing.[64-66] Silicon does, however, have a number of shortcomings as a photonic material.[67] The indirect energy band and highly reflective surface limit the absorption of light,[68] especially the near-infrared light above 900 nm.[64, 69] When the incident optical power increases, the devices will have a saturation limit[70] and the responsivities fall significantly due to the optical losses and recombinations.[71-73] In current photodiodes, doping at high temperature to create a p-n junction is popular but this would induce crystal damage and increase Auger recombination[74], thus limiting the further improvement of light response. To reduce the front surface reflectance of the planar surface, conventional antireflection coatings with different thicknesses and refractive indices is an effective method.[75-77] This would result in improvement in the certain wavelength range, however, it may reduce response at other wavelengths and increase the cost.[74, 75, 78] Developing nanostructures in the devices can improve the light response by providing longer optical paths, wider acceptance angles, and low surface reflection, but its high surface area significantly increases recombination at the device surface.[74] The hybrid integration of Ⅲ-Ⅴ materials onto Si to improve the NIR light absorption is still not cost-effective.[64, 79] Overall, to offer the lowest possible power consumption while significantly improve the performance of silicon photonics in terms of high responsivity without saturation limit is critical but challenging.

3.2.1 Enhanced Photon Sensing Based on p-insulator-n

Previously, we have presented a high-performance p-Si/n-ZnO broadband photodetector with high sensitivity.[80] Here, we report a 3-D structure photodiode concept that combines specially designed texture top electrode and nanowire arrays to maximize the absorption of light, conformal ALD alumina between the p-n junction to minimize surface recombination and dual induced inversion layers to improve the charges separation and collection efficiency. The fabricated photodiodes has excellent sensitivity, fast response speed (~220 μs), and great stability working at low biasing voltage and current. The performance of light response to light from near-ultraviolet to near-infrared has been dramatically enhanced via the formed dual inversion layers and Fowler-Nordheim tunneling. Its sensitivity and responsibility soar as the power intensity increases, and saturation limit has been overcome. It meets the stringent requirements of optical-fiber communication system, nanorobotics, analytical fields, biomedical sensing, and defense technology. To carefully investigate how the insulator layer influences the transport of electrons and holes differently, we selectively chose either electrons or holes passing through the interface of junctions by utilizing different wavelength lights, and applied the piezo-phototronic effect to modulate the charge density at the interface and alter the energy bands and potential barrier distance of tunneling. This study would help to develop a better understanding of the p-insulator-n system and enable to have notable performance improvements in optoelectronics.

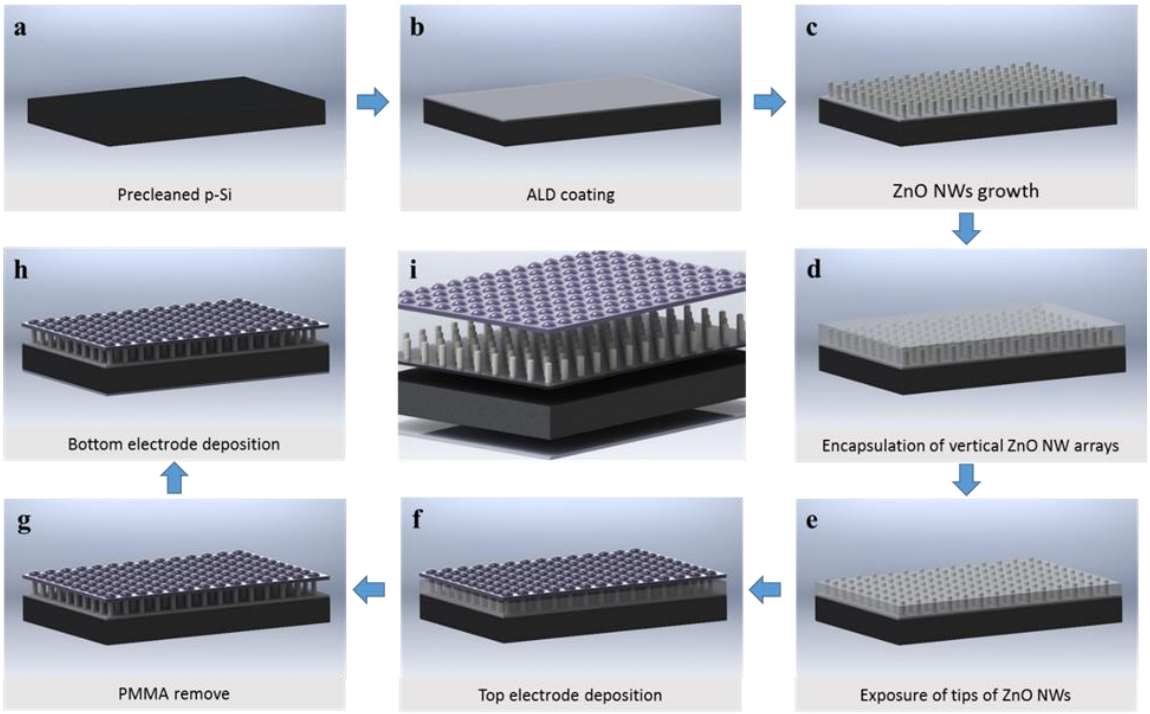

Figure 23 Processing scheme for fabricating the 3-D structure broadband photodetector based on p-Si/ AlO_x/ n-ZnO NW arrays. (a) Clean the p-type silicon wafer with acetone, and Isopropyl alcohol. (b) Deposit AlO_x via atomic layer deposition. (c) Deposit a thin layer of ZnO on the sample via RF sputter as the seed layer. ZnO is then grown in the growth solution by hydrothermal growth and annealed then. (d) PMMA resist layer is spin coated and cured. (e) The tips of ZnO nanowires are exposed by oxygen plasma treatment via reactive ion etching. (f) Schematic structure of a 3-D structure p-Si/AlOx/n-ZnO NW arrays photodetector. Deposit ITO by RF sputter as the top electrode. (g) Remove PMMA by acetone. (h) Deposit Al by electron beam evaporation. (i) Schematic structure of a 3-D structure p-Si/AlOx/n-ZnO NW arrays photodetector.

Figure 24a illustrates the structure of the broadband photodiode based on p-Si/AlO_x/n-ZnO nanowire arrays. The surface of the p-Si was covered with a 15-nm thick atomic layer deposited (ALD) alumina. The uniform 2 μm-thick ZnO nanowire arrays are grown vertically (Figure 24g) on the layer of AlO_x with a diameter of 70-80 nm.[81, 82] A mushroom like NIR antireflection layer of ITO top electrode was only developed at the tips of the nanowires. The back side of the wafer was deposited with aluminum as the bottom electrode. The top view of the scanning electron microscope (SEM) image is shown

in Figure 24b, the tips of the ZnO nanowires are core-shelled with the ITO film, the continuous ITO film is firmly supported by the nanowires and well contacted with ZnO.

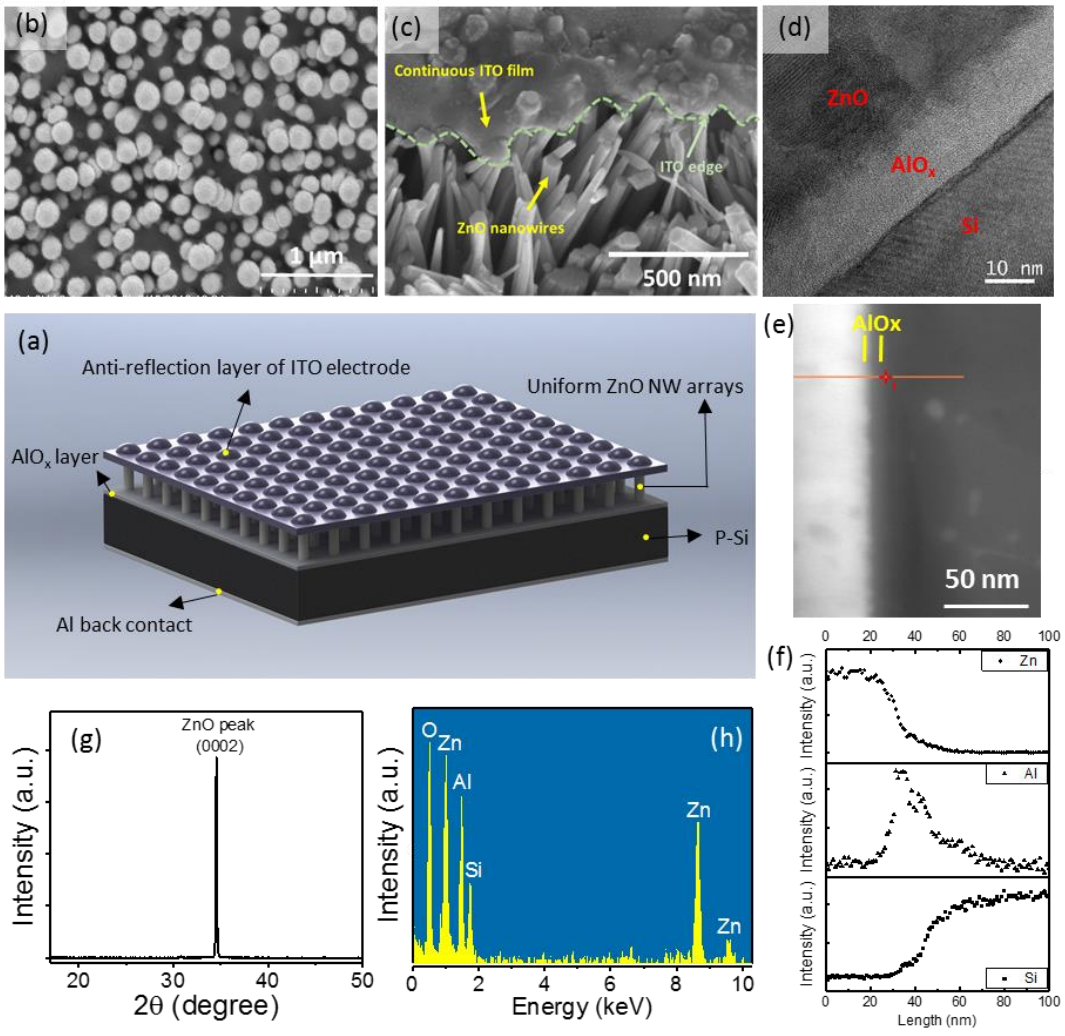

Figure 24 Device fabrication and structural characterization. a, Schematic structure of a 3-D structure p-Si/AlOx/n-ZnO NW arrays photodetector. A thin film of insulator AlOx is deposited on p-Si substrate. The nanowire arrays were grown vertically on the insulator layer. The ITO layer was core-shelled with the tips of ZnO nanowires, suspended as the ceiling. b-c, SEM images of top surface view of the device, 30° side view of top surface of ITO coating at the edge of the device, respectively. The ceiling top electrode has enoki mushroom-like texture nanostructure. d, TEM images of the cross-section. The red line in (e) is the scanning route of spectrum profile. f, Spectrum profile of the cross-section. g, X-ray diffraction of ZnO nanowires on Si. h, Energy dispersive X-ray Spectroscopy spectrum of the device.

Figure 24c shows the SEM image of 30° tilt view of the device at the edge. The ITO electrode has a texture structure with mushroom-like top surface and a flat bottom surface. The suspended top ceiling electrode could avoid current leakage and short circuit of nanowire arrays.

The transmission electron microscopy (TEM) image (Figure 24d) shows the cross-section of the p-insulator-n layers, and it shows the AlO_x layer is about 14.5 nm. The energy dispersive X-ray spectroscopy spectrum profile image and data (Figure 24e, f) show the distribution of elements, and the full width at half maximum (FWHM) of the Al peak can also demonstrate the thickness of AlO_x. The element analysis from the EDS result across the junctions is shown in Figure 24h.

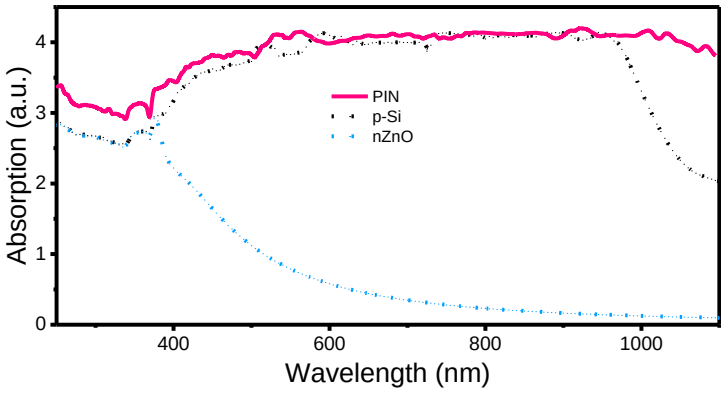

Figure 25 Absorption spectra of p-Si, n-ZnO, and the p-Si/AlOx/n-ZnO devices.

The absorption spectra of the device are shown in Figure 25. The absorption of light over 950 nm is significantly improved. The thin layer of AlO_x does not contribute to improve the absorption of light, as the transmittance of ~15 nm AlO_x is nearly 100%. The improved light absorption is believed to be a benefit of the antireflection layer of the ITO top electrode, as the textured top layer could reduce the reflection of the incident light and the flat bottom layer returns the reflected light back to be absorbed by the materials. It is

interesting to notice that at the period of negative bias, there is a hysteresis loop: the current has a higher value when the applied voltage is increasing than it is decreasing. This is also known as a memory effect, and it is different from the I-V curve from the conventional p-n junction photodiode. The broadband photodetectors exhibit great photo-sensing properties at a low bias voltage of negative 2 V. The current output curves under various illumination intensities under 442 nm and 1060 nm light are shown in Figure 26a and b, respectively.

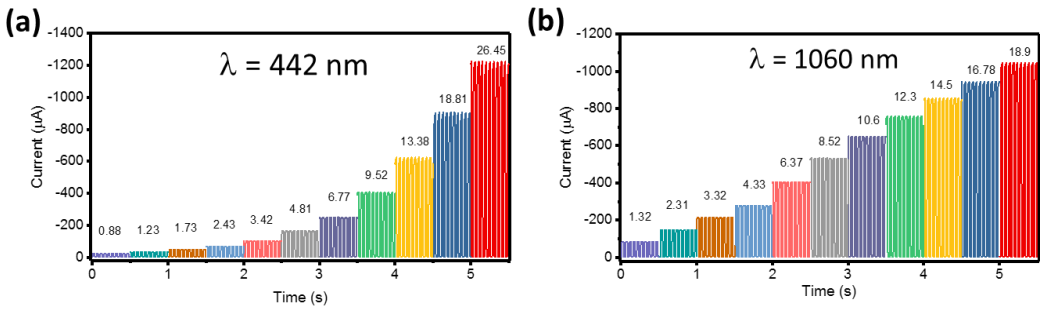

Figure 26 Output current under different power densities of (a) 442 nm light and (b) 1060 nm light.

The rise time is defined as the time interval for the response to rise from 10% to 90% of its peak value, and the fall time is defined as the time interval for the response to decay from 90% to 10% of its peak value. From Figure 27, the rise time is as fast as 260 μs, and the fall time could reach 220 μs, which demonstrates that this device is suitable to work as a high-speed photodiode that is operated at high-speed response conditions.

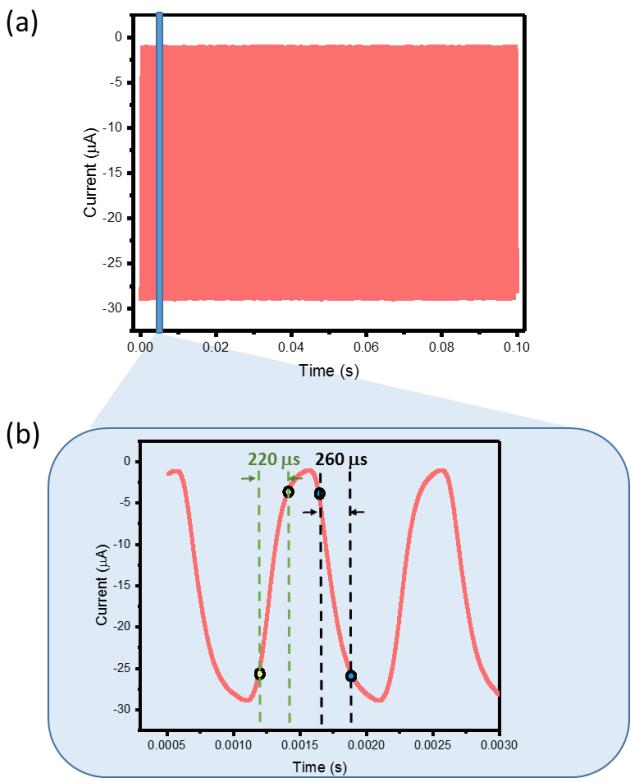

Figure 27 Response time for the photodetector. (a) The photo response over a relatively large time scale (0-0.1 s). (b) The inset of current- time figure at a small time scale.

The performance of the p-insulator-n junction device is compared with the one fabricated in the same way but without the insulator layer of AlO_x: the photocurrents ($|I| = |I_{light} - I_{dark}|$) for the device with AlO_x are above 9.5 times larger under the illumination of 442 nm near-ultraviolet light (Figure 28a) with the intensity of 26.45 mW/cm^2, and about 6.23 times larger under the 1060m near-infrared light with the intensity of 18.9 mW/cm^2 (Figure 28b). Under the near-infrared light, the device without AlO_x has a saturation limit that no additional photocurrent outputs from the photodetector as the incident optical power increases. However, the p-insulator-n device demonstrates a great linearity that the generated photocurrent increase linearly with the incident light power, overcame the limitation. The sensitivities of the device based on p-i-n junction, which is defined as

$(I_{light} - I_{dark})/I_{dark,}$ are more than 12.4 times larger than the device based on p-n junction under the 442 nm light (Figure 28c), about 8.9 times larger under the 1060 nm light (Figure 28d).

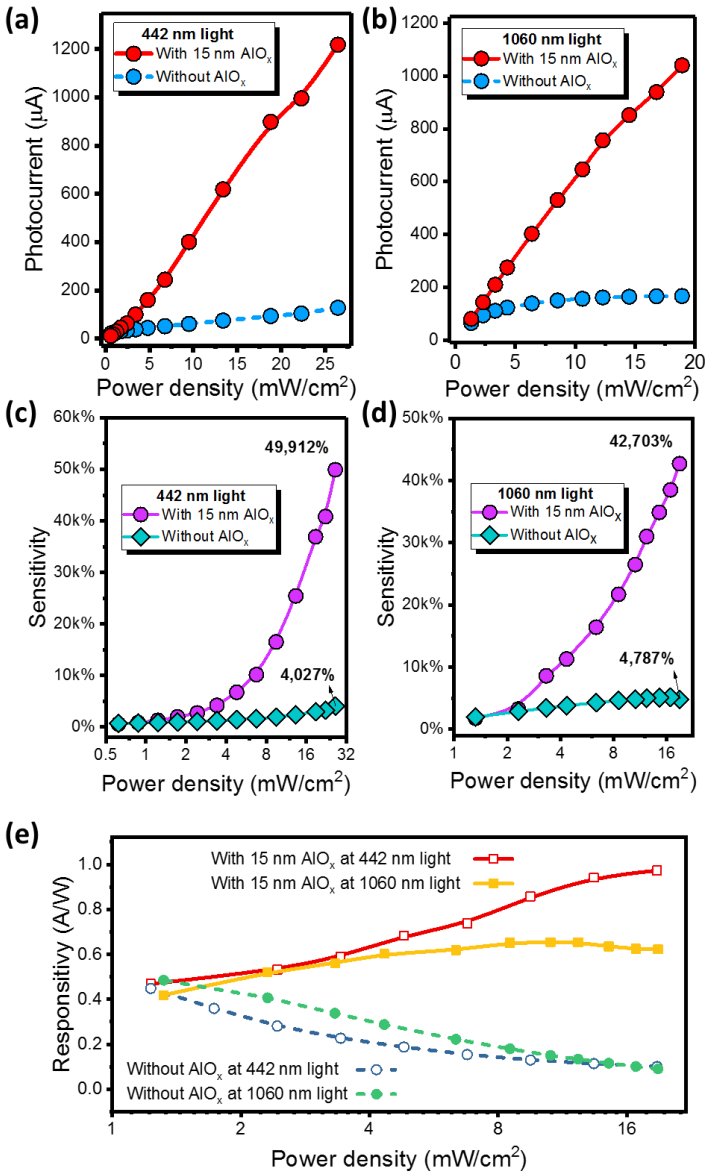

Figure 28 Optoelectronic characteristics of the PD. Photocurrent of the device under the illumination of 442 nm (a), 1,060 nm (b) with various the power densities. The sensitivity of the devices under illumination power densities of (c) 442 nm light and (d) 1,060 nm light. (e) The responsivities of the devices under illumination power densities of 442 nm light, and 1,060 nm light.

The responsivity of the photodetector, R, is defined as

$$\mathrm{R} = \frac{I_{light,s} - I_{dark,s}}{P_{ill}} = \frac{\eta_{ext}}{h\nu}\Gamma_G \qquad (15)$$

where $P_{ill} = I_{ill} \times S$ is the illumination power on the photodiode; $I_{light,s}$ and $I_{dark,s}$ represent the photon and dark current under the corresponding external strain, respectively; Γ_G is the internal gain; η_{ext} is the external quantum efficiency (EQE); q is the electronic charge; h is Planck's constant; ν is the frequency of the light; I_{ill} is the excitation power density; S is the effective area of the photodiode.

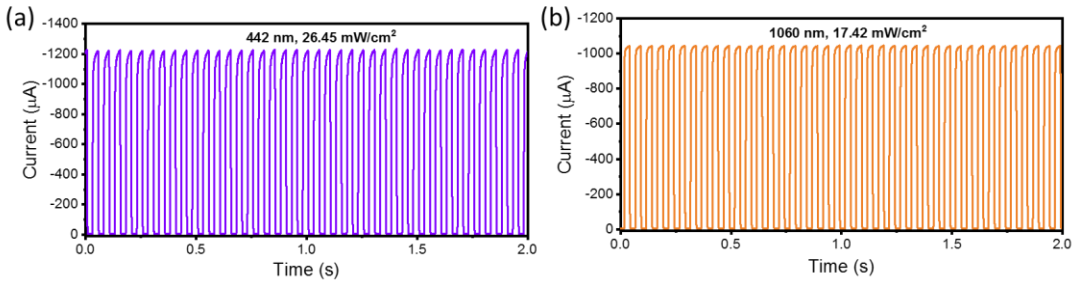

Figure 29 Repeatability and time response of the device under the (a) 442 nm, and (b) 1,060 nm light.

The photoresponsivity R is calculated as shown in Figure 28e under various light intensity. As normal, the responsivity of the photodetector without AlO_x reduces with increasing light intensity. However, it is interesting to find that the responsivity of the photodetector with ~15 nm AlO_x was increasing with light intensity, contrary to the previous reports. This phenomenon might be attributed to that, as the light goes stronger, more oppositely charged carriers would appear in the inversion layer at the semiconductor-oxide interface, thus a stronger inversion layer would be expected and the depletion expands,[8] resulting in higher current-collection capability.[83]

The stability and repeatability of light responses under the 442 nm light with the intensity of 28.46 mW/cm^2 and 1060 nm light with the intensity of 17.42 mW/cm^2 are shown in the current-time curves in Figure 29a and b, respectively. The broadband photodetector has excellent stability and repeatability, and there is no observable deviation. Consequently, this broadband photodetector based on the p-si/i-AlO_x/n-ZnO heterojunction exhibits significant improvement in its photo sensing properties, not only visible light but also near-infrared light. It operates at low power consumption, and has high sensitivity, high responsivity, fast response time, great linearity without saturation limit, and excellent stability.

3.2.2 Fowler-Nordheim Tunneling Distance

To study the key role of the middle ALD alumina layer on carriers transport in the broadband detecting, capacitance-voltage characteristics measurements (Figure 30a and b) were measured to verify the existence of inversion layers in the sample. The p-insulator-n junction can be treated as a combination of two basic junctions: p-Si/AlO_x, and AlO_x/ZnO NW arrays, two devices based on these two separate junctions were fabricated. Figure 30a and b show C-V measurements carried out on the two devices in the dark, ranging from -2 V to 2 V at 1 MHz. For the device based on p-Si/AlO_x, when the voltage sweeps from positive to negative, the net charge in the interface states changes from the accumulation, depletion, to the inversion condition. When a relatively large positive voltage (above 0.5 V) is applied to the p-Si/AlO_x device, the valence-band edge is closer to the Fermi level at the oxide-semiconductor interface than in the bulk material, which implies that there is an accumulation of holes. While the voltage decreases and swept to negative, the conduction and valence band energies bend downward, the negative space charge region induced, and

the majority carriers are depleted. The flat-band V_{FB} condition occurs between the accumulation and depletion conditions. When a sufficiently large negative voltage applied, the bands bend even more downward so that the intrinsic Fermi level E_F has moved below the Fermi level, thus the conduction band is closer to the Fermi level than the valence band (as shown in Figure 30c left side of the insulator layer). This result implies that the semiconductor surface adjacent to the oxide-semiconductor interface is n-type. An inversion layer of electrons has been induced at the oxide-semiconductor interface. Here, experimentally, it is found that the measuring frequency is high for the silicon substrate, but it is relatively low for ZnO NWs from the shape of the C-V curves. When the voltage swept from negative to positive, the states changes form the strong inversion, moderate inversion, depletion, and accumulation. This is related to the carrier lifetime and the thermal generation rate in the silicon substrate and ZnO nanowires.[84] By an applied negative voltage, the positive space charge region is induced; within this region, the conduction and valence band energies bend upward, and the intrinsic Fermi level has moved above the Fermi level so that the valence band is closer to the Fermi level than the conduction band is. This result implies that the semiconductor surface adjacent to the oxide-semiconductor interface inverts from n-type to p-type. An inversion layer of holes has been induced at the oxide-semiconductor interface (as shown in Figure 30c right side of the insulator layer). From the results, when a sufficient negative voltage is applied to the two sides of the p-insulator-n heterojunction, two inversion layers would be induced at the oxide-semiconductor interface. Figure 30c shows the energy-band diagram of the system demonstrating the formation of the dual inversion layers. P-Si/AlO_x/n-ZnO NWs hetero-junction displays more efficient charge carrier separation, a higher collection

efficiency and less surface recombination which benefits from the formation of strong inversion layers. P-insulator-n cells are made to use the stronger drift field to sweep the carriers out to P and N regions. With passivation of AlO_x, the dangling bonds defects could be efficiently reduced.

Ideally, the conductance of AlO_x is considered to be zero. However, real insulators with thin thickness show some degree of carrier conduction when the electric field is sufficiently high. Quantum mechanical tunneling describes the transition of carriers through a classically forbidden energy state. It is a result of quantum mechanics by which the electron wave function can penetrate through a potential barrier. Even if the energy barrier is higher than the electron energy, there is quantum mechanically a finite probability of this transition. The current flowing through an insulator is either Fowler-Nordheim or direct tunnel current.[85] Direct tunneling works through ultra-thin oxide, however, the 15 nm thick of AlO_x might be not possible for electrons to directly tunnel through. The Fowler-Nordheim regime is significant for thicker dielectrics and sufficiently high electric fields. Under the applied voltage, the energy bands bend down, leading to constant downscaling of gate-dielectric thicknesses in devices, where carriers tunnel through "thinned oxide", only a partial width of the barrier, thus the effect of tunneling has drastically gained relevance. As shown in Figure 30c, the carriers tunnel from the inversion layer to the energy bands at the other side.

To better understand the effect of the insulator layer on the transport of electrons and holes separately, here, the piezo-phototronic effect was employed to modify the charge density at the interface of oxide and semiconductor by applying strains to induce the piezo-charges. In this way, we are able to shift the energy bands and even alter potential barrier

width for tunneling in the same device without the need to change the materials. The piezo-phototronic effect is a three-way coupling among piezoelectricity, photoexitation, and semiconductor, which is to use the piezopotential to tune/control the optoelectronic processes at an interface/junction.[11, 43]

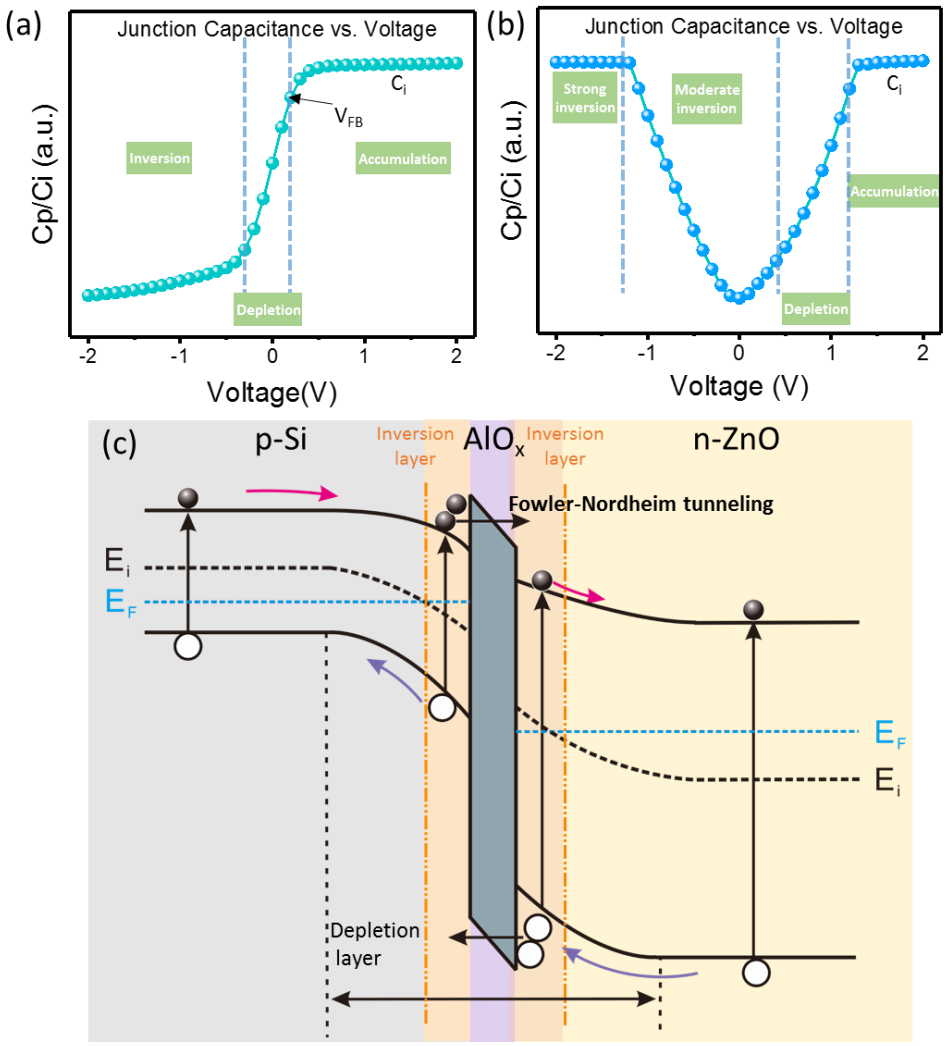

Figure 30 Principle of p-Si/AlO_x/n-ZnO broadband photodetector. a, C-V characteristics of the p-Si / AlO_x. The p-Si side for the device based on p-si/AlO_x, is connected with the positive electrode. VBF corresponds to the flat-band condition. Ci refers to the capacitance of the capacitor for this accumulation mode. C_p refers the capacitance of the capacitor at the present status. b, C-V characteristics of the AlO_x / n-ZnO NW arrays. The n-ZnO side for the device based on AlO_x / n-ZnO is connected with the negative electrode. c, Energy-band diagram in p-insulator-n for

the dual inversion layers mode under an appropriate large negative bias. The carrier charges flow through the insulating layer by quantum mechanical Fowler-Nordheim tunneling. Two inversion layers are formed at two sides of the insulating layer. The conduction and valence band edges bend as shown in the figure, indicating a space charge region similar to that in a pn junction. The conduction band and intrinsic Fermi levels move closer to the Fermi level. The intrinsic Fermi level Ei at the surface is now below the Fermi level EF; thus, the surface of the semiconductor adjacent to the oxide-semiconductor interface has inverted from a p-type to an n-type semiconductor. Similarly, we have created an inversion layer at the interface of oxide/n-ZnO nanowire arrays.

In a non-centrosymmetric wurzite semiconducting crystal, the piezoelectric charges would be induced at the interface of ZnO nanowire and insulator due to dipole moments caused by strains. In the depletion region, the induced positive charges by compression will be mostly preserved without being screened by local residual free carriers in the majority carrier-free zone. This will shift energy bands of ZnO as well as the insulator's energy bands, and potential barrier width of tunneling would be adjusted consequently. We could selectively choose the photo-generated charge carriers (either electrons or holes) passing through the depletion region, by using different wavelength lights. Under the illumination of 442 nm light, most light is absorbed by ZnO NWs, the light only excites electron-hole pairs in ZnO NW arrays. Electrons directly collected by the electrode, and only holes go across the interface. Similarly, under the illumination of 1060 nm light, electron-hole pairs are only generated in silicon, and only electrons pass through the insulator layer. This enables the possibility to investigate how the electrons and holes response to the bands shift separately with the existence of insulator layer between the p-n junction, how the inversion layers and tunneling influence on the output current when the barrier width of tunneling are altered.

Figure 33a shows that when the external compressive strains are applied, the photocurrents under various intensities of 442 nm lights increase first, then decrease. While

under various intensities of 1060 nm light, photocurrents show different changing trends, they fall down and then increase at higher strains (Figure 33b).

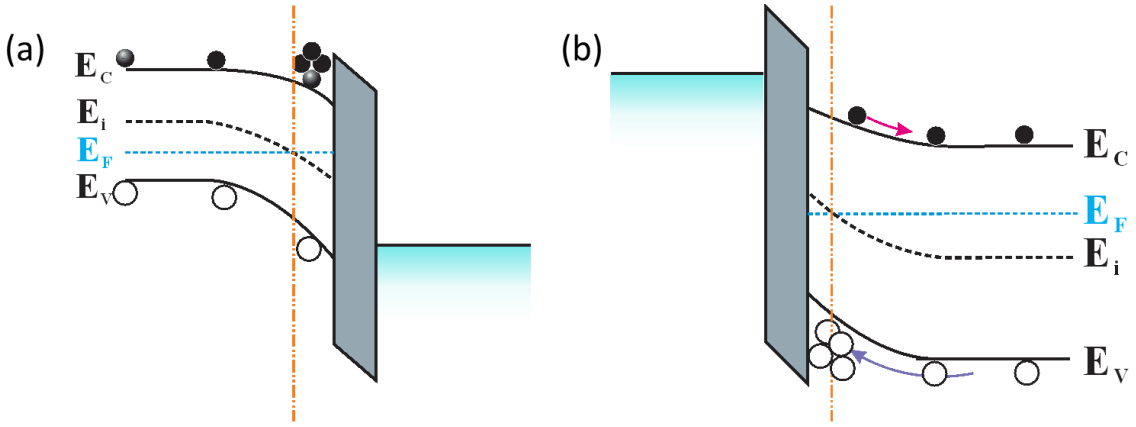

Figure 31 Schematic energy band diagram of Folwer-Nordehim tunneling in insulator-semiconductor structure for p-Si / AlOx (a), and AlOx / n-ZnO NW arrays (b). (a) When a sufficiently large negative gate voltage was applied, the bands near the interface bent downward so that the intrinsic Fermi level Ei would lie below the Fermi level EF. The conduction band would get closer to EF than the valence band to EF. At this point, the semiconductor surface adjacent to the oxide-semiconductor interface was n-type, and an inversion layer of electrons was induced at the oxide-semiconductor interface. (b) By an applied negative voltage, the positive space charge region is induced; within this region, the conduction and valence band energies bend upward, and the intrinsic Fermi level has moved above the EF so that the valence band is closer to the Fermi level than the conduction band to EF. This result implies that the semiconductor surface adjacent to the oxide-semiconductor interface inverts from n-type to p-type. An inversion layer of holes has been induced at the oxide-semiconductor interface.

The different trends of the photocurrent demonstrate that the transfer of electrons and holes behave differently. Since the ZnO NW arrays grow vertically on the surface of silicon, the compress strains would induce the positive charges at the interface of AlO_x /n-ZnO NWs (Figure 33c).

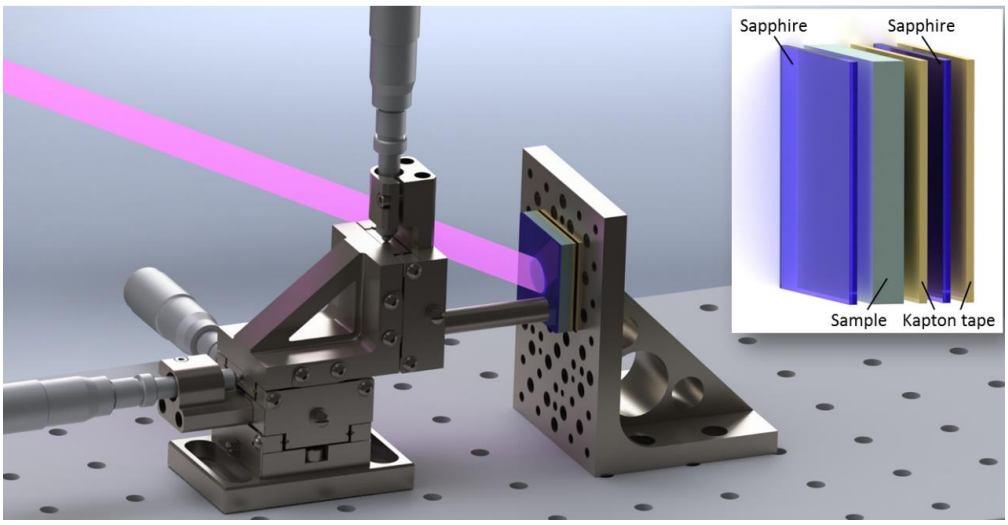

Figure 32 Experiment set-up and measurement system for applying strains on devices. The blue block refers to sapphire. The green strands for the sample. Two Kapton tapes were used to fix the sample and sapphire.

At 442 nm light, the positive piezo-charges enhance the charge density in the inversion layer region at the interface, the inversion layer that positioned at the n-ZnO NWs side builds up a stronger inversion layer and expands the depletion, so the charges separation and collection become more efficient. As the strains further increase, the piezo-potential tends to lower the local band slightly, as well as the bands of AlO_x. The further downscaling of the AlO_x would reduce the tunneling distance (Figure 33c) and the charge density accumulated at the interface. The dielectric layer would not create strong inversion layer then and this would prohibit the charge separation and collection efficiency. At 1060 nm light, the inversion layer was located at the p-Si side. When the compress strains work on the nanowires, the bands of AlO_x layer bend down due to the strain induced positive piezo-charges at the interface. The potential tunnel distance is reduced due to the alteration of the bands (Figure 33d), the charge density accumulated at the interface was lower, and the inversion layer becomes weaker then so that the photocurrent was decreased. As the strains further increase to a large value, the thinned tunneling distance would be small

enough for the carrier for tunneling through the insulator layer easily, and it would not be able to accumulate charges to have strong inversion layer. The decreased photocurrent would result in a weaker screening effect, and the tuning of the piezo-phototronic effect would turn out to be more significant, which leads to the increase of the photocurrent.[39, 86, 87] Above all, by utilizing the piezoelectric property of ZnO NWs, it produced piezo charges to modulate the energy bands, this would help us understand the effect of the insulator layer of AlO_x on the transport of electrons and holes, leading us to better understand the physics of the device system, to serve us for better performance devices.

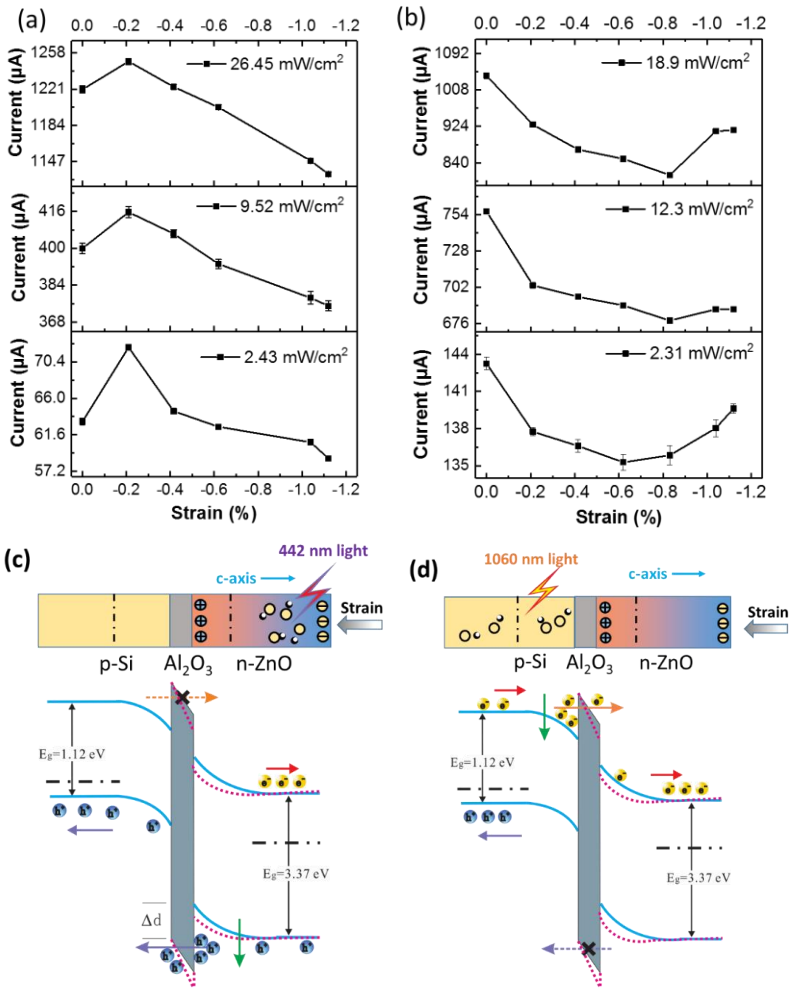

Figure 33 Study of the effect of AlO_x on electron and hole transport by using piezo-phototronic effect. Current output under different strains at -2 V bias voltage under

442 nm (a) and 1,060 nm (b) light with different power densities. Band diagram of the broadband photodiode under compressive strains at 442 nm light (c) and 1,060 nm light (d). For the color gradient, pink represent positive piezo-charges region and blue represents negative piezo-charges. The blue lines are the energy bands at the initial stage without strain, the short dot lines are the energy bands when the external strains applied.

In conclusion, we have fabricated an ultra-high performance broadband photodetector with enhanced absorption and carrier collection based on p-Si /AlO_x /n-ZnO NW arrays working over a wide wavelength range from 442 nm to 1060 nm. The uniquely designed ITO top electrode remarkably improved the absorption of near-infrared light above 900 nm, which overcame the limit of Si materials. By introducing ~15 nm AlO_x between the conventional p-n junction, the performance of light detection has been dramatically enhanced. Different from normal photodiodes, the responsivity increases sharply as the intensity of light increases, which overcome the trouble of saturation limit for other devices. Dual inversion layers were formed at the two sides of the insulator layer under the operating conditions. In the inversion layer region, surface recombination is deeply suppressed and high collection efficiency is achieved. Additionally, the fabrication process is compatible with the existing semiconductor processing techniques at low temperature via a dopant-free method. Given the obtained results, the fabricated devices presented in this work potentially renders a practical and effective approach to convert light efficiently, and pave a new path for broadband photodetectors and other optoelectronics to achieve better performance.

3.3 Photodetector Based on Ternary CdS_xSe_{1-x} Nanowires

Investigations on the coupling among mechanical, optical and electrical properties of semiconductor materials have explored an interdisciplinary field of piezo-phototronics,

which has attracted more and more research interest in the past several years.[11, 12, 88, 89] By introduced external strain along the c-axis direction of the wurtzite semiconductor, the induced piezoelectric polarization charges can effectively tune/modulate optoelectronic process, such as generation, separation, transport, and/or recombination. Previously it has been demonstrated that the sensitivity/response of photodetector (PDs), the efficiency of solar cell (SCs) and the performance of light emitting diodes (LEDs) can be enhanced greatly by piezo-phototronic effect.[24, 54, 90-92] Many attempts have been made to optimize the carrier transport process by tuning the Schottky barrier height (SBH), and thus promote the performance of PDs.[40, 93, 94] The piezo-phototronic effect has been demonstrated to take this responsibility to work on devices constructed with traditional piezoelectric material.[39, 80, 95] For example, ZnO and GaN have been studied extensively in piezotronic and piezo-phototronic devices, since a strong piezopotenial can be created in the crystal by externally applying a strain due to the polarization of ions.[96-99] Also, 1D CdS and CdSe nanostructures are the common materials for studying piezo-phototronic devices.[100-103] Up to now, most of these works about piezo-phototronic effects are limited on binary semiconductor nanostructures. Exploration of new piezoelectric materials, and the study of theirs doping/composition or structure on the modulating effect of device performance are equally important for the development of piezo-photoelectronics field.

One-dimensional (1D) wide-band ternary semiconductor are a great class of materials with potential application in nano/microdevices,[104-107] because of their continuously tunable physical properties with composition. Among them, the ternary CdS_xSe_{1-x} nanowires/nanobelts have attracted more research interest since its bandgap can be tuned by means of the composition between ~2.42 eV (for CdS) and ~1.72 eV (for

CdSe), almost covering the entire visible spectral range.[108-115] Liu's group has studied the strain-modulation behavior of ternary MgZnO film PD by introducing the piezo-phototronic effect.[116] In the case, ZnO thin film is alloyed with Mg to investigate how the alloying process and Mg content work on the piezoelectric coefficient and thus how the corresponding piezo-phototronic effect affects the performance improvement of PDs. However, as the effective polarized system to produce the piezoelectric charges, 1D nanostructure based on the ternary semiconductor nanowires have not been reported so far.

In this work, the piezo-phototronic effect on PD of ternary CdS_xSe_{1-x} nanowires (NWs) is demonstrated for the first time. The piezo-phototronic effect enhanced photoresponsivity of the single NW photodetector have been studied for different NWs of compositions $CdS_{0.85}Se_{0.15}$, $CdS_{0.60}Se_{0.40}$, and $CdS_{0.38}Se_{0.62}$. The devices show excellent photodetection ability to visible light with fast respond time, high photosensitivity and photoresponsivity. Significantly, the photoresponse of this kind of devices can be modulated under different strains and by the atomic composition of the ternary wurtzite semiconducting materials. The change in piezoelectric coefficient and carries screening effect are proposed for explaining the observed phenomenon. Also, the energy band diagrams were presented to illustrate the piezo-phototronic process on the Schottky contacted metal-semiconductor. This work offers an innovative candidate and provide a new perspective to study the NW-based piezo-phototronic PDs, which are all very important to in-depth understand the physical mechanism of piezo-phototronics effects and enable the development of high-performance piezo-phototronic devices.

3.3.1 Sensitivity and Responsivity

Ternary CdS_xSe_{1-x} NWs with site-controlled compositions were fabricated via a simple one-step CVD process in the presence of Sn catalyst. **Error! Reference source not found.**a shows a low-magnification SEM image of the CdS_xSe_{1-x} NWs, showing the diameters of about 500 nm and lengths of about several hundred micrometers. The inset is an enlarged SEM image of a CdS_xSe_{1-x} NW, with a Sn-particle locating at the tip, which indicates a typical vapor-liquid-solid (VLS) growth mechanism of the NW terminating at a catalyst metal particle. It should be noted that Sn ball at the tip of the NWs worked as catalyst can be found on most of the longer NWs, especially for the NWs with length close to millimeter. However, in many cases, such as NWs with lengths less than about 300 microns, the catalyst particles will fall off the NWs due to the thermodynamics of the growth process. TEM image and the high-resolution electron microscope (HRTEM) image of the corresponding area of a typical CdS_xSe_{1-x} are given in Figure 34b2. Combining with the corresponding select area electron diffraction (SAED) pattern in Figure 34b3, it revealed that the as-synthesized CdS_xSe_{1-x} NW is single crystal and grown along c-axis. Figure 34c shows the normalized XRD patterns of three representative CdS_xSe_{1-x} NWs obtained at different growth temperatures. The composition x of the nanowire can be determined from Vegard's law using the lattice parameters deduced from the XRD data.[106, 117] After careful observation, the diffraction peaks can be indexed to the typical wurtzite structure of ternary $CdS_{0.85}Se_{0.15}$, $CdS_{0.60}Se_{0.40}$ and $CdS_{0.38}Se_{0.62}$, respectively. Figure 34d shows the normalized PL spectra of the ternary CdS_xSe_{1-x} NWs obtained at room temperature. The spectra of all the samples show a single emission band, located at ~550 nm (2.258 eV), ~609 nm (2.036 eV) and ~656 nm (1.891 eV), respectively, which can be attributed to the near-band-edge emissions of ternary CdS_xSe_{1-x}.[106] The single emission

band with absence of defect-related band confirms the highly crystallized quality of the ternary alloy NWs.

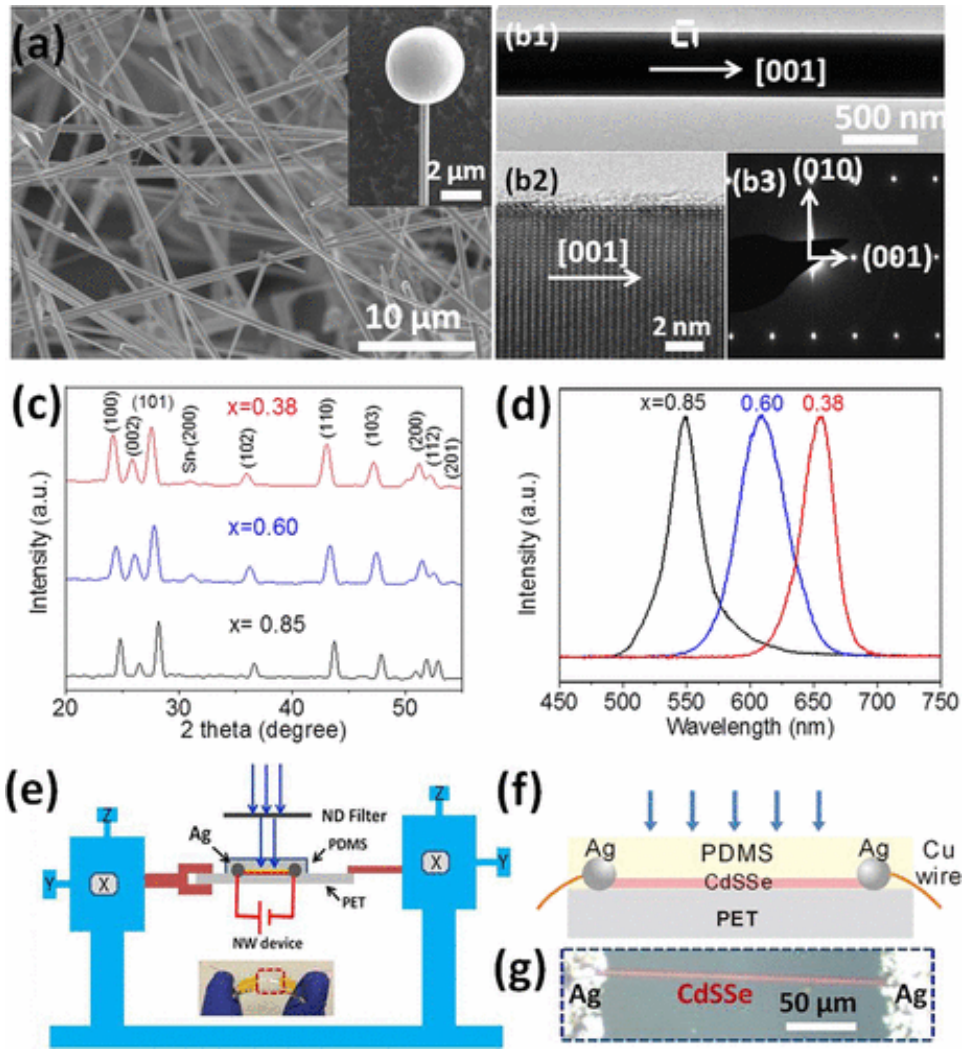

Figure 34 (a) SEM image of CdS_xSe_{1-x} NWs, the inset is a high magnification SEM image of a typical CdS_xSe_{1-x} NW with a catalyst Sn-particle on the tip. (b1) TEM image and (b2) HRTEM image of a typical CdS_xSe_{1-x} NW, (b3) is the corresponding SAED pattern, indicating that the CdS_xSe_{1-x} NW is single crystal and grown along c-axis.(c) Normalized XRD patterns of three representative CdS_xSe_{1-x} NWs obtained at different growth temperatures. (x=0. 85, 0.60 and 0.38).(d) The normalized PL spectra of the obtained CdS_xSe_{1-x} nanobelts excited with an Ar-ion laser (488 nm).(e) Schematic of the measurement setup for studying the piezo-phototronic effect in CdS_xSe_{1-x} NW. The inset is a digital image of the as-fabricated device on flexible PET. (f) Schematic diagram and (g) a typical optical image of the PD device.

Three PD devices with similar channel area (200 μm × 500 nm) based on the single ternary CdS_xSe_{1-x} NW with different composition (device #1: x=0.85, $CdS_{0.85}Se_{0.15}$; device #2: x=0.60 $CdS_{0.60}Se_{0.40}$, and device #3: x=0.38, $CdS_{0.38}Se_{0.62}$) were fabricated by a standard procedure, which has been described in the experimental section. In order to avoid the uncertainty of the introduction of metal Sn catalyst on the device interface electronic properties, the NW with no catalyst particles at the tip is selected to fabricate the device. The schematic of the measurements setup and the digital image of the as-fabricated NW device are illustrated in Figure 34e and the corresponding inset. The schematic diagram and the typical optical image of the PD device under strain-free are also shown in Figure 34f and g, respectively, which can be more clear to illustrate the structure of the devices.

Figure 35(a-c) show the typical I-V characteristic of device #(1-3) in dark and under the illumination of 442 nm light at different light intensities from 0.2 mW/cm^2 to 280 mW/cm^2 (without strain). It can be observed that all these three single CdS_xSe_{1-x} NW devices exhibit a prominent sensitivity to visible light and the photocurrents increase obviously with the excitation light intensity increasing. Significantly, under the same excitation intensity, the absolute photocurrent increase as the x value decrease at a bias of 2.0 V. For example, the maximum photocurrent under 280 mW/cm^2 of illumination increase from 260 nA (x=0.85) to 1528 nA (x=0.60) and further to 2460 nA (x=0.38). We believe it can be attributed to the tunable bandgap of the ternary CdS_xSe_{1-x} structure. The bandgap of ternary CdS_xSe_{1-x} become narrower with the decrease of the S/Se ratio in alloyed CdS_xSe_{1-x}, as shown in Figure 41a.Then, SBH between the semiconductor CdS_xSe_{1-x} and metal electrode is reduced as x decreasing, which induced more photogenerated carriers drifting the interface and thus produce a larger photocurrent.

The insets in Figure 35(a-c) show the corresponding time-resolved photocurrent response curves of device #(1-3), respectively. With the periodical changing of light irradiation on and off, the current of all three devices increase very sharply from one state to another state, exhibiting a good stability and reproducibility. Figure 35d shows a typical response time of the ternary NW PD with rise time of 1.5 ms and fall time of 2.0 ms (the response time and the fall time were defined as the time for the photocurrent to rise to 90% and decay to 10% of the maximum peak value), which are much faster than the reported results for the binary NW PD.[118, 119]

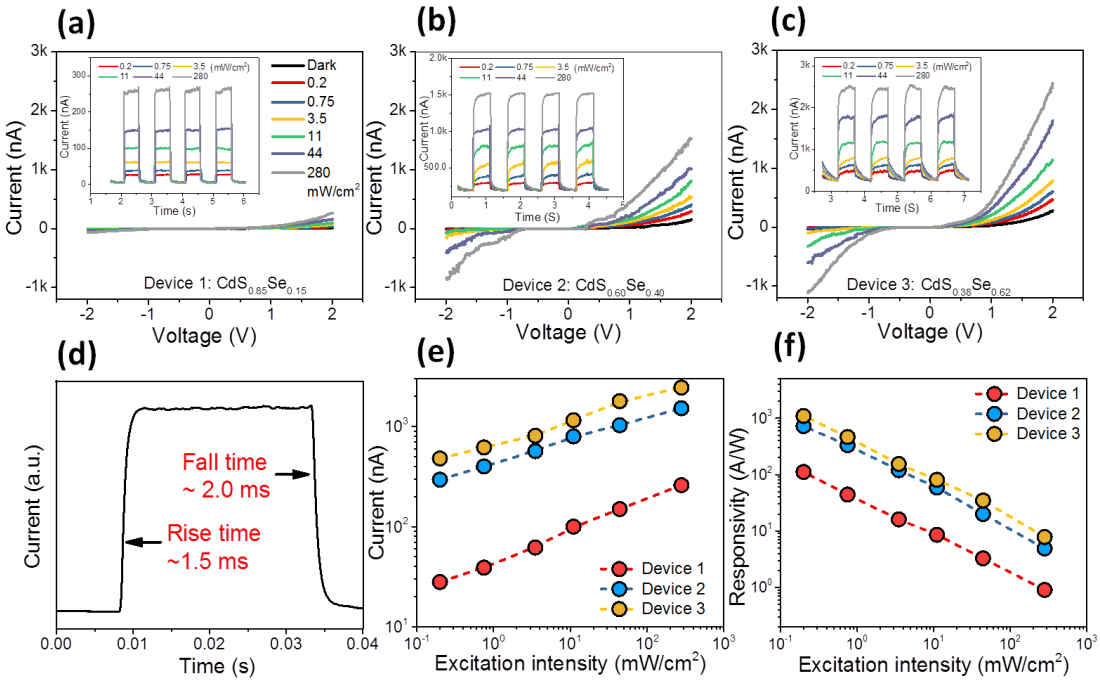

Figure 35 (a-c) The typical I-V characteristics of the single CdSxSe1-x NW PD as a function of excitation light intensity. Curves (a)-(c) for x=0. 85, 0.60 and 0.38, respectively. The inset in (a-c) is the photocurrent of the NW PD without strain under different illumination intensity with the periodical changing of light irradiation on and off. (d) The typical response time of a single CdSxSe1-x NW PD. (e) Absolute photocurrent and (f) derived photo-responsivity relative to excitation intensity on the three NW devices at bias = 2.0 V. Excitation wavelength = 442 nm.

The intensity dependences of photocurrents are plotted in Figure 35e, which exhibits a good linear relationship in the double logarithmic chart. The photocurrent of all the three devices increased with the excitation intensity and showed no saturation at high power intensity, providing a large dynamic range from about 10^{-1} to 10^{3} mW/cm^2. The fast response time and good stability indicate that the as-fabricated ternary CdS_xSe_{1-x} NWs is a great candidate for applications in visible light detection.

It is well known that the photoresponsivity (R), related to the generated photocurrent per unit power of incident light on the effective area of the PD, and the photosensitivity (S) are the important parameters to evaluate the performance of a PD. R and S defined as:

$$R = \frac{I_{light} - I_{dark}}{P_i \times L \times D} = \frac{\eta_{ext} q}{h\nu} \Gamma_G \qquad (16)$$

$$S = \frac{I_{light} - I_{dark}}{I_{dark}} \times 100\% \qquad (17)$$

where, I_{light} is the photocurrent, I_{dark} is dark current, P_i is the illumination power intensity, D is the diameter of the CdS_xSe_{1-x} wire, and L is the spacing between two electrodes, η_{ext} is the external quantum efficiency (EQE), q is the element charge, h is Planck's constant, ν is the frequency of the illuminated light, Γ_G is the internal photoconductive gain. The excitation intensity dependences of photoresponsivity are calculated and plotted in Figure 35f, which also show a good linear relationship in the double logarithmic chart. At the same excitation intensity, device #3 exhibits the best R value due to the highest photocurrent, as shown in Figure 35e, and the maximum R is approximately 1.1×10^{3} A/W at an intensity of 0.2 mW/cm^2 of 442 nm light illumination, which is much higher than that of the

networks CdSe NWs PD.[120] The photoresponsivity of all the three devices decrease with increasing the excitation intensity, which could be attributed to the hole-trapping saturation and the Schottky barrier being transparent at high light intensity, as has been observed from a ZnO NW-based UV light PD.[39] However, the photosensitivity of the three devices, as shown in Figure 36 (a-c), display a linear increasing with improving the excitation intensity. The maximum value of about 4462% in device #1 obtained at the light intensity of 280 W/cm^2, which is much higher than previously reported photoconductive PD based on single CdS nanobelt.[121]

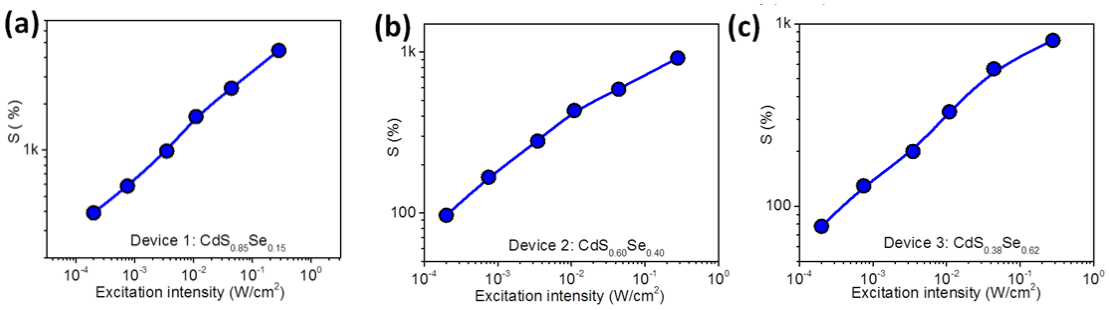

Figure 36 (a-c) Photo-sensitivity relative to excitation intensity of the single NW PD device #(1-3). Excitation wavelength = 442 nm, bias=2.0 V.

In addition to excellent response to blue light, the ternary CdS_xSe_{1-x} NWs also exhibits a good response to green light. Figure 37a shows the real-time photo switching behavior of the $CdS_{0.85}Se_{0.15}$ NW device performed under 532 nm with a power intensity of 2.48 mW/cm^2 at a bias of 2.0 V. However, when the same excitation light was imposed on an individual CdS NW device (the CdS NW was fabricated in the same growth process as CdS_xSe_{1-x} NW, but obtained at a lower deposition temperature), it has no observable photon response to 532 nm light, as shown in Figure 37b. Obviously, the ternary CdS_xSe_{1-x} NW exhibits a broader range of light detection, comparing with CdS NW. Furthermore, the response range can extend to the entire visible spectrum, even the near infrared, as the

ratio of Se/S increasing.[122] It is attributed to the flexible bandgap tuning from CdS (x=1 with bandgap of 2.42 eV) to CdSe (x= 0 with bandgap of 1.72 eV) of ternary CdS_xSe_{1-x}, which indicated a prospective candidate for applications in optoelectronics.

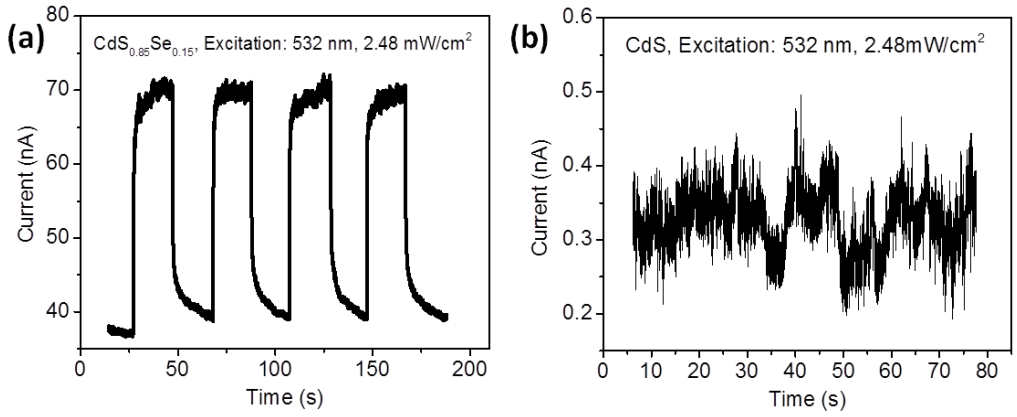

Figure 37 Repeatable response of (a) $CdS_{0.85}Se_{0.15}$ NW and (b) CdS NW. Excitation wavelength = 532 nm, Bias=2.0 V.

To investigate the effects of piezopotential on the performance of the ternary CdS_xSe_{1-x} NWs, the strain, coupling with light excitation, were imposed upon the single NW device to study the piezo-phototronic effect. Figure 38(a-c) show the typical I-V characteristics of device #1 ($CdS_{0.85}Se_{0.15}$) under illumination of 442 nm light, and the corresponding insets are plots of photocurrents as a function of strain upon different excitation light intensity at a bias voltage of 2.0 V. The asymmetric I-V curves show the rectification behavior under all strain conditions, which indicate the forming of the back-to-back Schottky barriers at the interfaces of the semiconductor NW and metal Ag electrodes. Obviously, in the positive voltage range, the photocurrent decrease upon the compressive strain and increase as the tensile strains increasing from 0% to 0.4%. Figure 35a shows I-V curves measured in the weak light excitation intensity at about 0.2 mW/cm^2. From the inset in Figure 38a, the photocurrent at 2.0 V bias increases from 26.94 nA to

45.3 nA under tension strains up to 0.4%, and down to 20.97 nA under compressive strains up to -0.4%. A similar tendency was also observed under the illumination of medium excitation intensity (3.5 mW/cm^2) and intense excitation intensity (44 mW/cm^2), as exhibited in Figure 38b and c. However, the change of photocurrent induced by strain at negative bias side have no definite trend because of the accompanied piezoresistance effects. [9]

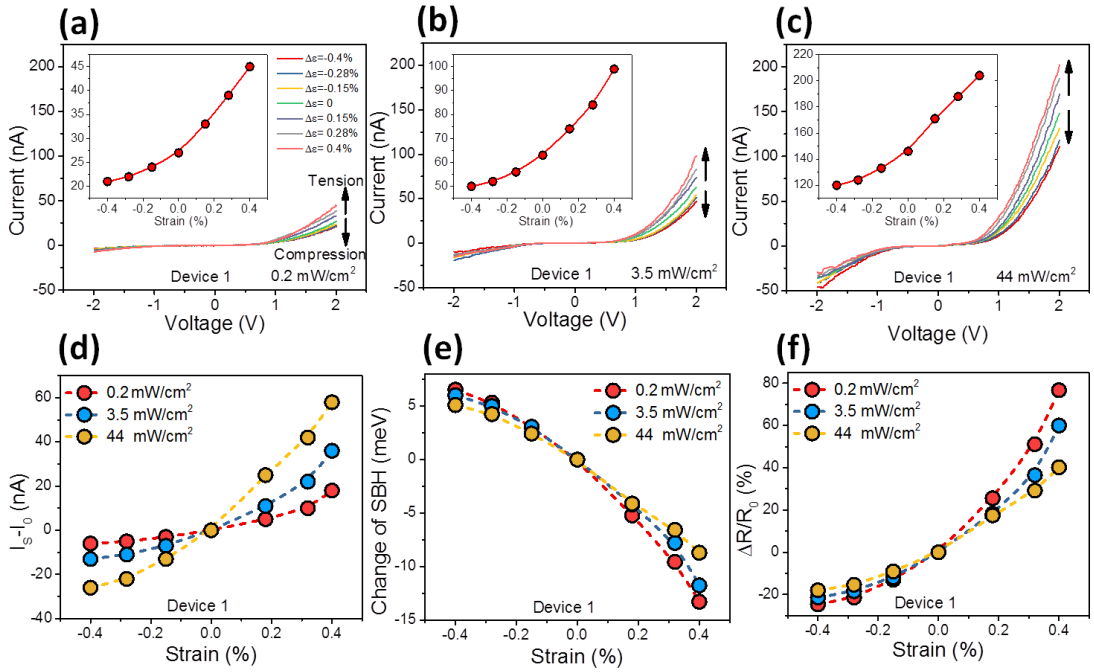

Figure 38 (a-c) The typical I-V characteristics of device #1 (CdS0.85Se0.15) under different tensile and compressive strains, with excitation light intensity of (a) 0.2 mW/cm2, (b) 3.5 mW/cm2 and (c) 44 mW/cm2, the inset in (a-c) is the corresponding absolute photocurrent at bias=2.0 V. (d) Changes of photocurrent derived from (a-c), I0 is set as photocurrent under zero strain for this illumination power. (e) The derived change in SBH as a function of strain using the thermionic emission diffusion model. (f) Changes of responsivity derived from (a-c); R0 is set as responsivity under zero strain. Excitation wavelength = 442 nm.

Figure 38d shows the photocurrent changes of the PD with and without strain (I_S-I_0) under different excitation intensity, which were extracted from Figure 38(a-c). It can be seen clearly that compressive strain leads to a monotonic decreasing photocurrent and

tensile strain induces a monotonic increasing photocurrent in the un-degraded strains range. In addition, a larger photocurrent changes are observed in intense excitation intensity with the same variation of strain. This is because the more photogenerated carries are exposed to the variation of the strain in a higher excitation intensity, and thus inducing more obvious photocurrent changes.

It has been reported that the SBH at the interface of a metal and semiconductor is an important factor in determining the transport property of the metal-semiconductor-metal structure.[40] To understand the changes of the photocurrent with strains, a thermionic field emission (TFE) theory was considered to describe the current transport with illumination. The changes of SBH ($\Delta\Phi$) with strain are calculated by $\Delta\Phi = -kT\ln(I_S/I_0)$[123], where, k is Boltzmann constant, T is temperature, I_S and I_0 are measured at a fixed bias V with and without strain, respectively. The relationship of changes of SBH on strains is calculated and plotted in Figure 38e, which indicate an increase/decrease of SBH under the compressive/tensile condition. The changes of responsivity, inducing by applied strain, is a significant parameter to evaluate the degree of piezo-phototronics effect on the performance of PD. We have the changes of responsivity as $\Delta R/R_0=(R_S-R_0)/R_0$, where, R_S and R_0 are set as responsivity under applied strain and free strain, respectively. Figure 35f shows the relationship of $\Delta R/R_0$ on applied strain in different excitation intensity. It can be seen that the $\Delta R/R_0$ increases with tensile strain and decreases with compressive stain, but the degree of variation is asymmetric, which is a typical feature of piezo-phototronic effect.[94] The responsivity of the PD under the 0.4% tensile strain was enhanced by 76.7%, 57.1% and 40.2% upon the excitation intensity of 0.2 mW/cm^2, 3.5 mW/cm^2 and 44m W/cm^2, respectively. The enhanced performance of the PD is attributed to the effective

decrease of the SBH between the ternary CdS_xSe_{1-x} semiconductor and the metal Ag electrode due to the energy band modification caused by polarization charges, as will be discussed later. It is pointed out that the responsivity is much larger enhanced for weak light detection than for strong light detection, which indicates a potential application in ultra-sensitive light detection, as the detection of low-intensity light is practically desired.

3.3.2 The Composition Effect of Materials on Piezo-phototronic Effect

To further investigate the piezo-phototronic effect on the ternary PD performance with different x composition, device #2 ($CdS_{0.60}Se_{0.40}$) and device #3 ($CdS_{0.38}Se_{0.62}$) are also be studied by applied tensile strain. In order to clearly show the performance improvement of the three devices under tensile strains at different illumination intensities, Figure 39 presents the compared results of (a-c) photocurrent (d) responsivity (R) and (e) the relative increases of responsivity ($\Delta R/R_0$), respectively. It can be seen from the column graph in Figure 39 (a-c) that the absolute photocurrents of the three devices increase as the tensile strain increasing and improve as the excitation intensity rising. The maximum changes of photocurrent are from ~ 5.6 nA (C1: Strain free, Dark) to ~ 204 nA (C2: 0.4% tensile strain, 44 mW/cm^2) for device #1 (Figure 39a), from ~150 nA (C1) to ~ 1348 nA (C2) for device #2 (Figure 39b), and from ~270 nA (C1) to ~2265 nA (C2) for device #3 (Figure 39c), which have enhanced by 36.43, 8.99 and 8.38 times, respectively. The larger improvement in device #1 is mainly attributed to the lower dark current, which can be seen from Figure 39a. As we know, a Schottky junction will form between an n-type semiconductor materials and a metal with higher work function. A lower electronic affinity will induce a higher SBH between the mental-semiconductor (M-S) junction if the carrier concentration is close in the semiconductor with a similar high crystal quality. Then, a high

contact resistance will form and induce a low dark current. It has reported that the affinity energy of the binary CdSe is higher than that in CdS, and the energy band of ternary CdS_xSe_{1-x} change continuously between the band gap of binary CdS and CdSe.[110] So the SBH between the semiconductor CdS_xSe_{1-x} and metal Ag electrode increase as x approaches 1. Then, a higher SBH of device #1 than that of device #2 and/or #3 with decreasing x will hinder the carriers drifting the M-S interface and therefore induce a lower dark current.

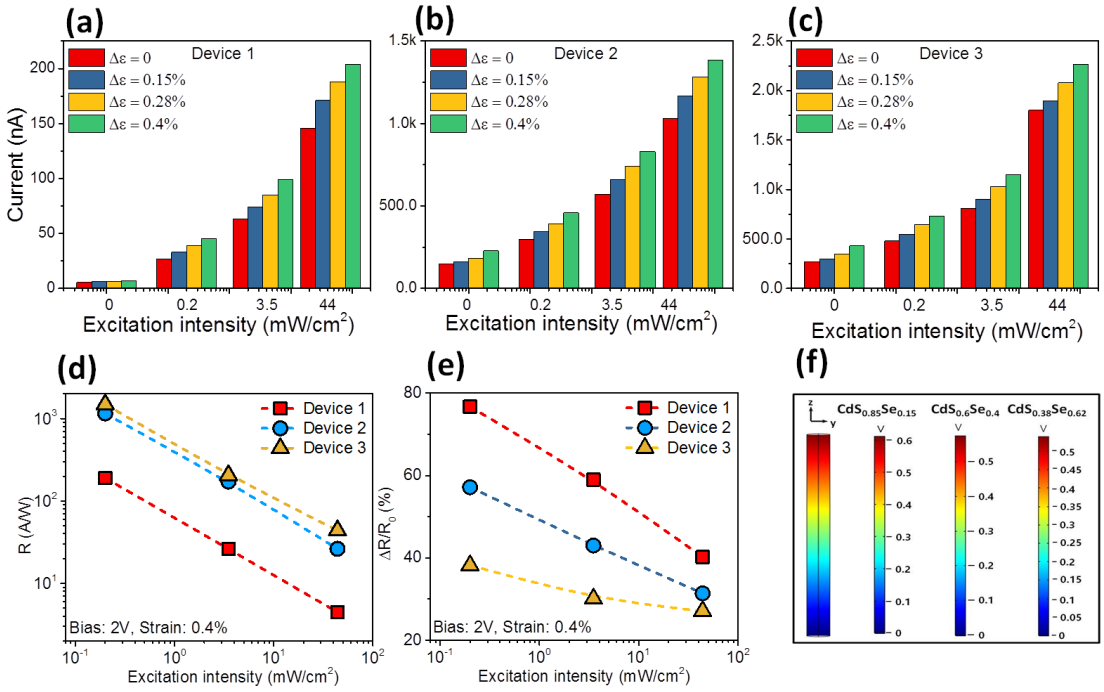

Figure 39 (a-c) Column graph of absolute photocurrent under different tensile strains and different excitation intensity at bias = 2.0 V. Graph (a)-(c) for device #1 ($CdS_{0.85}Se_{0.15}$), device #2 ($CdS_{0.60}Se_{0.40}$) and device #3 ($CdS_{0.38}Se_{0.62}$), respectively. (d, e) Dependences of responsivity (R) and relative increases of responsivity ($\Delta R/R_0$) on excitation light intensity under 0.4% tensile strain and at bias of 2.0 V, derived from (a-c); R_0 is set as responsivity under zero strain. Excitation wavelength = 442 nm. (f) Simulation of the piezopotential distribution in the wire of typical CdS_xSe_{1-x} with x=0.85, 0.6 and 0.32 under tensile strain.

Photoresponsivity (R) under strain is an important parameter in evaluating the effects of piezo-phototronics on the performance of a PD. Figure 39d shows the R values of the three devices by 0.4% tensile strain under different excitation light intensity at a bias of 2.0 V. It can be seen that the responsivity of device #3 is higher than that of device #2 and is much higher than that of device #1. The trend is similar to the compared result of the photocurrent, which indicates device #1 has a smaller photogenerated carriers than that in device #2/#3 when applied the same strain and illumination condition. Figure 39e presents the changes of responsivity of the three PDs at a fixed tensile strain of 0.4%. The maximum value of enhancement for device #1 is 76.7%, larger than that of device #2 enhanced by 59 %, and device #3 enhanced by 41.9% upon the excitation intensity of 0.2 mW/cm^2. It was reported the effect of piezopotential to the SBH can be described as $P= \varepsilon_{xx} e_{33}$ for an axial polarization, where, ε_{xx} is a constant strain along the length of the wire, e_{33} is the piezoelectric tensor.[39] In our case, the piezoelectric coefficiency of CdS is 0.440, which is larger than 0.347 that for CdSe.[124] For the ternary CdS_xSe_{1-x} with similar wurtzite crystal structure of binary CdS and CdSe, the ratios of lattice parameters c/a that reflect the asymmetry of crystals increase from CdS to CdSe as x decreasing.[106] So the potential drops resulting from the changes of piezoelectric coefficients will increase from CdSe to CdS. By the finite element method, we calculated piezopotential distribution in the wire of typical CdS_xSe_{1-x} with x=0.38, 0.6, and 0.85, as shown in Figure 39f. It can be seen a positive potential drop will be induced along the length of the wire under tensile strain and the potential drops will increase from $CdS_{0.38}Se_{0.62}$ (~ 0.53 V) to $CdS_{0.6}Se_{0.4}$ (~ 0.57 V), and further to $CdS_{0.85}Se_{0.15}$ (~ 0.62 V). For quantitative comparisons, the calculated results of piezopotential drops for binary CdSe (~ 0.47 V) and CdS (~ 0.72 V) were demonstrated

in Figure 40. Therefore the SBH is decreased with x increasing at the fixed tensile strain. Thus, a more obviously piezopotential drop will produce in device #1, and induce a more pronounced enhancement of photoresponsivity in ternary CdS_xSe_{1-x} with a larger x. In addition, the screening effect induced by the photogenerated carries is another possible reason for the performance of the PDs.[39] An increased carrier density speeds up the possibility of screening effect on the polarization charges, which weakens function of the piezo-phototronic effect on the performance of the PD. In our three devices, carrier density and photocurrent are increasing with Se/S value of the ternary CdS_xSe_{1-x} NW based PD upon the same excitation light and applied strain. Therefore, a larger enhancement of photoresponsivity in device #1 is observed.

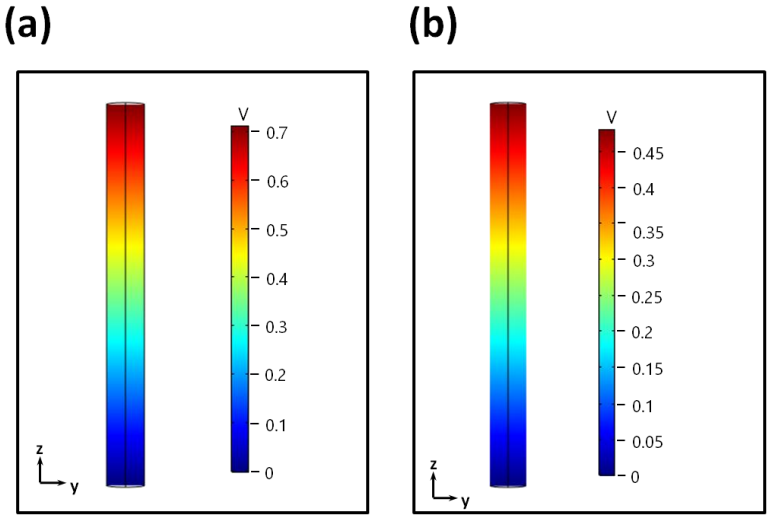

Figure 40 Simulation of the piezopotential distribution in the wire under tensile strain (a) for CdS, (b) for CdSe. The diameter and length used for calculation is about 500 nm and 200 μ m, respectively.

As described in previous work, the internal piezoelectric field formed inside wurtzite semiconductor NW can tune the charge transport/separation process at the contact and thus optimize the photoresponse of a single semiconductor wire.[92] To further

understood the piezoelectric potential on the performance of our PDs under illumination, a theoretical model by analyzing the energy band diagram is proposed to illustrate the piezo-phototronics effect on the CdS_xSe_{1-x} NW, as shown in Figure 41. The conduction band (CB) and valence band (VB) of the n-type CdS_xSe_{1-x} locate between corresponding band-edge of CdS and CdSe.[111, 125] Two back-to-back at the contacts, with SBH at the drain side and at the source side, would be created between semiconductor CdS_xSe_{1-x} and Ag electrode. In our case, when a relatively large positive voltage was applied at drain side, the voltage drop occurred mainly at the reversely biased Schottky barrier at the source side. So the SBH at the source side is much higher than that at the drain side. When the Schottky barrier photosensitive device is under illumination of 442 nm light, as shown in Figure 41a, the incident photons give rise to electron-hole pairs in the semiconductor. Under external electric field, the electron-hole pairs are separated and induce a plenty of excess electrons and excess holes. The photogenerated electrons in the CB are inclined to move close to the interface of drain side and the holes in VB are inclined to move toward to the source side, and therefore induce the photocurrent flowing from the drain side to source. Usually, the photocurrent depends on the effective separation and transport of both holes and electrons at the vicinity of the contacts, and is strongly affected SBH as a result from the TFE theory.[126, 127]

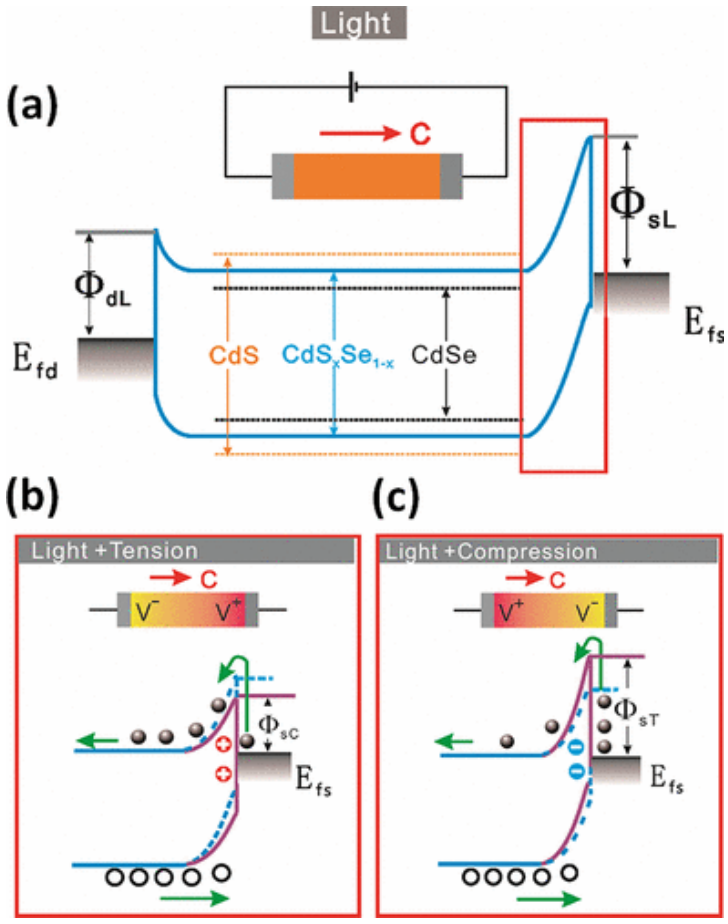

Figure 41 Schematic Energy band diagram for illustrating the piezo-phototronic effect on a Schottky contacted metal-semiconductor interface when (a) only illumination, (b) tensile strain and illumination, (c) compressive strain and illumination are applied to the single CdS_xSe_{1-x} NW device.

When tensile strain is applied along the c-axis direction of the semiconductor NW, positive polarization charges were introduced at the vicinity of source side to reduce the SBH ($\Phi_{sT} < \Phi_{sL}$). The decreasing SBH at local contact will facilitate electrons transport across the M-S interface, and induce an increasing photocurrent, as shown in Figure 41b. Furthermore, a larger tensile strain will result in a greater decrease in SBH, and induce a greater photocurrent, as observed in Figure 41a. In addition, the function of the polarization charges on the SBH is affected by the excitation intensity on the device. An increase excitation intensity will induce a larger carrier density, which will increase the screening

effect on the polarization charges, and weaken the function of strain on the photocurrent enhancing. Therefore, the piezo-phototronic effect can help enhancing responsivity of the detection at low light intensity, but does not necessarily have significant effect for strong light intensity. Conversely, if the compressive strain is applied on the device, negative polarization charges will be introduced at the interface, and increase the SBH ($\Phi_{sC} > \Phi_{sL}$), as shown in Figure 41c. In the case, the higher SBH is not favorable for the photogenerated electrons/holes transfer, therefore reduce the photocurrent, leading to a low responsivity of the detection.

As discussed above, although the photocurrent and responsivity of device #1 with lower Se content ($CdS_{0.85}Se_{0.15}$) is lower than that of device #2 ($CdS_{0.60}Se_{0.40}$) and device #3 ($CdS_{0.38}Se_{0.62}$) , with higher Se content, the enhanced responsivity is larger due to the enhancing of piezoelectric coefficiency and the decreasing screening effect of the polarization charges. According to the fundamental theory, carrier transport behavior can be controlled by piezopotential, which achieved by external strain and photo-excited process. Whereas, the present study demonstrates that the piezopotential can also be tuned by the composition of the Se/S ratio in the ternary CdS_xSe_{1-x}. The performance of the PDs can be regulated by changing the Se/S ratio to manipulate the optical-electrical process through the piezo-photronice effect, which provides a novel way to study piezo-photoelectronic effects.

In summary, we have fabricated high quality of single crystal ternary CdS_xSe_{1-x} nanowires. The application of the ternary alloyed CdS_xSe_{1-x} NW for the high-performance flexible visible photodetectors was first demonstrated. The devices exhibit an excellent photoresponse on visible light (442 nm) with high sensitivity, responsivity, and fast

respond speed. By introducing the external strain, the performance of the PDs was further improved by piezo-phototronic effect. The responsivity of the PD ($CdS_{0.85}Se_{0.15}$) is enhanced by 76.7%, 57.1%, 40.2% upon 0.2 mW/cm^2, 3.5 mW/cm^2 and 44 mW/cm^2 by introducing a 0.4% tensile strain. The piezo-phototronic effect under tensile strain reduce SBH, and facilitate the transport of photo-excited carries, inducing the increase of photocurrent and responsivity. A theoretical mode of schematic energy band diagram is proposed to illustrate the enhancing mechanism. Significantly, the composition effect of materials in ternary materials on both light detecting and piezo-phototronic were also first investigated systematically. The results present that the performance of the ternary CdS_xSe_{1-x} NW PD can be tuned by the S/Se ratio, and the piezo-phototronic effect was stronger as the ratios of S/Se increasing. The unique piezo-phototronic properties of the ternary CdS_xSe_{1-x} NW materials provides us with a versatile potential pathway to tune/control the performance of optoelectronic devices, enables the development of the better performance of optoelectronic, but also broadens the family of piezotronic materials, demonstrates a promising candidate for further piezo-phototronic devices.

CHAPTER 4. PIEZO-PHOTOTRONIC EFFECT ON LIGHT EMISSION PROCESSES

Group III-nitride-based ultraviolet (UV) light-emitting diodes (LEDs) have attracted considerable interest due to a wide range of applications such as water treatment, high-density optical data storage, sterilization of medical equipment, and biological imaging.[128] Although III-nitride LEDs have been commercialized and widely used in backlighting and general illumination, quantum efficiency enhancement and light output improvement is still necessary to further reduce the cost and expand their applications. Especially, UV LED sources suffer from relatively low quantum efficiencies that are still far behind those of the visible region. [129, 130] Ideally, increasing current injection enables the improvement of internal quantum efficiency (IQE) and light output in LEDs. Unfortunately, this straightforward route to cost-reduction is not readily available in practical GaN-based LEDs due to a phenomenon, generally called "efficiency droop" that makes IQE to decline at high injection current density.[131, 132] The efficiency droop has long been an obstacle to develop high efficiency and high power LEDs. Although the physical origin of the droop effect is still being debated, many proposals have been forwarded such as Joule heating,[119, 133] poor holes injection efficiency,[134, 135] electrons leakage,[136, 137] and so forth.

The large ionic component of the Ga–N bonds, combined with the deviation of their equilibrium lattice structure from ideal wurtzite crystals, give rise to giant spontaneous polarization fields in III-nitride semiconductors.[138, 139] The intrinsic polarizations in the nitrides play essential roles in corresponding devices. For example, high-density two-dimensional electron gas (2DEG) forming at AlGaN/GaN interfaces caused by

spontaneous and lattice-mismatch-induced piezoelectric polarizations enable the performances of nitride high-electron mobility transistors to surpass transistors made from any other semiconductor family in radio frequency power performance.[140] Moreover, current commercial GaN LEDs grown along *c*-axis are negatively impacted by the quantum confined Stark effect (QCSE) due to large polarization-related spontaneous and piezoelectric fields.[141] Therefore, several technological modifications, aiming to modify the polarization field in GaN-based LEDs, have been proposed as droop remedies, such as varying the volume of active region,[134, 142] exploring semipolar or nonpolar devices,[143, 144] engineering the energy band profile by inserting interlayers.[145] Most of these methods were realized by continuously optimizing material growth parameters/processes, which inevitably add the cost and complexity of devices fabrication and also may degrade the crystal quality caused by the introduction of dislocations. Therefore, an alternative strategy for efficiency enhancement and droop suppression is therefore highly desirable.

In the present work, the piezo-phototronic effect is utilized to simultaneously enhance quantum efficiency and suppress efficiency droop in GaN microwire (MW)-based p–n junction UV LED. By applying a −0.12% static compressive strain perpendicular to the p–n junction interface, the relative external quantum efficiency (EQE) of GaN-based UV LED is enhanced by over 600%. An obvious efficiency droop is observed in the GaN-based LEDs as increasing injection current beyond certain value under strain-free condition. When the piezo-phototronic effect is introduced by applying a −0.12% static compressive strain, the efficiency droop is significantly reduced from 46.6% to 7.5% and corresponding droop onset current density shifts from 10 to 26.7 A cm^{-2}. Performances optimization of our GaN MW-based LEDs is attributed to the enhanced electrons trapping and reduced

electrons leakage within the p–n junction region and uniform carriers injection due to energy bands tilt across the bulk region (n- and p-type region). Theoretical calculations are systematically performed to confirm the proposed working mechanisms. This study presents in-depth understandings about the piezo-phototronic effect in p–n homojunctions and offers an unconventional path for the development of high efficiency, strong brightness, and high-power III-nitride visible/UV LEDs/LDs.

4.1.1 Emitted Light Intensity

GaN MWs used in this work were synthesized by a metal–organic chemical vapor deposition (MOCVD) system as described elsewhere.[146] The synthesized GaN MWs are along the nonpolar $\langle 2\bar{1}\bar{1}0\rangle$ (i.e., *a*-axis) direction with their *c*-axis pointing across its thickness direction, which has been fully characterized in our previous work.[147] The corresponding atomic structure models (overall and cross-section view) of the GaN MW are shown in Figure 42a1. A Mg-doped p-type GaN film grown on a sapphire substrate and an indium tin oxide (ITO)-coated sapphire substrate were used to fabricate p–n junction LED with a single n-GaN MW. Figure 42a2 schematically shows the GaN-based p–n junction LED. Under external bias above turn-on voltage, light emission occurs at p–n junction interface and escapes from the distal end of the GaN MW (Figure 42b) due to the Fabry–Pérot waveguide behavior.[148, 149] A bright light spot (upper right, inset in Figure 42b) from the end of the GaN MW was observed and collected by a microscope objective. The scanning electron microscope (SEM) image of the trapezoid-shaped end surface of GaN MW (lower right, inset in Figure 42b) indicates that its polar *c*-axis points away from p-GaN film and $-c$ plane contacted with p-GaN to form p–n junction.

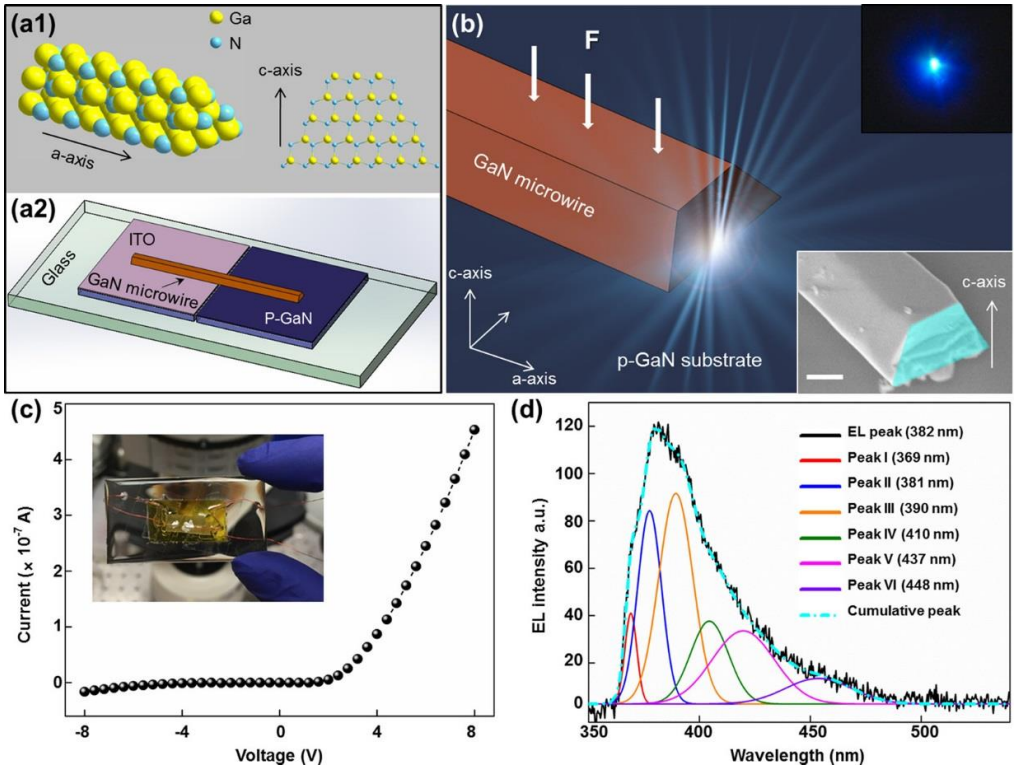

Figure 42 General characteristics of GaN MW-based LEDs. (a) Atomic structure model (overall and cross-section view) of the GaN MW (a1) and schematic image of the fabricated LED (a2). (b) Schematic image showing the light emission escaped from the distal end of the GaN MW. Upper inset: light spot of the MW-based LED observed under microscope. Lower inset: SEM image of the trapezoid-shaped end surface of GaN MW. (c) *I–V* characteristic of the as-fabricated LED. Inset: photograph of a real MW-based LED device. (d) Room-EL spectrum collected from the MW-based LED device and corresponding peak-deconvolution with Gaussian functions of the EL spectrum.

The *I–V* characteristic of the as-fabricated LED under strain-free condition (Figure 42c) exhibits a strong rectification behavior with quite low reverse leakage current. The low turn-on voltage estimated to be ~2.8 V implies high p–n junction quality of the LEDs and good Ohmic contact formed at two electrodes. A digital image of the as-fabricated p–n junction GaN MW-based LED device is shown in the inset of Figure 42c. Room-temperature electroluminescence (EL) spectra under various injection currents are shown in Figure 43b. A strong UV light emission (Figure 42d) centered at around 382 nm is obtained under 30 μA injection current and its full width at half-maximum (fwhm) is ~42

nm. Peak-deconvolution with Gaussian functions exhibits that the broad spectrum consists of six distinct bands and each emission band corresponds to a particular recombination process. Emission origin analyses are illustrated confirmed by room-temperature photoluminescence (PL) spectrum taken from n-GaN MW (Figure 43c).

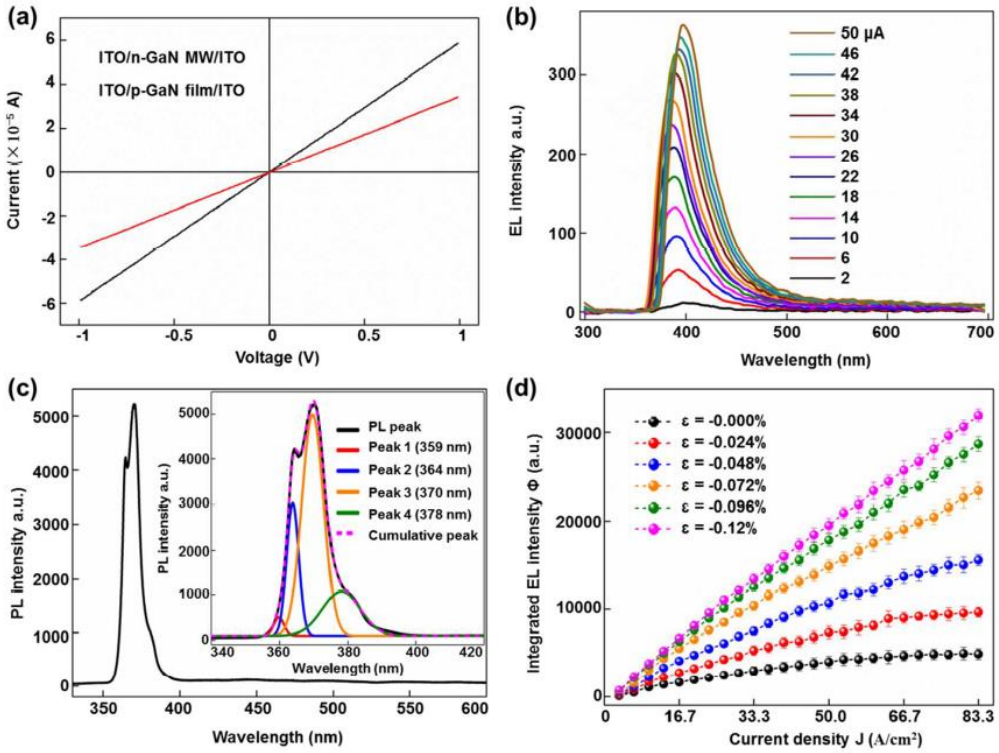

Figure 43 Electrical and optical properties of the fabricated LEDs. (a) Conformation of good Ohmic contact when n-GaN MW and p-GaN film contact with two ITO electrodes. (b) EL spectra at various injection currents collected from the fabricated micro-LED. (c) Micro-PL spectrum of a single n-GaN MW; Inset: corresponding peak peak-deconvolution with Gaussian functions of the micro-PL spectrum. (d) The calculated effective barrier height of the PN junction in the GaN MW-based LEDs under various compressive strains.

To explore the piezo-phototronic effect on the performances of the as-fabricated GaN NW-based LED devices, a homemade measurement system (Figure 44a) consisting of an inverted microscope, a piezo-nanopositioning stage, and a fiber optical spectrometer was utilized to simultaneously collect the electrical characteristics, output light spectra and

brightness of light spot of the GaN MW-based LEDs under a series of uniform external strains.

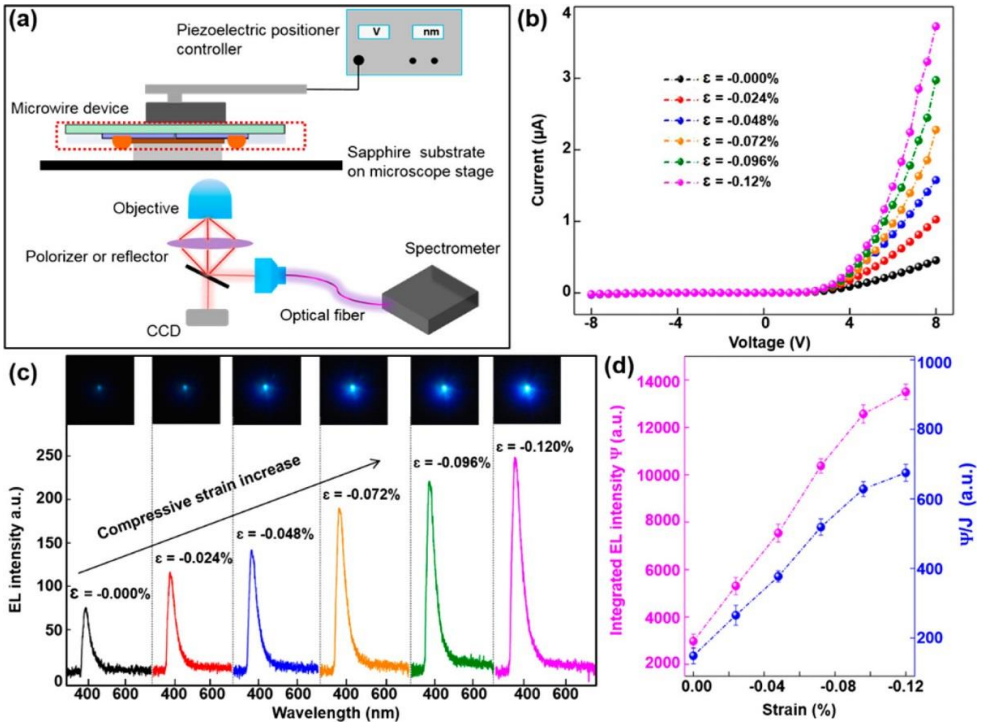

Figure 44 Enhancement of emitted light intensity by piezo-phototronic effect. (a) Schematic diagram of the homemade measurement system for characterizing the performances of MW-based LEDs under compressive strain. (b) I−V characteristic of the as-fabricated LED at forward bias with the variation of the applied compressive strain. (c) Optical spectra collected from the MW-based LED at 20 μA injection current under various compressive strains (lower panel) and corresponding CCD images recorded from the emitting end of the GaN MW under different applied strain. (d) Change of the integrated EL intensity (magenta) and relative EQE (blue) of the MW-based LED with increasing externally compressive strain.

At a fixed external bias, the output currents of the LED devices increase gradually with increasing the compressive strain from 0.00% to −0.12% (Figure 44b). Associated physical mechanisms will be discussed later. Under a fixed injection current of 20 μA, the significantly enhanced light intensity by applied compressive strain can be directly observed in optical images of the light spot recorded by a CCD (upper panel in Figure 44c) and corresponding light output spectrum under each compressive strain (lower panel

in Figure 44c). The integration area of each emitted spectra is further calculated (magenta, Figure 4.22d) to represent the relative light intensity Ψ of the LED, indicating the emitted light intensity is gradually enhanced by increasing the external compressive strain. The relative EQE (η_{ex}) of the GaN MW-based LED can be represented by ψ/J. The calculated η_{ex} (blue, Figure 44d) is enhanced by over 450% under −0.12% applied compressive strain at the fixed injection current density J of 33.3 A cm^{-2}.

4.1.2 Suppression of Efficiency Droop

Efficiency droop is another main restrictive factor for achieving high power-conversion efficiency and high-power GaN-based LEDs. Generally, the physical origin of efficiency droop phenomenon in GaN-based LEDs is attributed to thermal and/or nonthermal mechanisms.[150] In order to rule out that thermal effect is the dominant mechanism of efficiency droop here, two distinct current injection modes, continuous mode and pulsed mode (duty cycle of 20%), are utilized to drive our MW-based LEDs. Figure 45a shows EL spectra under various injection current densities from 3.3 to 83.3 A cm^{-2} under continuous and pulsed operation mode. Corresponding peak locations (Figure 45b) are extracted and indicate that the spectra peak wavelength first blue shift to shorter wavelength under low injection current for both continuous and pulsed modes. Then it exhibits an obvious redshift of about 10 nm under continuous mode as further increasing the current density whereas it remains almost constant for pulsed mode. The blue shift of the spectra peak wavelength under low injection current arises from the Fermi-level band filling effect[107, 151] and the redshift under high injection current is caused by Joule-heating.[152, 153] No obvious peak wavelength shift was observed as increasing the injection

current under pulsed current injection mode, indicating that the thermal effect in the p–n junction of GaN MW-based LEDs is largely relieved at this situation.

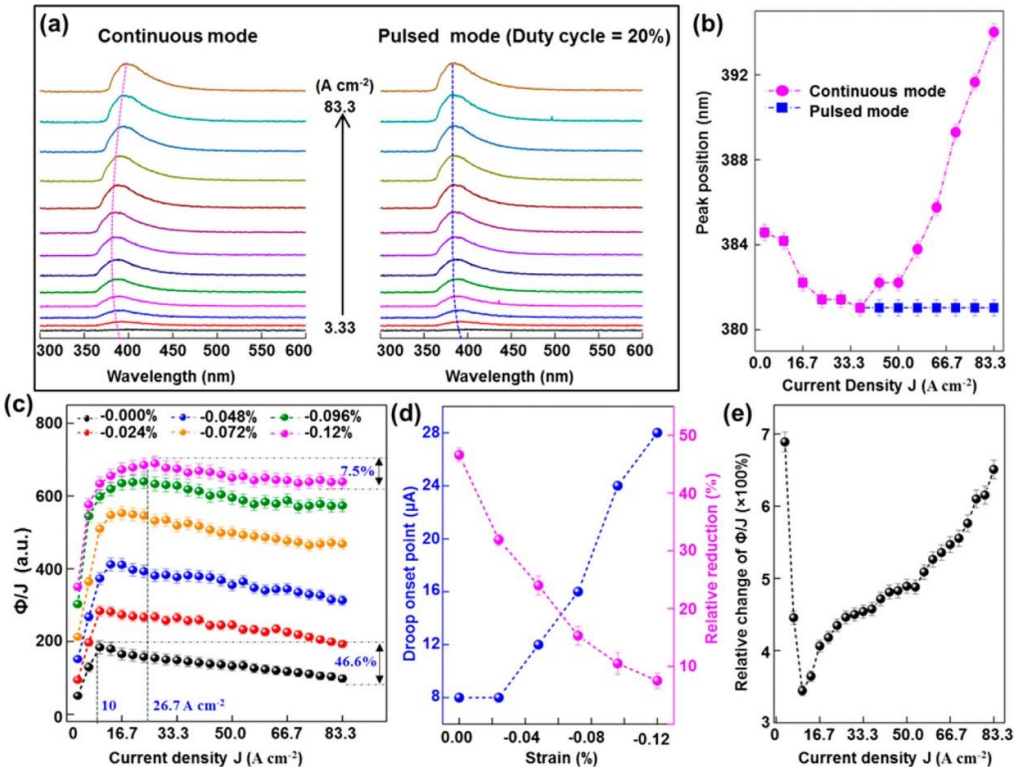

Figure 45 Suppression of efficiency droop by piezo-phototronic effect. (a) EL spectrum under various injection current density from 3.3 to 83.3 A cm^{-2} under continuous (left) and pulsed (right) current injection mode. (b) Evolution of the peak wavelength as increasing injection current density under continuous (magenta) and pulsed (blue) mode. (c) Corresponding relative EQE (η_{ex}) of the MW LED devices represented by Ψ/J at each injection current density (J) point under various compressive strains. (d) Droop onset current densities and the change of efficiency drop values as a function of the external applied strains. (e) Relative change of η_{ex} at each injection current density condition.

Efficiency droop in the GaN MW-based LEDs under various external compressive strains and a series of injection currents is then systematically studied under pulsed operation mode. Relative EL intensity (Ψ) of the MW LED devices as a function of injection current density (J) at various compressive strains (Figure 43d) indicate the light

intensity increases with increasing the injection current density/externally applied compressive strain under a fixed compressive strain/injection current density condition.

Corresponding η_{ex} of the MW LED devices derived by Ψ/J at each injection current density and each compressive strain condition are further calculated (Figure 45c). Under strain-free condition (black curve, Figure 45c), η_{ex} first increases with increasing the injection current density, and then significantly drops as continuous increase of the current density after reaching its maximum value at the current density of 10 A cm^{-2}. This high droop onset current density is impressive compared to the previously reported planar structured GaN LEDs,[154, 155] which is attributed to high light extraction efficiency due to 1D geometry of n-GaN MW and high crystal quality of our n-GaN MW and p-GaN film. Furthermore, η_{ex} significantly drops down by 46.6% when the pulsed current density increases to 83.3 A cm^{-2}, which indicates that thermal effect is not the dominant mechanism of efficiency droop in our GaN MW-based LEDs. As the externally applied compressive strain increases from −0.00% to −0.12%, the efficiency droop is markedly reduced from 46.6% to 7.5% and corresponding droop onset current density gradually shifts from 10 to 26.7 A cm^{-2} (Figure 45d). Various technological modifications[156-158] have been reported and utilized to suppress the efficiency droop in InGaN multiquantum well (MQW) LEDs by regulating internal polarization. On the basis of the experimental observations above, the piezo-phototronic effect, as an unconventional approach, can effectively relieves the droop efficiency in the p–n junction GaN MW-based LED.

Further study of the piezo-phototronic effect on the efficiency enhancement was performed by calculating the relative change of η_{ex} which is represented by $[(\Psi/J)_{strain=-0.12\%} - (\Psi/J)_{strain=0.00\%})]/(\Psi/J)_{strain=0.00\%}$ at each injection current density condition (Figure

45e). Obviously, η_{ex} is enhanced by over 600% at certain injection current density conditions under a −0.12% compressive strain. At low *J* less than 10 A cm^{-2}, the relative variation of η_{ex} decreases as increasing *J* due to the increase of *J* dominant η_{ex} in our GaN MW-based LEDs. As *J* further increasing, the relative change of η_{ex} gradually increases, indicating that η_{ex} of the LED is largely enhanced and efficiency droop is effectively suppressed under high injection current density by the piezo-phototronic effect.

4.1.3 Physical Mechanisms and Theoretical Simulation

To fully understand and analyze the piezo-phototronic effect on the performances of our GaN MW-based LED, piezo-potential distribution across the LED under compressive strains were systematically calculated. Commercial finite element analysis software COMSOL Multiphysics is utilized to conduct the theoretical simulation and calculate the strain and piezo-potential distribution of *n*-type GaN MW under different compressive strains. A three dimensional (3D) model with exact the size of practical *n*-GaN MW/*p*-GaN film LED device is built. All the materials' parameters used in the simulation are listed below in Table 2. **Table 2 Materials' parameters used in the simulation**

Material	ε_r	Density	Young's modulus	Poisson's ratio
Glass	2.09	2.203[g/cm^3]	73.1[GPa]	0.17
PMMA	3.0	1.19[g/cm^3]	3[GPa]	0.40
Kapton	3.4	1.3[g/cm^3]	3.1[GPa]	0.34
Sapphire	11.5	3.98[g/cm^3]	435[GPa]	0.29
ITO		6.8[g/cm^3]	116[GPa]	0.35
Polypropylene	2.2	0.904[g/cm^3]	1.3[GPa]	0.42
PDMS	2.75	0.97[g/cm^3]	923[psi]	0.49

Under a −0.12% static compressive strain, the overall view and cross-section view of piezo-potential distribution within the LED are simulated and presented in Figure 46a and inset of Figure 46b, respectively. Corresponding piezo-potential values across the LED device are extracted and plotted in Figure 46b. Obviously, negative piezo-charges is induced at the top surface (+*c* plane) of n-GaN MW and positive at the bottom surface of p-GaN film. The net polarization charges at the p–n junction is simulated to be positive as a result of electrostatic coupling between the induced positive piezo-charges at −*c* plane of n-GaN MW and negative piezo-charges at p-GaN surface. The built-in electric field, energy band profile within the depletion region of the p–n junction, and corresponding device performances of the LEDs are naturally and inevitably modulated by the induced piezo-charges.

The upper surface of the top sapphire substrate is fixed, which means it has no displacements in any directions at all. An upward displacement along the *c*-axis direction of *n*-type GaN MW (*i.e.* the z-axis direction in the coordinate) as a boundary condition is applied to the lower surface of the bottom glass substrate. An electric ground boundary condition is applied at infinite boundaries to serve as the reference for the calculation of the piezo-potential distribution. Finally, the piezoelectric constitutive equations are solved using the Solid Mechanics, Electrostatics and Piezoelectric Effect modules in COMSOL. After the computation, the strain and piezo-potential distribution of the *n*-type GaN MW under different compressive strains could be derived and obtained by post-processing.

Table 2 Materials' parameters used in the simulation

Material	ε_r	Density	Young's modulus	Poisson's ratio

Glass	2.09	2.203[g/cm^3]	73.1[GPa]	0.17
PMMA	3.0	1.19[g/cm^3]	3[GPa]	0.40
Kapton	3.4	1.3[g/cm^3]	3.1[GPa]	0.34
Sapphire	11.5	3.98[g/cm^3]	435[GPa]	0.29
ITO		6.8[g/cm^3]	116[GPa]	0.35
Polypropylene	2.2	0.904[g/cm^3]	1.3[GPa]	0.42
PDMS	2.75	0.97[g/cm^3]	923[psi]	0.49

Under a −0.12% static compressive strain, the overall view and cross-section view of piezo-potential distribution within the LED are simulated and presented in Figure 46a and inset of Figure 46b, respectively. Corresponding piezo-potential values across the LED device are extracted and plotted in Figure 46b. Obviously, negative piezo-charges is induced at the top surface (+*c* plane) of n-GaN MW and positive at the bottom surface of p-GaN film. The net polarization charges at the p–n junction is simulated to be positive as a result of electrostatic coupling between the induced positive piezo-charges at −*c* plane of n-GaN MW and negative piezo-charges at p-GaN surface. The built-in electric field, energy band profile within the depletion region of the p–n junction, and corresponding device performances of the LEDs are naturally and inevitably modulated by the induced piezo-charges.

The generation of piezo-potential and corresponding energy band profile of the LED devices is carefully analyzed under strain-free and compressive strain conditions to illustrate the physical mechanism of the performances optimization in our p–n junction LEDs (Figure 46c). Under strain-free condition, depletion region and built-in electric field (E_b) are generated at the p–n junction interface with the direction of E_b pointing away from n- to p-type region (upper left). The corresponding energy band diagram of the p–n junction

at forward bias (lower left) exhibits the charge carriers (electrons and holes) inject into the junction region from bulk region and recombine with each other. During this process, the electrons from n-type region go through depletion region and leak into p-GaN region with strong possibility due to their high mobility (up to ~200 cm^2 $(V \cdot S)^{-1}$[1159]), leading to severe nonradiative recombination due to the existence of a large number of nonradiative recombination centers within p-GaN. On the other hand, poor holes mobility in GaN (in the order of 10 cm^2 $(V \cdot S)^{-1}$) leads to nonuniform/asymmetric carriers injection (insufficient hole injection) in junction region. Therefore, electrons leakage and nonuniform/asymmetric carriers injection results in low power conversion efficiency and efficiency droop in the p–n junction LED, especially under high current injection condition.

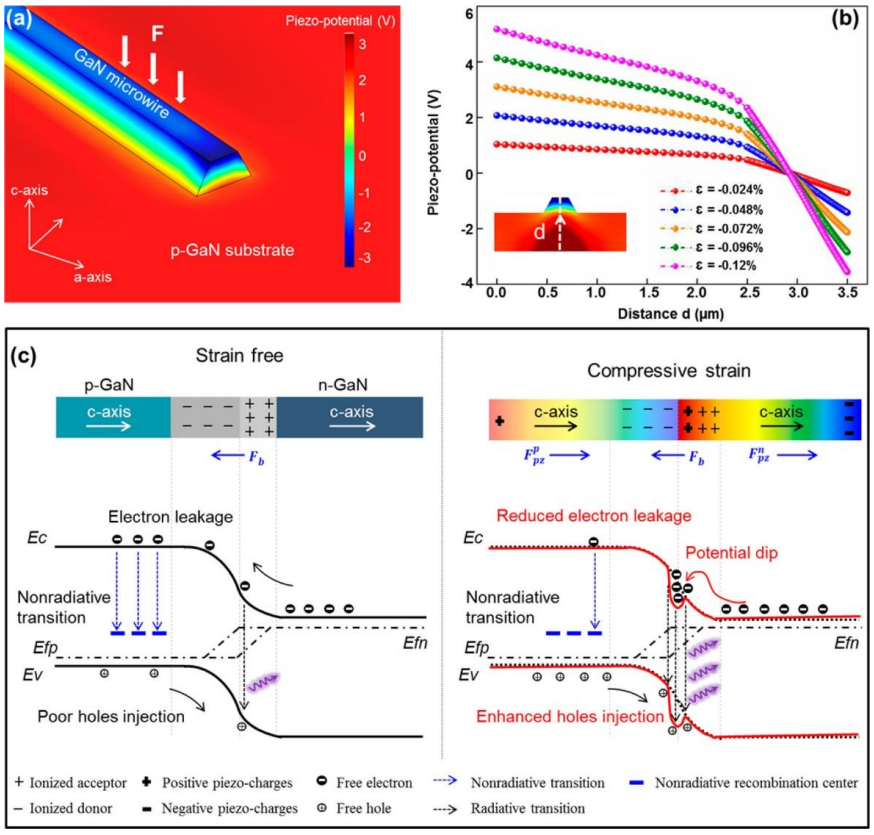

Figure 46 Theoretical simulation results and physical mechanisms. (a) Under a −0.12% compressive strain, the overall view of piezo-potential distribution. (b) Piezo-

potential values across the LED device normal to the p–n junction interface; inset: cross-section view of piezo-potential distribution within the GaN MW-based LEDs under −0.12% compressive strain. (c) Generation of piezo-potential and corresponding energy band profile of the LED devices under strain-free (left) and compressive strain (right) conditions.

Under externally applied compressive strain (upper right), two extra piezoelectric fields F_{pz}^{n} and F_{pz}^{p} with opposite direction with F_b are induced within n-GaN MW and p-GaN film, respectively. The generation of F_{pz}^{n} and F_{pz}^{p} also weakens F_b and tilts the energy band across n- and p-type region, leading to effective energy band gap (E_g) shrinking for n- and p-type region.[160] The magnitude of F_b is equal to the barrier height (Φ_b) of the p–n junction, which can be expressed by

$$\Phi_b = qV_d \tag{18}$$

where V_d is the contact potential difference of the p–n junction and

$$V_d = \frac{k_bT}{q}\left(ln\frac{N_AN_D}{n_i^2}\right) \tag{19}$$

in which N_A and N_D are concentration of acceptors and donors. n_i^2 is the product of electrons and holes concentration in nondegenerate semiconductor under equilibrium, which can be written as

$$n_i^2 = N_CN_V exp\left(-\frac{E_g}{k_bT}\right) \tag{20}$$

where N_C and N_V are the effective density of states at the bottom of conductive band and top of the valence band, respectively. According to above equations, V_d is proportional to E_g that is reduced under compressive strain, and thus V_d and Φ_b can also be effectively

reduced by externally applied compressive strains. Details about the quantitative calculations are founded in Figure 47.

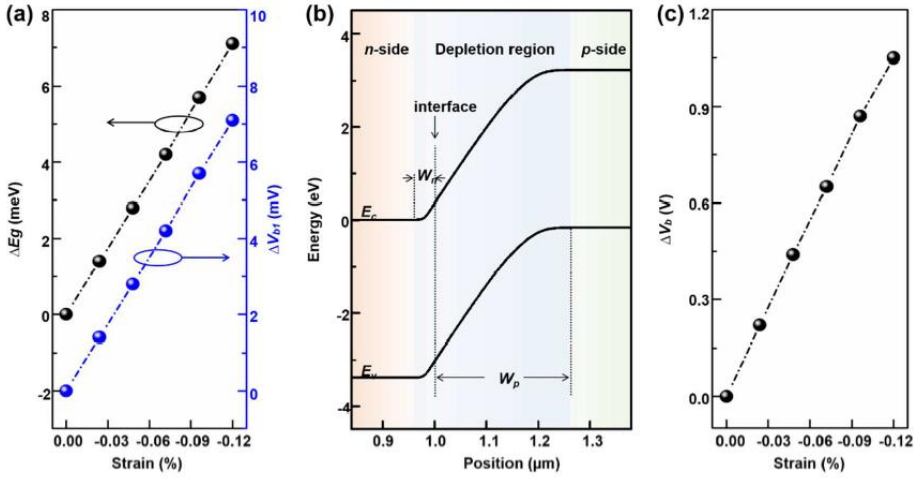

Figure 47 (a) Reduction of GaN bandgap (ΔE_g) and built-in electric potential difference (ΔV_{d1}) caused by the strain-induced deformation as a function of externally applied compressive strain. (b) Theoretically simulated energy band diagram of GaN p-n junction. (c) The calculated total reduction of built-in electric field (ΔV_d) caused by external strain as a function of externally applied compressive strain.

The induced F_{pz}^{p} within p-GaN film and the reduced F_b effectively promote the holes injection from p-type into junction region, leading to more uniform carrier injection and higher radiative combination efficiency with electrons. More importantly, an electron potential dip is formed as a result of the local positive piezo-potential within depletion region induced by external compressive strain (lower right). The electrons injected from n-GaN can be temporarily trapped and accumulated in the potential dip and thus facilitates the radiative recombination with holes at p–n junction region. Furthermore, the formed electron potential dip also acts as a natural electron-blocking barrier to prevent the leakage of electrons into p-GaN region, giving rise to significantly reduced nonradiative combination in p-GaN region. According to the discussion above, the enhancement of light emission efficiency and suppression of efficiency droop in GaN-MW based LEDs can be

effectively and simultaneously achieved by engineering the energy band profile induced by piezo-phototronic effect.

In order to further confirm our experimental results, the *c*-axis orientation of n-GaN MW was inverted by micromanipulation with its *c*-axis pointing to p-GaN film and +*c* plane contacted with p-GaN film (Figure 48a). EL characteristics of this kind of LEDs collected under various compressive strains (Figure 48b) exhibit that the light emission intensity decreases gradually with increasing the externally applied compressive strain. Theoretical simulations of this kind of LEDs were also conducted under a −0.12% compressive strain to understand and confirm the physical mechanisms (Figure 48c,d). Experimentally, 28 devices were fabricated by manipulating the *c*-axis orientation of GaN MW pointing to p-GaN (downward) or away from p-GaN (upward). 18 LEDs among them with *c*-axis of GaN MW pointing upward exhibit enhanced light emission and reduced efficiency droop under compressive strain, exhibiting the same trends and approximate magnitude of change. The other 10 LEDs with *c*-axis of GaN MW pointing downward exhibit obviously reduced emitting light intensity as increasing the externally applied compressive strain. This fact indicates that the observed performances optimization in our GaN p–n junction LEDs is dominated by polar piezo-potential effect rather than any nonpolar effects such as change in contact-area and/or piezoresistance.

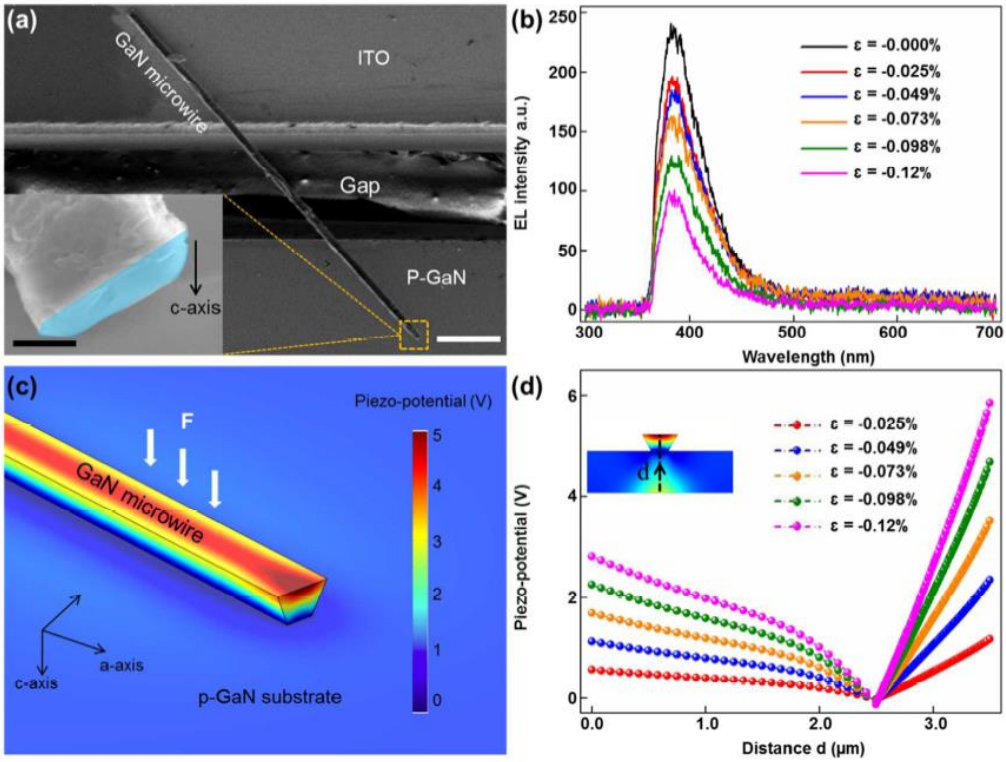

Figure 48 Experimental and theoretical simulation results of the GaN MW-based LEDs with inverted *c*-axis orientation for *n*-GaN MW. (a) Overall view SEM image of the as-fabricated LEDs; Inset: The corresponding end surface of *n*-GaN MW. (b) EL characteristics of this kind LEDs are collected under various compressive strains. (c) Under -0.12% compressive strain, the overall view of piezo-potential distribution within the GaN MW-based LEDs. (d) Piezo-potential values across the LED device normal to the *p-n* junction interface; inset: cross-section view of piezo-potential distribution within the GaN MW-based LEDs under -0.12% compressive strain.

In conclusion, the piezo-phototronic effect is utilized to simultaneously enhance the quantum efficiency and suppress the efficiency droop in GaN MW-based p–n homojunction UV LEDs. By applying a −0.12% compressive strain perpendicular to the p–n junction interface, the relative EQE of the LEDs is enhanced by over 600%. The efficiency droop is significantly reduced from 46.6% to 7.5% and corresponding droop onset current density shifts from 10 to 26.7 A cm^{-2} when the piezo-phototronic effect is introduced by applying a −0.12% static compressive strain. The corresponding physical mechanisms are carefully proposed and fully confirmed by theoretical calculations. This

study not only presents in-depth understandings about the piezo-phototronic effect in p–n homojunctions but also offers a novel approach to develop high efficiency, strong brightness and high power III-Nitride visible/UV light emitters.

CHAPTER 5. CONCLUSION

5.1 Summary of Work

In this dissertation, I have presented my major research achievements during my doctoral research. I was dedicated to investigating the application of piezotronic and piezo-phototronic effects on performance of various devices and the optoelectronic processes especially charge carrier transport processes both theoretically and experimentally. These results indicate that the universality of piezotronic and piezo-phototronic effects as effective approaches to modify the physical properties of charge carriers in piezoelectric semiconductors.

The general performance of the broadband photodiodes can be further improved by the piezo‐phototronic effect. The enhancement of responsivity can reach a maximum of 78% to 442 nm illumination, the linearity and saturation limit to 1060 nm light are also significantly increased by applying external strains. The photodiode is illuminated with different wavelength lights to selectively choose the photogenerated charge carriers (either electrons or holes) passing through the depletion region, to investigate the piezo‐phototronic effect on electron or hole transport separately for the first time.

Instead of the conventional p–n junction and p–intrinsic–n junction, we introduce a ~15 nm thick alumina insulator layer between a p-type Si substrate and n-type ZnO nanowire (NW) arrays, which significantly enhances the charge carrier separation and collection efficiency. The photosensing responsivity and sensitivity are found to be nearly 1 order of magnitude higher than that of a reference device of p-Si/n-ZnO NW arrays,

significantly higher than the commercial silicon photodiodes as well. The light-induced charge carriers flow across the appropriate thickness of insulator layer via the quantum mechanical Fowler–Nordheim tunneling mechanism. By virtue of the piezo-phototronic effect, the charge density at the interfaces can be tuned to alter the energy bands and the potential barrier distance for tunneling. Additionally, along with the use of incident light of different wavelengths, the influence of the insulator layer on the transport of electrons and holes separately is further investigated.

By introducing an external tensile strain, the performance of PDs is enhanced by 76.7% upon 0.2 mW/cm^2 442 nm light illumination for $CdS_{0.85}Se_{0.15}$ by the piezo-phototronic effect. The composition effect of materials in ternary materials on light detecting and piezo-phototronics was also first investigated systematically. The results indicate that in the CdS_xSe_{1-x} system, as the value of x decreases, the photocurrent and responsivity experience an increase, while the enhancement of the piezo-phototronic effect was weakened. The change in piezoelectric coefficient and carrier screening effect are proposed for the observed phenomenon. This study reports a high-quality ternary CdSxSe1–x NWs system used for high-performance PDs, broadens the family of piezotronic materials, offers an innovative material for high-performance visible PD, and provides a new pathway to modulate the performance of piezo-phototronic devices by tuning the atomic ratios of ternary wurtzite semiconducting materials.

Here, we demonstrate the significantly enhanced light-output efficiency and suppressed efficiency droop in GaN microwire (MW)-based p–n junction ultraviolet light-emitting diode (UV LED) by the piezo-phototronic effect. By applying a −0.12% static compressive strain perpendicular to the p–n junction interface, the relative external

quantum efficiency of the LED is enhanced by over 600%. Furthermore, efficiency droop is markedly reduced from 46.6% to 7.5% and corresponding droop onset current density shifts from 10 to 26.7 A cm^{-2}. Enhanced electrons confinement and improved holes injection efficiency by the piezo-phototronic effect are revealed and theoretically confirmed as the physical mechanisms. This study offers an unconventional path to develop high efficiency, strong brightness and high power III-nitride light sources.

These results are essential for studying the basic principles in order to develop a full understanding about piezotronics and it also enables the development of the better performance of optoelectronics.

5.2 Future work

Although a considerable amount of work have been done by using the piezoelectric effect and piezo-phototronic effect on various structure of devices, both fundamental theory and application work are needed for future investigations. There are several aspects can be further studied:

1. Fundamental theory study of piezotronic and piezo-phototronic effects on optoelectronic processes. In this thesis, we have found that the piezo-charges induced by the strains would have different influence on the electron and hole transport. We can further introduce piezo-charges on another side or both sides, or induce different piezo-charges by using compressive or tensile strains, so that they can reveal the full picture of the effect of piezo-charges on the optoelectronic processes. This result would help us to analysis how to design the electronic devices so as to improve the performance or tailor optoelectronic processes in different optoelectronic devices by these effects in a right way.

2. Piezo-phototronic effect on devices based on various structures. Here, we have studied the p-n, and p-insulator-n, other structures such as Ohmic contact, and Schottky contact have been widely studied. P-intrinsic-n has demonstrated high performance in photonics, like solar cells, and photodetectors; in addition, metal-insulator-semiconductor has been widely studied and used in many products. However, the study of piezo-phototronic effect on these devices is rare. More researches based on various structure would accelerate fundamental theory development and further promote the application of piezo-phototronic effect.
3. It is of great importance to find a way to conduct in-situ explorations about the modulation of energy states, structure change, and charge transfer etc. by the piezo-charges.
4. Expanding the materials system is urgent. Although, a lot of researches have been done to demonstrate the piezo-phototronic effect on piezoelectric semiconductor materials, for instance, ZnO, GaN, CdS, CdSe etc. However, there are a lot of piezoelectric semiconductors materials have been studied and even used in industry, and operating systems, such as GaAs, perovskite, and many 2-D materials, but the piezo-phototronic effect on the devices based on these materials are scarce. Studies to verify the universality of this effect are also necessary and important.
5. Wider applications of piezotronic and piezo-phototronic effects are of great importance. Large amount of reports on photodetectors and LEDs have been published, but the piezo-phototronic effect on solar cells, electrochemical processes, energy storages and quantum dots are still limited and incomplete. Therefore, there exists a great opportunity right now to systematically study the piezotronic and piezo-phototronic effect on different types of devices.
6. Explore how to push this field towards commercialization in the future. Since the establishment of the field of piezotronics in year 2007 and piezo-phototronics in year

2010, the fundamental physics have been carefully studied and a number of application have been demonstrated to advance this field in the recent years. All practical applications of piezotronics and piezo-phototronics so far are based on lab-scale flexible devices, it is significant to demonstrate the feasibility to apply the effects to commercialized devices.

REFERENCES

1. http://www.iabrasive.com/articles/rise-of-the-3rd-generation-semiconductor-silicon-carbide-technology (accessed Oct 10, 2018).

2. Ilican, S.; Caglar, Y.; Caglar, M., Preparation and Characterization of Zno Thin Films Deposited by Sol-Gel Spin Coating Method. *J Optoelectron Adv M* **2008,** *10*, 2578-2583.

3. Zhang, K. M.; Zhao, Y. P.; He, F. Q.; Liu, D. Q., Piezoelectricity of Zno Films Prepared by Sol-Gel Method. *Chinese J Chem Phys* **2007,** *20*, 721-726.

4. Znaidi, L., Sol-Gel-Deposited Zno Thin Films: A Review. *Mater Sci Eng B-Adv* **2010,** *174*, 18-30.

5. Fang, T. H.; Kang, S. H., Physical Properties of Zno: Al Nanorods for Piezoelectric Nanogenerator Application. *Curr Nanosci* **2010,** *6*, 505-511.

6. Wang, Z. L., Energy Harvesting Using Piezoelectric Nanowires-a Correspondence on "Energy Harvesting Using Nanowires?" By Alexe Et Al. *Adv Mater* **2009,** *21*, 1311-1315.

7. Kong, X. Y.; Wang, Z. L., Spontaneous Polarization-Induced Nanohelixes, Nanosprings, and Nanorings of Piezoelectric Nanobelts. *Nano Lett* **2003,** *3*, 1625-1631.

8. Ito, Y.; Kushida, K.; Sugawara, K.; Takeuchi, H., A 100-Mhz Ultrasonic Transducer Array Using Zno Thin-Films. *Ieee T Ultrason Ferr* **1995,** *42*, 316-324.

9. Wang, Z. L., Nanopiezotronics. *Adv Mater* **2007,** *19*, 889-892.

10. Wang, Z. L., The New Field of Nanopiezotronics. *Mater Today* **2007,** *10*, 20-28.

11. Wang, Z. L.; Wu, W. Z., Piezotronics and Piezo-Phototronics: Fundamentals and Applications. *Natl Sci Rev* **2014,** *1*, 62-90.

12. Wang, Z. L., Progress in Piezotronics and Piezo-Phototronics. *Adv Mater* **2012,** *24*, 4632-4646.

13. Pan, Z. W.; Dai, Z. R.; Wang, Z. L., Nanobelts of Semiconducting Oxides. *Science* **2001,** *291*, 1947-1949.

14. Heo, Y. W.; Varadarajan, V.; Kaufman, M.; Kim, K.; Norton, D. P.; Ren, F.; Fleming, P. H., Site-Specific Growth of Zno Nanorods Using Catalysis-Driven Molecular-Beam Epitaxy. *Appl Phys Lett* **2002,** *81*, 3046-3048.

15. Greene, L. E.; Yuhas, B. D.; Law, M.; Zitoun, D.; Yang, P. D., Solution-Grown Zinc Oxide Nanowires. *Inorg Chem* **2006,** *45*, 7535-7543.

16. Xu, S.; Adiga, N.; Ba, S.; Dasgupta, T.; Wu, C. F. J.; Wang, Z. L., Optimizing and Improving the Growth Quality of Zno Nanowire Arrays Guided by Statistical Design of Experiments. *Acs Nano* **2009,** *3*, 1803-1812.

17. Xu, S.; Lao, C.; Weintraub, B.; Wang, Z. L., Density-Controlled Growth of Aligned Zno Nanowire Arrays by Seedless Chemical Approach on Smooth Surfaces. *J Mater Res* **2008,** *23*, 2072-2077.

18. Song, J.; Baek, S.; Lee, J.; Lim, S., Role of Oh- in the Low Temperature Hydrothermal Synthesis of Zno Nanorods. *J Chem Technol Biot* **2008,** *83*, 345-350.

19. Li, W. J.; Shi, E. W.; Zhong, W. Z.; Yin, Z. W., Growth Mechanism and Growth Habit of Oxide Crystals. *J Cryst Growth* **1999,** *203*, 186-196.

20. Gong, X.; Tong, M. H.; Xia, Y. J.; Cai, W. Z.; Moon, J. S.; Cao, Y.; Yu, G.; Shieh, C. L.; Nilsson, B.; Heeger, A. J., High-Detectivity Polymer Photodetectors with Spectral Response from 300 Nm to 1450 Nm. *Science* **2009,** *325*, 1665-1667.

21. Middelhoek, S.; Audet, S. A. *Silicon Sensors*; Academic Press: 1989.

22. Sze, S. M.; Ng, K. K. *Physics of Semiconductor Devices*; John wiley & sons: 2006.

23. Yu, R. M.; Niu, S. M.; Pan, C. F.; Wang, Z. L., Piezotronic Effect Enhanced Performance of Schottky-Contacted Optical, Gas, Chemical and Biological Nanosensors. *Nano Energy* **2015,** *14*, 312-339.

24. Han, X.; Chen, M. X.; Pan, C. F.; Wang, Z. L., Progress in Piezo-Phototronic Effect Enhanced Photodetectors. *J Mater Chem C* **2016,** *4*, 11341-11354.

25. Wang, Z. L.; Chen, J.; Lin, L., Progress in Triboelectric Nanogenerators as a New Energy Technology and Self-Powered Sensors. *Energ Environ Sci* **2015,** *8*, 2250-2282.

26. Chen, J.; Huang, Y.; Zhang, N.; Zou, H.; Liu, R.; Tao, C.; Fan, X.; Wang, Z. L., Micro-Cable Structured Textile for Simultaneously Harvesting Solar and Mechanical Energy. *Nature Energy* **2016,** *1*, 16138.

27. Wu, W. Z.; Wen, X. N.; Wang, Z. L., Taxel-Addressable Matrix of Vertical-Nanowire Piezotronic Transistors for Active and Adaptive Tactile Imaging. *Science* **2013,** *340*, 952-957.

28. Almeida, V. R.; Barrios, C. A.; Panepucci, R. R.; Lipson, M., All-Optical Control of Light on a Silicon Chip. *Nature* **2004,** *431*, 1081-4.

29. Lipson, M., Guiding, Modulating, and Emitting Light on Silicon - Challenges and Opportunities. *J Lightwave Technol* **2005,** *23*, 4222-4238.

30. Zou, H. Y.; Chen, J.; Fang, Y. N.; Ding, J. L.; Peng, W. B.; Liu, R. Y., A Dual-Electrolyte Based Air-Breathing Regenerative Microfluidic Fuel Cell with 1.76 V Open-Circuit-Voltage and 0.74 V Water-Splitting Voltage. *Nano Energy* **2016,** *27*, 619-626.

31. Liu, J.-M. *Photonic Devices*; Cambridge: Cambridge ; New York, 2005; p. li, 1052 p.

32. Juntunen, M. A.; Heinonen, J.; Vähänissi, V.; Repo, P.; Valluru, D.; Savin, H., Near-Unity Quantum Efficiency of Broadband Black Silicon Photodiodes with an Induced Junction. *Nature Photonics* **2016,** *10*, 777-781.

33. Wu, C.; Crouch, C. H.; Zhao, L.; Carey, J. E.; Younkin, R.; Levinson, J. A.; Mazur, E.; Farrell, R. M.; Gothoskar, P.; Karger, A., Near-Unity Below-Band-Gap Absorption by Microstructured Silicon. *Appl Phys Lett* **2001,** *78*, 1850-1852.

34. Hu, Y.; Chang, Y.; Fei, P.; Snyder, R. L.; Wang, Z. L., Designing the Electric Transport Characteristics of Zno Micro/Nanowire Devices by Coupling Piezoelectric and Photoexcitation Effects. *Acs Nano* **2010,** *4*, 1234-40.

35. Chen, M. X.; Pan, C. F.; Zhang, T. P.; Li, X. Y.; Liang, R. R.; Wang, Z. L., Tuning Light Emission of a Pressure-Sensitive Silicon/Zno Nanowires Heterostructure Matrix through Piezo-Phototronic Effects. *Acs Nano* **2016,** *10*, 6074-6079.

36. Wu, W.; Wang, L.; Yu, R.; Liu, Y.; Wei, S. H.; Hone, J.; Wang, Z. L., Piezophototronic Effect in Single-Atomic-Layer Mos2 for Strain-Gated Flexible Optoelectronics. *Adv Mater* **2016,** *28*, 8463-8468.

37. Peng, W.; Yu, R.; Wang, X.; Wang, Z.; Zou, H.; He, Y.; Wang, Z. L., Temperature Dependence of Pyro-Phototronic Effect on Self-Powered Zno/Perovskite Heterostructured Photodetectors. *Nano Research* **2016**, 1-10.

38. Wu, W.; Wen, X.; Wang, Z. L., Taxel-Addressable Matrix of Vertical-Nanowire Piezotronic Transistors for Active and Adaptive Tactile Imaging. *Science* **2013,** *340*, 952-957.

39. Yang, Q.; Guo, X.; Wang, W. H.; Zhang, Y.; Xu, S.; Lien, D. H.; Wang, Z. L., Enhancing Sensitivity of a Single Zno Micro-/Nanowire Photodetector by Piezo-Phototronic Effect. *Acs Nano* **2010,** *4*, 6285-6291.

40. Zhang, F.; Ding, Y.; Zhang, Y.; Zhang, X. L.; Wang, Z. L., Piezo-Phototronic Effect Enhanced Visible and Ultraviolet Photodetection Using a Zno-Cds Core-Shell Micro/Nanowire. *Acs Nano* **2012,** *6*, 9229-9236.

41. Pan, C. F.; Dong, L.; Zhu, G.; Niu, S. M.; Yu, R. M.; Yang, Q.; Liu, Y.; Wang, Z. L., High-Resolution Electroluminescent Imaging of Pressure Distribution Using a Piezoelectric Nanowire Led Array. *Nature Photonics* **2013,** *7*, 752-758.

42. Wang, C. F.; Ba, R. R.; Zhao, K.; Zhang, T. P.; Dong, L.; Pan, C. F., Enhanced Emission Intensity of Vertical Aligned Flexible Zno Nanowire/P-Polymer Hybridized Led Array by Piezo-Phototronic Effect. *Nano Energy* **2015,** *14*, 364-371.

43. Liu, Y.; Zhang, Y.; Yang, Q.; Niu, S. M.; Wang, Z. L., Fundamental Theories of Piezotronics and Piezo-Phototronics. *Nano Energy* **2015,** *14*, 257-275.

44. Fan, Z. Y.; Chang, P. C.; Lu, J. G.; Walter, E. C.; Penner, R. M.; Lin, C. H.; Lee, H. P., Photoluminescence and Polarized Photodetection of Single Zno Nanowires. *Appl Phys Lett* **2004,** *85*, 6128-6130.

45. Schwing, U.; Hoffmann, B., Model Experiments Describing the Microcontact of Zno Varistors. *J Appl Phys* **1985,** *57*, 5372-5379.

46. Chan, Y. F.; Su, W.; Zhang, C. X.; Wu, Z. L.; Tang, Y.; Sun, X. Q.; Xu, H. J., Electroluminescence from Zno-Nanofilm/Si-Micropillar Heterostructure Arrays. *Opt Express* **2012,** *20*, 24280-24287.

47. Wang, Z. L. *Piezotronics and Piezo-Phototronics*; 1st ed.; Springer: New York, 2013.

48. Saleh, B. E.; Teich, M. C.; Saleh, B. E. *Fundamentals of Photonics*; Wiley New York: 1991; Vol. 22.

49. Carey, J. E.; Crouch, C. H.; Shen, M.; Mazur, E., Visible and near-Infrared Responsivity of Femtosecond-Laser Microstructured Silicon Photodiodes. *Optics Letters* **2005,** *30*, 1773-1775.

50. Franta, B.; Pastor, D.; Gandhi, H. H.; Rekemeyer, P. H.; Gradečak, S.; Aziz, M. J.; Mazur, E., Simultaneous High Crystallinity and Sub-Bandgap Optical Absorptance in Hyperdoped Black Silicon Using Nanosecond Laser Annealing. *J Appl Phys* **2015,** *118*, 225303.

51. Sharma, P.; Sreenivas, K.; Rao, K. V., Analysis of Ultraviolet Photoconductivity in Zno Films Prepared by Unbalanced Magnetron Sputtering. *J Appl Phys* **2003,** *93*, 3963-3970.

52. Ahn, S. E.; Lee, J. S.; Kim, H.; Kim, S.; Kang, B. H.; Kim, K. H.; Kim, G. T., Photoresponse of Sol-Gel-Synthesized Zno Nanorods. *Appl Phys Lett* **2004,** *84*, 5022-5024.

53. Chen, M.; Hu, L. F.; Xu, J. X.; Liao, M. Y.; Wu, L. M.; Fang, X. S., Zno Hollow-Sphere Nanofilm-Based High-Performance and Low-Cost Photodetector. *Small* **2011,** *7*, 2449-2453.

54. Hu, L. F.; Yan, J.; Liao, M. Y.; Xiang, H. J.; Gong, X. G.; Zhang, L. D.; Fang, X. S., An Optimized Ultraviolet-a Light Photodetector with Wide-Range Photoresponse Based on Zns/Zno Biaxial Nanobelt. *Adv Mater* **2012,** *24*, 2305-2309.

55. Zhang, T. C.; Guo, Y.; Mei, Z. X.; Gu, C. Z.; Du, X. L., Visible-Blind Ultraviolet Photodetector Based on Double Heterojunction of N-Zno/Insulator-Mgo/P-Si. *Appl Phys Lett* **2009,** *94*.

56. Wang, Z. N.; Yu, R. M.; Wen, X. N.; Liu, Y.; Pan, C. F.; Wu, W. Z.; Wang, Z. L., Optimizing Performance of Silicon-Based P-N Junction Photodetectors by the Piezo-Phototronic Effect. *Acs Nano* **2014,** *8*, 12866-12873.

57. Selman, A. M.; Hassan, Z.; Husham, M.; Ahmed, N. M., A High-Sensitivity, Fast-Response, Rapid-Recovery P-N Heterojunction Photodiode Based on Rutile Tio2 Nanorod Array on P-Si(111). *Appl Surf Sci* **2014,** *305*, 445-452.

58. Sze, S. M. *Physics of Semiconductor-Devices*; 1982.

59. Liu, Y.; Niu, S. M.; Yang, Q.; Klein, B. D. B.; Zhou, Y. S.; Wang, Z. L., Theoretical Study of Piezo-Phototronic Nano-Leds. *Adv Mater* **2014,** *26*, 7209-7216.

60. Janotti, A.; Van de Walle, C. G., Fundamentals of Zinc Oxide as a Semiconductor. *Rep Prog Phys* **2009,** *72*.

61. Wu, W. Z.; Wang, L.; Yu, R. M.; Liu, Y. Y.; Wei, S. H.; Hone, J.; Wang, Z. L., Piezophototronic Effect in Single-Atomic-Layer Mos2 for Strain-Gated Flexible Optoelectronics. *Adv Mater* **2016,** *28*, 8463-8468.

62. Yang, Q.; Guo, X.; Wang, W.; Zhang, Y.; Xu, S.; Lien, D. H.; Wang, Z. L., Enhancing Sensitivity of a Single Zno Micro-/Nanowire Photodetector by Piezo-Phototronic Effect. *Acs Nano* **2010,** *4*, 6285-91.

63. Chao, C. H.; Weng, W. J.; Wei, D. H., Enhanced Uv Photodetector Response and Recovery Times Using a Nonpolar Zno Sensing Layer. *J Vac Sci Technol A* **2016,** *34*.

64. Thomson, D.; Zilkie, A.; Bowers, J. E.; Komljenovic, T.; Reed, G. T.; Vivien, L.; Marris-Morini, D.; Cassan, E.; Virot, L.; Fédéli, J.-M., Roadmap on Silicon Photonics. *Journal of Optics* **2016,** *18*, 073003.

65. Hochberg, M.; Baehr-Jones, T., Towards Fabless Silicon Photonics. *Nature Photonics* **2010,** *4*, 492-494.

66. Atabaki, A. H.; Moazeni, S.; Pavanello, F.; Gevorgyan, H.; Notaros, J.; Alloatti, L.; Wade, M. T.; Sun, C.; Kruger, S. A.; Meng, H. Y.; Al Qubaisi, K.; Wang, I.; Zhang, B. H.; Khilo, A.; Baiocco, C. V.; Popovic, M. A.; Stojanovic, V. M.; Ram, R. J., Integrating Photonics with Silicon Nanoelectronics for the Next Generation of Systems on a Chip. *Nature* **2018,** *556*, 349.

67. Leuthold, J.; Koos, C.; Freude, W., Nonlinear Silicon Photonics. *Nature Photonics* **2010,** *4*, 535-544.

68. Liu, Y.; Das, A.; Lin, Z. Y.; Cooper, I. B.; Rohatgi, A.; Wong, C. P., Hierarchical Robust Textured Structures for Large Scale Self-Cleaning Black Silicon Solar Cells. *Nano Energy* **2014,** *3*, 127-133.

69. Ccama, A. G. https://www.slideshare.net/rathur/chap6-photodetectors (accessed Dec 21, 2018).

70. Quimby, R. S. *Photonics and Lasers: An Introduction*; John Wiley & Sons: 2006.

71. Buscema, M.; Island, J. O.; Groenendijk, D. J.; Blanter, S. I.; Steele, G. A.; van der Zant, H. S. J.; Castellanos-Gomez, A., Photocurrent Generation with Two-Dimensional Van Der Waals Semiconductors. *Chem Soc Rev* **2015,** *44*, 3691-3718.

72. Green, M. A., Solar Cells: Operating Principles, Technology, and System Applications. **1982**.

73. Mukherjee, S.; Das, K.; Kakati, A.; Soumen, D.; Ray, S. K.; Raychaudhuri, A. K. In *Single Silicon Nanowire Based Broadband Photodetector with Superior Responsivity*, International Conference on Fibre Optics and Photonics, Optical Society of America: 2014; p T3A. 69.

74. Juntunen, M. A.; Heinonen, J.; Vahanissi, V.; Repo, P.; Valluru, D.; Savin, H., Near-Unity Quantum Efficiency of Broadband Black Silicon Photodiodes with an Induced Junction. *Nature Photonics* **2016,** *10*, 777.

75. Spinelli, P.; Verschuuren, M. A.; Polman, A., Broadband Omnidirectional Antireflection Coating Based on Subwavelength Surface Mie Resonators. *Nat Commun* **2012,** *3*.

76. Kuo, M. L.; Poxson, D. J.; Kim, Y. S.; Mont, F. W.; Kim, L. K.; Schuhert, E. F.; Lin, S. Y., Realization of a near-Perfect Antireflection Coating for Silicon Solar Energy Utilization. *Optics Letters* **2008,** *33*, 2527-2529.

77. Shi, E. Z.; Li, H. B.; Yang, L.; Zhang, L. H.; Li, Z.; Li, P. X.; Shang, Y. Y.; Wu, S. T.; Li, X. M.; Wei, J. Q.; Wang, K. L.; Zhu, H. W.; Wu, D. H.; Fang, Y.; Cao, A. Y., Colloidal Antireflection Coating Improves Graphene-Silicon Solar Cells. *Nano Lett* **2013,** *13*, 1776-1781.

78. Nagel, H.; Aberle, A. G.; Hezel, R., Optimised Antireflection Coatings for Planar Silicon Solar Cells Using Remote Pecvd Silicon Nitride and Porous Silicon Dioxide. *Prog Photovoltaics* **1999,** *7*, 245-260.

79. Michel, J.; Liu, J. F.; Kimerling, L. C., High-Performance Ge-on-Si Photodetectors. *Nature Photonics* **2010,** *4*, 527-534.

80. Zou, H. Y.; Li, X. G.; Peng, W. B.; Wu, W. Z.; Yu, R. M.; Wu, C. S.; Ding, W. B.; Hu, F.; Liu, R. Y.; Zi, Y. L.; Wang, Z. L., Piezo-Phototronic Effect on Selective Electron

or Hole Transport through Depletion Region of Vis-Nir Broadband Photodiode. *Adv Mater* **2017,** *29*.

81. Pradel, K. C.; Wu, W. Z.; Zhou, Y. S.; Wen, X. N.; Ding, Y.; Wang, Z. L., Piezotronic Effect in Solution-Grown P-Type Zno Nanowires and Films. *Nano Lett* **2013,** *13*, 2647-2653.

82. Pradel, K. C.; Wu, W. Z.; Ding, Y.; Wang, Z. L., Solution-Derived Zno Homojunction Nanowire Films on Wearable Substrates for Energy Conversion and Self-Powered Gesture Recognition. *Nano Lett* **2014,** *14*, 6897-6905.

83. Sun, T.; Wang, R. B.; Liu, R. Y.; Wu, C.; Zhong, Y. N.; Liu, Y. Q.; Wang, Y. S.; Han, Y. J.; Xia, Z. H.; Zou, Y. T.; Song, T.; Koch, N.; Duhm, S.; Sun, B. Q., Investigation of Moox/N-Si Strong Inversion Layer Interfaces Via Dopant-Free Heterocontact. *Phys Status Solidi-R* **2017,** *11*.

84. Sze, S. M.; Ng, K. K. *Physics of Semiconductor Devices*; John Wiley & Sons: Hoboken, 2006; p. 197-238.

85. Ranuarez, J. C.; Deen, M. J.; Chen, C. H., A Review of Gate Tunneling Current in Mos Devices. *Microelectron Reliab* **2006,** *46*, 1939-1956.

86. Dai, G. Z.; Zou, H. Y.; Wang, X. F.; Zhou, Y. K.; Wang, P. H.; Ding, Y.; Zhang, Y.; Yang, J. L.; Wang, Z. L., Piezo-Phototronic Effect Enhanced Responsivity of Photon Sensor Based on Composition-Tunable Ternary Cdsxse1-X Nanowires. *Acs Photonics* **2017,** *4*, 2495-2503.

87. Wang, Z. N.; Yu, R. M.; Pan, C. F.; Liu, Y.; Ding, Y.; Wang, Z. L., Piezo-Phototronic Uv/Visible Photosensing with Optical-Fiber-Nanowire Hybridized Structures. *Adv Mater* **2015,** *27*, 1553-+.

88. Wu, W. Z.; Wang, Z. L., Piezotronics and Piezo-Phototronics for Adaptive Electronics and Optoelectronics. *Nat Rev Mater* **2016,** *1*.

89. Wang, Z. L., Piezopotential Gated Nanowire Devices: Piezotronics and Piezo-Phototronics. *Nano Today* **2010,** *5*, 540-552.

90. Zhu, L. P.; Wang, L. F.; Pan, C. F.; Chen, L. B.; Xue, F.; Chen, B. D.; Yang, L. J.; Su, L.; Wang, Z. L., Enhancing the Efficiency of Silicon-Based Solar Cells by the Piezo-Phototronic Effect. *Acs Nano* **2017,** *11*, 1894-1900.

91. Zhang, Y.; Wang, Z. L., Theory of Piezo-Phototronics for Light-Emitting Diodes. *Adv Mater* **2012,** *24*, 4712-4718.

92. Liu, Y.; Yang, Q.; Zhang, Y.; Yang, Z. Y.; Wang, Z. L., Nanowire Piezo-Phototronic Photodetector: Theory and Experimental Design. *Adv Mater* **2012,** *24*, 1410-1417.

93. Song, W. D.; Wang, X. F.; Xia, C.; Wang, R. P.; Zhao, L. L.; Guo, D. X.; Chen, H.; Xiao, J. K.; Su, S. C.; Li, S. T., Improved Photoresponse of a-Axis Gan Microwire/P-Polymer Hybrid Photosensor by the Piezo-Phototronic Effect. *Nano Energy* **2017,** *33*, 272-279.

94. Zhang, F.; Niu, S. M.; Guo, W. X.; Zhu, G.; Liu, Y.; Zhang, X. L.; Wang, Z. L., Piezo-Phototronic Effect Enhanced Visible/Uv Photodetector of a Carbon-Fiber/Zno-Cds Double-Shell Microwire. *Acs Nano* **2013,** *7*, 4537-4544.

95. Han, X.; Du, W. M.; Yu, R. M.; Pan, C. F.; Wang, Z. L., Piezo-Phototronic Enhanced Uv Sensing Based on a Nanowire Photodetector Array. *Adv Mater* **2015,** *27*, 7963-7969.

96. Wang, X.; Yu, R.; Jiang, C.; Hu, W.; Wu, W.; Ding, Y.; Peng, W.; Li, S.; Wang, Z. L., Piezotronic Effect Modulated Heterojunction Electron Gas in Algan/Aln/Gan Heterostructure Microwire. *Adv Mater* **2016,** *28*, 7234-42.

97. Wang, X. F.; Yu, R. M.; Peng, W. B.; Wu, W. Z.; Li, S. T.; Wang, Z. L., Temperature Dependence of the Piezotronic and Piezophototronic Effects in a-Axis Gan Nanobelts. *Adv Mater* **2015,** *27*, 8067-8074.

98. Yang, Y.; Guo, W. X.; Pradel, K. C.; Zhu, G.; Zhou, Y. S.; Zhang, Y.; Hu, Y. F.; Lin, L.; Wang, Z. L., Pyroelectric Nanogenerators for Harvesting Thermoelectric Energy. *Nano Lett* **2012,** *12*, 2833-2838.

99. Wang, Z. L.; Song, J. H., Piezoelectric Nanogenerators Based on Zinc Oxide Nanowire Arrays. *Science* **2006,** *312*, 242-246.

100. Yu, R. M.; Wang, X. F.; Wu, W. Z.; Pan, C. F.; Bando, Y.; Fukata, N.; Hu, Y. F.; Peng, W. B.; Ding, Y.; Wang, Z. L., Temperature Dependence of the Piezophototronic Effect in Cds Nanowires. *Adv Funct Mater* **2015,** *25*, 5277-5284.

101. Zhou, Y. S.; Wang, K.; Han, W. H.; Rai, S. C.; Zhang, Y.; Ding, Y.; Pan, C. F.; Zhang, F.; Zhou, W. L.; Wang, Z. L., Vertically Aligned Cdse Nanowire Arrays for Energy Harvesting and Piezotronic Devices. *Acs Nano* **2012,** *6*, 6478-6482.

102. Dong, L.; Niu, S. M.; Pan, C. F.; Yu, R. M.; Zhang, Y.; Wang, Z. L., Piezo-Phototronic Effect of Cdse Nanowires. *Adv Mater* **2012,** *24*, 5470-5475.

103. Yu, X. X.; Yin, H.; Li, H. X.; Zhang, W.; Zhao, H.; Li, C.; Zhu, M. Q., Piezo-Phototronic Effect Modulated Self-Powered Uv/Visible/near-Infrared Photodetectors Based on Cds:P3ht Microwires. *Nano Energy* **2017,** *34*, 155-163.

104. Zhuang, X. J.; Ning, C. Z.; Pan, A. L., Composition and Bandgap-Graded Semiconductor Alloy Nanowires. *Adv Mater* **2012,** *24*, 13-33.

105. Kuykendall, T.; Ulrich, P.; Aloni, S.; Yang, P., Complete Composition Tunability of Ingan Nanowires Using a Combinatorial Approach. *Nat Mater* **2007,** *6*, 951-956.

106. Pan, A. L.; Yang, H.; Liu, R. B.; Yu, R. C.; Zou, B. S.; Wang, Z. L., Color-Tunable Photoluminescence of Alloyed Cdsxse1-X Nanobelts. *J Am Chem Soc* **2005,** *127*, 15692-15693.

107. Ye, J. D.; Gu, S. L.; Zhu, S. M.; Liu, S. M.; Zheng, Y. D.; Zhang, R.; Shi, Y., Fermi-Level Band Filling and Band-Gap Renormalization in Ga-Doped Zno. *Appl Phys Lett* **2005,** *86*, 192111.

108. Zhang, Q. L.; Liu, H. W.; Guo, P. F.; Li, D.; Fan, P.; Zheng, W. H.; Zhu, X. L.; Jiang, Y.; Zhou, H.; Hu, W.; Zhuang, X. J.; Liu, H. J.; Duan, X. F.; Pan, A. L., Vapor Growth and Interfacial Carrier Dynamics of High-Quality Cds-Cdsse-Cds Axial Nanowire Heterostructures. *Nano Energy* **2017,** *32*, 28-35.

109. Guo, P. F.; Xu, J. Y.; Gong, K.; Shen, X.; Lu, Y.; Qiu, Y.; Xu, J. Q.; Zou, Z. J.; Wang, C. L.; Yan, H. L.; Luo, Y. S.; Pan, A. L.; Zhang, H.; Ho, J. C.; Yu, K. M., On-Nanowire Axial Heterojunction Design for High-Performance Photodetectors. *Acs Nano* **2016,** *10*, 8474-8481.

110. Li, L.; Lu, H.; Yang, Z. Y.; Tong, L. M.; Bando, Y.; Golberg, D., Bandgap-Graded Cdsxse1x Nanowires for High-Performance Field-Effect Transistors and Solar Cells. *Adv Mater* **2013,** *25*, 1109-1113.

111. Xu, J. Y.; Zhuang, X. J.; Guo, P. F.; Zhang, Q. L.; Huang, W. Q.; Wan, Q.; Hu, W.; Wang, X. X.; Zhu, X. L.; Fan, C. Z.; Yang, Z. Y.; Tong, L. M.; Duan, X. F.; Pan, A. L., Wavelength-Converted/Selective Waveguiding Based on Composition-Graded Semiconductor Nanowires. *Nano Lett* **2012,** *12*, 5003-5007.

112. Dai, G. Z.; Liu, R. B.; Wan, Q.; Zhang, Q. L.; Pan, A. L.; Zou, B. S., Color-Tunable Periodic Spatial Emission of Alloyed Cds1-Xsex/Sn: Cds1-Xsex Superlattice Microwires. *Opt Mater Express* **2011,** *1*, 1185-1191.

113. Pan, A.; Wang, X.; He, P. B.; Zhang, O. L.; Wan, Q.; Zacharias, M.; Zhu, X.; Zou, B. S., Color-Changeable Optical Transport through Se-Doped Cds 1d Nanostructures. *Nano Lett* **2007,** *7*, 2970-2975.

114. Liu, Y. K.; Zapien, J. A.; Shan, Y. Y.; Tang, H.; Lee, C. S.; Lee, S. T., Wavelength-Tunable Lasing in Single-Crystal Cds1-Xsex Nanoribbons. *Nanotechnology* **2007,** *18*.

115. Pan, A. L.; Liu, R. B.; Wang, F. F.; Xie, S. S.; Zou, B. S.; Zacharias, M.; Wang, Z. L., High-Quality Alloyed Cdsxse1-X Whiskers as Waveguides with Tunable Stimulated Emission. *J Phys Chem B* **2006,** *110*, 22313-22317.

116. Chen, Y. Y.; Wang, C. H.; Chen, G. S.; Li, Y. C.; Liu, C. P., Self-Powered N-Mgxzn1-Xo/P-Si Photodetector Improved by Alloying-Enhanced Piezopotential through Piezo-Phototronic Effect. *Nano Energy* **2015,** *11*, 533-539.

117. Perna, G.; Pagliara, S.; Capozzi, V.; Ambrico, M.; Ligonzo, T., Optical Characterization of Cdsxse1-X Films Grown on Quartz Substrate by Pulsed Laser Ablation Technique. *Thin Solid Films* **1999,** *349*, 220-224.

118. Zhang, K. Y.; Hu, C. G.; Tian, Y. S.; Zheng, C. H.; Wan, B. Y., Stable and Highly Photosensitive Device of Cdse Nanorods. *Physica E* **2011,** *43*, 943-947.

119. Yin, L.; Yang, L.; Yang, W.; Guo, Y.; Ma, K.; Li, S.; Zhang, J., Thermal Design and Analysis of Multi-Chip Led Module with Ceramic Substrate. *Solid-State Electronics* **2010,** *54*, 1520-1524.

120. Littig, A.; Lehmann, H.; Klinke, C.; Kipp, T.; Mews, A., Solution-Grown Nanowire Devices for Sensitive and Fast Photodetection. *Acs Appl Mater Inter* **2015,** *7*, 12184-12192.

121. Li, L.; Wu, P. C.; Fang, X. S.; Zhai, T. Y.; Dai, L.; Liao, M. Y.; Koide, Y.; Wang, H. Q.; Bando, Y.; Golberg, D., Single-Crystalline Cds Nanobelts for Excellent Field-Emitters and Ultrahigh Quantum-Efficiency Photodetectors. *Adv Mater* **2010,** *22*, 3161-3165.

122. Takahashi, T.; Nichols, P.; Takei, K.; Ford, A. C.; Jamshidi, A.; Wu, M. C.; Ning, C. Z.; Javey, A., Contact Printing of Compositionally Graded Cdsxse1-X Nanowire Parallel Arrays for Tunable Photodetectors. *Nanotechnology* **2012,** *23*.

123. Zhou, J.; Fei, P.; Gu, Y. D.; Mai, W. J.; Gao, Y. F.; Yang, R.; Bao, G.; Wang, Z. L., Piezoelectric-Potential-Control Led Polarity-Reversible Schottky Diodes and Switches of Zno Wires. *Nano Lett* **2008,** *8*, 3973-3977.

124. Madelung, O.; Rössler, U.; Schulz, M., Landolt-Börnstein - Group Iii Condensed Matte. *Spring materials* **1999,** *41*.

125. Liu, H. W.; Lu, J. P.; Yang, Z. Y.; Teng, J. H.; Ke, L.; Zhang, X. H.; Tong, L. M.; Sow, C. H., Ultrahigh Photoconductivity of Bandgap-Graded Cdsxse1-X Nanowires Probed by Terahertz Spectroscopy. *Sci Rep-Uk* **2016,** *6*, 27387-27393.

126. Padovani, F. A.; Stratton, R., Field and Thermionic-Field Emission in Schottky Barriers. *Solid-State Electronics* **1966,** *9*, 695-707.

127. Blicher, A., Physics of Semiconductor Power Devices. *Rep Prog Phys* **1982,** *45*, 427-468.

128. A Brief Review of Iii-Nitride Uv Emitter Technologies and Their Applications; In *Iii-Nitride Ultraviolet Emitters: Technology and Applications*; Kneissl, M., Kneissl, M.; Rass, J., Eds. Springer International Publishing: Cham, 2016; pp 1-25.

129. Shabunina, E. I.; Levinshtein, M. E.; Kulagina, M. M.; Kurin, S. Y.; Chernyakov, A. E.; Petrov, V. N.; Ratnikov, V. V.; Smirnova, I. N.; Troshkov, S. I.; Shmidt, N. M.; Usikov, A. S.; Helava, H.; Yu, N. M., Nanomaterial Disordering in Algan/Gan Uv Led Structures. *Journal of Physics: Conference Series* **2015,** *643*, 012128.

130. Zhang, Y.; Krishnamoorthy, S.; Akyol, F.; Allerman, A. A.; Moseley, M. W.; Armstrong, A. M.; Rajan, S., Design and Demonstration of Ultra-Wide Bandgap Algan Tunnel Junctions. *Appl Phys Lett* **2016,** *109*, 121102.

131. Pimputkar, S.; Speck, J. S.; DenBaars, S. P.; Nakamura, S., Prospects for Led Lighting. *Nature Photonics* **2009,** *3*, 180.

132. Sun, W.; Shatalov, M.; Deng, J.; Hu, X.; Yang, J.; Lunev, A.; Bilenko, Y.; Shur, M.; Gaska, R., Efficiency Droop in 245–247 Nm Algan Light-Emitting Diodes with Continuous Wave 2 Mw Output Power. *Appl Phys Lett* **2010,** *96*, 061102.

133. Chih-Chien, P.; Tao, G.; Nathan, P.; Shinichi, T.; Yuji, Z.; Daniel, F.; James, S. S.; Shuji, N.; Steven, P. D., Reduction in Thermal Droop Using Thick Single-Quantum-Well Structure in Semipolar (2021) Blue Light-Emitting Diodes. *Applied Physics Express* **2012,** *5*, 102103.

134. Ni, X.; Fan, Q.; Shimada, R.; Özgür, Ü.; Morkoç, H., Reduction of Efficiency Droop in Ingan Light Emitting Diodes by Coupled Quantum Wells. *Appl Phys Lett* **2008,** *93*, 171113.

135. Lu, T.; Li, S.; Liu, C.; Zhang, K.; Xu, Y.; Tong, J.; Wu, L.; Wang, H.; Yang, X.; Yin, Y.; Xiao, G.; Zhou, Y., Advantages of Gan Based Light-Emitting Diodes with a P-Ingan Hole Reservoir Layer. *Appl Phys Lett* **2012,** *100*, 141106.

136. Vampola, K. J.; Iza, M.; Keller, S.; DenBaars, S. P.; Nakamura, S., Measurement of Electron Overflow in 450 Nm Ingan Light-Emitting Diode Structures. *Appl Phys Lett* **2009,** *94*, 061116.

137. Joachim, P., Efficiency Droop in Nitride‐Based Light‐Emitting Diodes. *physica status solidi (a)* **2010,** *207*, 2217-2225.

138. Bernardini, F.; Fiorentini, V.; Vanderbilt, D., Spontaneous Polarization and Piezoelectric Constants of Iii-V Nitrides. *Physical Review B* **1997,** *56*, R10024-R10027.

139. Morkoç, H.; Cingolani, R.; Gil, B., Polarization Effects in Nitride Semiconductor Device Structures and Performance of Modulation Doped Field Effect Transistors. *Solid-State Electronics* **1999,** *43*, 1909-1927.

140. Wu, Y. F.; Saxler, A.; Moore, M.; Smith, R. P.; Sheppard, S.; Chavarkar, P. M.; Wisleder, T.; Mishra, U. K.; Parikh, P., 30-W/Mm Gan Hemts by Field Plate Optimization. *IEEE Electron Device Letters* **2004,** *25*, 117-119.

141. Son, J. H.; Lee, J.-L., Strain Engineering for the Solution of Efficiency Droop in Ingan/Gan Light-Emitting Diodes. *Opt Express* **2010,** *18*, 5466-5471.

142. Li, Y.-L.; Huang, Y.-R.; Lai, Y.-H., Efficiency Droop Behaviors of Ingan ⁄ Gan Multiple-Quantum-Well Light-Emitting Diodes with Varying Quantum Well Thickness. *Appl Phys Lett* **2007,** *91*, 181113.

143. Yuji, Z.; Shinichi, T.; Chih-Chien, P.; Kenji, F.; Daniel, F.; James, S. S.; Steven, P. D.; Shuji, N., High-Power Blue-Violet Semipolar (2021) Ingan/Gan Light-Emitting Diodes with Low Efficiency Droop at 200 a/Cm 2. *Applied Physics Express* **2011,** *4*, 082104.

144. Feezell, D. F.; Speck, J. S.; DenBaars, S. P.; Nakamura, S., Semipolar (20-2-1) Ingan/Gan Light-Emitting Diodes for High-Efficiency Solid-State Lighting. *Journal of Display Technology* **2013,** *9*, 190-198.

145. Xie, J.; Ni, X.; Fan, Q.; Shimada, R.; Özgür, Ü.; Morkoç, H., On the Efficiency Droop in Ingan Multiple Quantum Well Blue Light Emitting Diodes and Its Reduction with P-Doped Quantum Well Barriers. *Appl Phys Lett* **2008,** *93*, 121107.

146. Wang, X.; Tong, J.; Chen, X.; Zhao, B.; Ren, Z.; Li, D.; Zhuo, X.; Zhang, J.; Yi, H.; Liu, C.; Fang, F.; Li, S., Highly Ordered Gan-Based Nanowire Arrays Grown on Patterned (100) Silicon and Their Optical Properties. *Chemical Communications* **2014,** *50*, 682-684.

147. Yu, R.; Wang, X.; Peng, W.; Wu, W.; Ding, Y.; Li, S.; Wang, Z. L., Piezotronic Effect in Strain-Gated Transistor of a-Axis Gan Nanobelt. *Acs Nano* **2015,** *9*, 9822-9829.

148. Johnson, J. C.; Choi, H.-J.; Knutsen, K. P.; Schaller, R. D.; Yang, P.; Saykally, R. J., Single Gallium Nitride Nanowire Lasers. *Nat Mater* **2002,** *1*, 106.

149. Qian, F.; Li, Y.; Gradečak, S.; Wang, D.; Barrelet, C. J.; Lieber, C. M., Gallium Nitride-Based Nanowire Radial Heterostructures for Nanophotonics. *Nano Lett* **2004,** *4*, 1975-1979.

150. Verzellesi, G.; Saguatti, D.; Meneghini, M.; Bertazzi, F.; Goano, M.; Meneghesso, G.; Zanoni, E., Efficiency Droop in Ingan/Gan Blue Light-Emitting Diodes: Physical Mechanisms and Remedies. *J Appl Phys* **2013,** *114*, 071101.

151. Eliseev, P. G.; Perlin, P.; Lee, J.; Osiński, M., "Blue" Temperature-Induced Shift and Band-Tail Emission in Ingan-Based Light Sources. *Appl Phys Lett* **1997,** *71*, 569-571.

152. Cabrera, B.; Clarke, R. M.; Colling, P.; Miller, A. J.; Nam, S.; Romani, R. W., Detection of Single Infrared, Optical, and Ultraviolet Photons Using Superconducting Transition Edge Sensors. *Appl Phys Lett* **1998,** *73*, 735-737.

153. Park, T.-Y.; Choi, Y.-S.; Kim, S.-M.; Jung, G.-Y.; Park, S.-J.; Kwon, B.-J.; Cho, Y.-H., Electroluminescence Emission from Light-Emitting Diode of P-Zno/(Ingan/Gan) Multiquantum Well/N-Gan. *Appl Phys Lett* **2011,** *98*, 251111.

154. Schubert, M. F.; Xu, J.; Kim, J. K.; Schubert, E. F.; Kim, M. H.; Yoon, S.; Lee, S. M.; Sone, C.; Sakong, T.; Park, Y., Polarization-Matched Gainn / Algainn Multi-Quantum-Well Light-Emitting Diodes with Reduced Efficiency Droop. *Appl Phys Lett* **2008,** *93*, 041102.

155. Singh, S.; Robidas, D.; Rohila, N.; Pal, S.; Dhanavantri, C., Effect of Electron Blocking Layer on Efficiency Droop in Blue Ingan/Gan Based Light-Emitting Diodes. *Optoelectron Adv Mat* **2010,** *4*, 1106-1110.

156. Kim, M.-H.; Schubert, M. F.; Dai, Q.; Kim, J. K.; Schubert, E. F.; Piprek, J.; Park, Y., Origin of Efficiency Droop in Gan-Based Light-Emitting Diodes. *Appl Phys Lett* **2007,** *91*, 183507.

157. Ling, S.-C.; Lu, T.-C.; Chang, S.-P.; Chen, J.-R.; Kuo, H.-C.; Wang, S.-C., Low Efficiency Droop in Blue-Green M-Plane Ingan/Gan Light Emitting Diodes. *Appl Phys Lett* **2010,** *96*, 231101.

158. Zhang, Z.-H.; Tan, S. T.; Kyaw, Z.; Ji, Y.; Liu, W.; Ju, Z.; Hasanov, N.; Sun, X. W.; Demir, H. V., Ingan/Gan Light-Emitting Diode with a Polarization Tunnel Junction. *Appl Phys Lett* **2013,** *102*, 193508.

159. Kaufmann, U.; Schlotter, P.; Obloh, H.; Köhler, K.; Maier, M., Hole Conductivity and Compensation in Epitaxial Gan:Mg Layers. *Physical Review B* **2000,** *62*, 10867-10872.

160. Wei, B.; Zheng, K.; Ji, Y.; Zhang, Y.; Zhang, Z.; Han, X., Size-Dependent Bandgap Modulation of Zno Nanowires by Tensile Strain. *Nano Lett* **2012,** *12*, 4595-4599.